UNIVERSITY OF CALIFORNIA
RIVERSIDE

Electrical Transport Properties of Topological Insulators and Graphene

A Dissertation submitted in partial satisfaction
of the requirements for the degree of

Doctor of Philosophy

in

Physics

by

Zhiyong Wang

June 2014

Dissertation Committee:
Dr. Jing Shi, Chairperson
Dr. Ward Beyermann
Dr. Vivek Aji

The Dissertation of Zhiyong Wang is approved:

_____

_____

_____

Committee Chairperson

University of California, Riverside

Acknowledgement

This is one of the most meaningful periods in my life. It is not only an opportunity to pursue higher education but also a completely new style of life. Different from the studies in primarily school, middle school, high school and even undergraduate university, it provides me an entirely new angle to see, to think, and to do.

First and foremost, I want to express my gratitude to Professor Jing Shi for his guide on my scientific research. Without his encouragement, advice, guidance and support, I could not achieve what I have today. He always shows enthusiasm on research works and aggressive attitude towards the approach to goals. I can feel his love for physics. And I am so inspired and stimulated by his passion on physics research. He teaches me to think more fundamentally and coherently to see the nature of problems and find out the optimal solutions. He also asks me to think independently and to insist on and fight for my own opinion. I've benefited a lot from what he says and does.

I would like to express my appreciation to Professor Ward Beyermann for the useful discussions on my topological insulators and transition metal dichalcogenides projects. And I want to thank him for letting me use the Quantum Design's physical property measurement system for my low temperature measurements and providing useful tips for using the system. And I would like to express my appreciation to Professor Vivek Aji for the useful discussions on topological insulators. I would also like to thank Professor Roland Kawakami and Professor Jianlin Liu for being on my oral exam committees.

I would like to thank Professor Yadong Yin and his students for helping me using their glovebox on my topological insulators project; Dong Yan and Dexter Humphrey for the help in cleanroom; Stan Sheldon for the help on the quartz tube work of my topological insulators project, and Ross McDonald for the help in my pulsed field experiments.

I would like to acknowledge all my labmates and friends. I would like to thank Peng Wei for teaching and showing me his experiment skills and technique, his careful and serious attitude towards the research work, and his rich knowledge in Physics. I would like to thank Deqi Wang, Xinfei Liu, Tao Lin, and Raymond Sachs for teaching me a lot of useful lab skills and discussing problems that I met in my projects. I would like to thank Raymond Sachs for teaching me the transfer technique in my transition metal dichalcogenides and graphene projects. I would like to thank Wei Han for his useful suggestions and discussions. I would like to thank Yan Li for her help when I was in Los Alamos National Lab. I would like to thank Yafis Barlas for the discussions on my graphene project. I would like to thank Tengfei Miao, Peng Wang, Bin Cheng, Fenglin Wang, Hua Wen for their discussions. I would like to thank Zhisheng Lin, Chi Tang, Zilong Jiang, Yadong Xu, Hamad Alyahyaei, Bowen Yang for their help. And I would like to thank all my friends supporting me all the time.

Last but not least, I want to express my deepest love to my parents. They always give me whatever they have without asking for anything. They give me strength whenever I feel weak. They give me support whenever I feel depressed or frustrated. I love them!

ABSTRACT OF THE DISSERTATION

Electrical Transport Properties of Topological Insulators and Graphene

by

Zhiyong Wang

Doctor of Philosophy, Graduate Program in Physics
University of California, Riverside, June 2014
Dr. Jing Shi, Chairperson

This dissertation summarizes my work on the study of topological insulators, graphene, and transition metal dichalcogenides, especially on the electrical transport studies. There are mainly two parts in this dissertation. The first part is the study on topological insulators. Bi_2Se_3 and Bi_2Te_2Se single crystals are synthesized and characterized. Calcium dopants are introduced to Bi_2Se_3 to compensate for the excess electrons generated by selenium vacancies in the as-grown single crystals. An n- to p-type transition is then realized. The bulk insulating state is achieved. In Bi_2Te_2Se bulk samples, extremely high low-temperature resistivity (>2 Ω·cm) is achieved. Nanodevices of Bi_2Se_3 and Bi_2Te_2Se are then fabricated. A lithography-free technique is developed for device fabrication in order to well maintain the pristine state of bulk samples. Electron beam irradiation is performed to manually adjust the Fermi levels in the devices. Further control of the Fermi level is realized with the application of gate voltages. The insulating temperature behavior is

achieved in devices upon electron beam irradiation. And the gate modulation grows as the electron beam irradiation dosage increases. The field-effect mobility is greatly enhanced and a ten-fold increase is obtained.

The second part is focused on graphene and transition metal dichalcogenides. Graphene is expected to exhibit ferromagnetism induced by the magnetic proximity effect when it is placed on a magnetic material. With enhanced spin-orbit coupling, the anomalous Hall effect can be realized in graphene. Meanwhile, a topological gap is opened at the Dirac point, making it possible to realize the quantized anomalous Hall effect when the Fermi level is in the gap. In this dissertation, graphene devices are transferred to yttrium iron garnet thin films, a ferrimagnetic material. At low temperatures, anomalous Hall effect is observed. Further studies on the temperature dependence and gate dependence of the anomalous Hall effect is performed.

For single-layer MoS_2, at the valence band maxima, the band is split by 160 meV due to strong spin-orbit coupling. Spin-up and spin-down electrons reside in different bands due to the broken inversion symmetry. Valley and spin degrees of freedom of the valence bands are inherently coupled in single-layer MoS_2. It is an ideal material to study the valley Hall effect.

Contents

List of Figures

List of Tables

Chapter 1 Introduction

In recent years, the 2-dimensional layered structure materials have been attracting people's attention and research interest due to their unique properties and practical applications, such as graphene, topological insulators, transition metal dichalcogenides, etc.

The single layer graphite which is called graphene has been studied tremendously over the past 10 years since the first discovery in lab[1] due to its unique band structure and extremely high mobility. Topological insulators, predicted[2] in 2006, are being more and more explored recently due to its exceptional property of the non-backscattering carriers and low energy dissipation. And for transition metal dichalcogenides, they have been used as traditional lubricants for years due to the layered structure. However, as the thickness of transition metal dichalcogenides approaches single layer, the band structure changes accordingly[3]. And interesting behaviors emerge, some of which are even, to some extent, superior to graphene, for example, the valley Hall effect[4].

This dissertation contains two major parts: the study of topological insulators (both bulk materials and nanodevices), and graphene devices on magnetic insulator thin films, the study on transition metal dichalcogenides nanodevices is included as a section in the graphene chapter.

1.1 Topological Insulators

Generally, a topological insulator is an insulator which is insulating in its bulk but allows the movement of carriers on its boundary (edges for 2-dimensional materials and surfaces for 3-dimensional materials).

According to the dimensions, topological insulators can be categorized as 2-dimensional (2D) topological insulators (2D TIs) and 3-dimensional (3D) topological insulators (3D TIs). For 2D TIs,

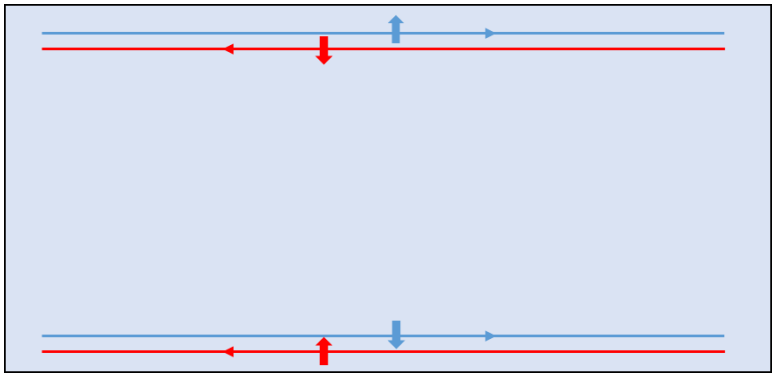

Figure 1-1 Edge states in a 2D TI
Blue and red lines represent two channels on each edge. The opposite blue and red arrows indicate different spin orientations in the two channels.

there are gapless edge states existing in the gapped bulk bands due to the band inversion. The edges are conducting without energy dissipation while the bulk is still an insulator. For 3D TIs, there are two types: weak and strong topological insulators[5-8]. The 3D weak TI can be simply treated as a stack of 2D TIs. It is conducting on some surfaces while the bulk is insulating. But its Berry curvature is zero, which means it is not robust to disorder or weak interactions. However, for 3D strong TIs, all of its surfaces are conducting and immune to non-magnetic disorder and weak interactions with a Berry curvature of π while the bulk is insulating with zero Berry curvature.

In a 2D TI, only edge states are allowed. And there are only two channels existing on each edge, as is illustrated in Figure 1-1. The two channels have different carrier propagation direction and spin direction. The spin and momentum are locked due to the strong spin-orbit coupling. When subjected to a non-magnetic impurity, the electron has two different ways to be scattered backward, as is demonstrated in Figure 1-2. And the chances of both ways are equal since the impurity is non-magnetic. Backscattered electrons in Figure 1-2**a** and **b** have a phase difference of 2π. Since the spin of an electron is ½, the possibility of the backscattered electrons is the superposition of the possibilities of the two types of electrons with a phase difference of 2π, which is zero. In other words, there are no backscattered electrons. However, the situation will be different if the impurity

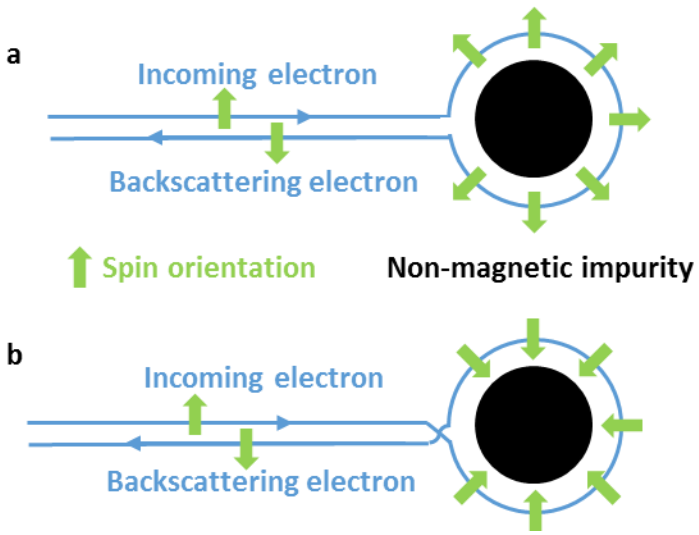

Figure 1-2 Electron scattering mechanism in a 2D TI
The black solid circle is a non-magnetic impurity. Green arrows stand for the spin orientations. Blue curves are trajectories of the electrons being scattered.

is magnetic. The chances of the two types of the backscattered electrons are not equal anymore. The possibility of the backscattered electrons is not zero and there will be backscattered electrons with the presence of magnetic impurities. Without magnetic impurity, carriers in these two edge channels propagate without dissipation and give rise to the quantum conductance $2e^2/h$.

The situation is more complex for a 3D TI. The backscattered electrons are still prohibited. Moreover, the electrons scattered to other directions are suppressed to some extent which depends on the direction of the scattered electrons, as is demonstrated in Figure 1-3, the length of the arrow lines stands for the possibility of scattering electrons in that direction. Since there are still electrons being scattered to other directions, the lowest conductance in a 3D TI could be lower than $2\ e^2/h$.

In 2005, the quantum spin Hall effect was predicted to exist in graphene with edge states in the tiny gap opened near the Dirac point[9,10]. Due to the extremely weak spin-orbit coupling, this gap is so small that the effect was not experimentally observed. In 2006, a quantum spin Hall insulator, which is the 2D topological insulator, CdTe/HgTe/CdTe quantum well was predicted to have band

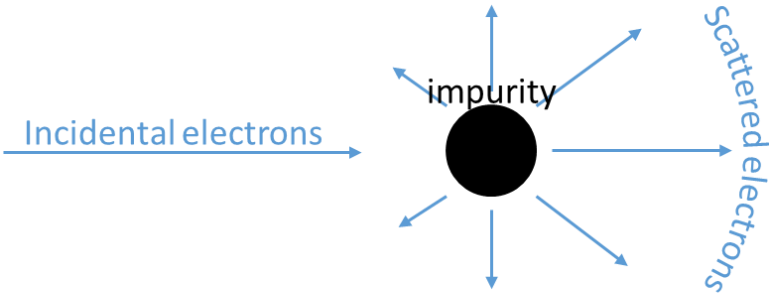

Figure 1-3 Scattered electrons in a 3D TI
The black solid circle represents a nonmagnetic impurity. Blue lines with arrows are the directions of the scattered electrons

inversion in HgTe at some critical thickness, leading to nontrivial gapless edge states[2]. Unlike the quantum Hall effect, in quantum spin Hall effect, there are two channels existing on each edge even without the external magnetic field, Figure 1-2. Electrons with opposite spins travel to different directions in these two channels without backscattering due to strong spin-orbit coupling. Soon after the prediction, in 2007, this topological CdTe/HgTe/CdTe quantum well was experimentally realized with the achievement of the quantum conductance[11] 2 e^2/h.

After the discovery of the 2D topological insulator, Bi_xSb_{1-x} was found out to be a 3D topological insulator and 5 surface bands was detected by angle-resolved photoemission spectroscopy (ARPES)[6,12-14]. However, as an alloy, there are many uncontrollable defects in the material. The bulk bandgap is small and the surface band structure is complicated due to the existence of 5 surface bands, making the characteristic properties of this material difficult to be observed in transport experiments. Then in 2009, compound materials such as Bi_2Se_3, Bi_2Te_3 and Sb_2Te_3, were predicted and experimentally verified to be a new generation of the 3D topological insulators with only one single Dirac cone[15-20]. The band structures of Bi_2Se_3, Bi_2Te_3, Sb_2Te_3, and

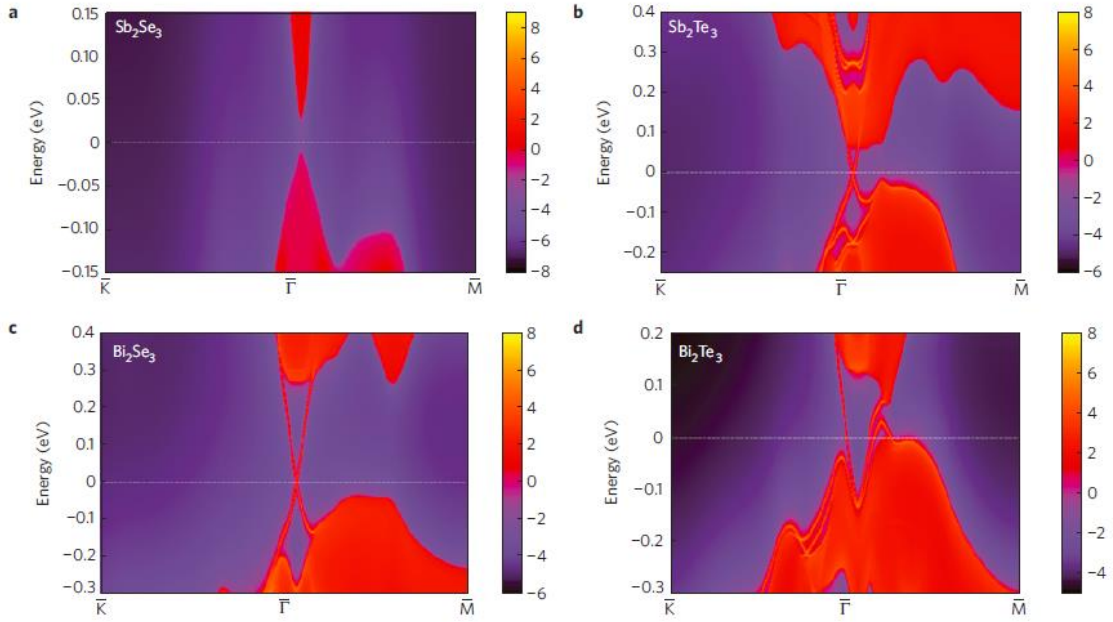

Figure 1-4 Band Structures of Sb_2Se_3, Bi_2Se_3, Sb_2Te_3, and Bi_2Te_3
Red regions are bulk bands. Blue regions are bulk bandgaps. Red lines are the surface states. There is no surface states in Sb_2Se_3. [Zhang, *et al. Nature Physics* **5**, 438-442]

Sb_2Se_3 are shown in Figure 1-5. Among these 3 candidates, Bi_2Se_3 has superior properties to the other two for its large bulk band gap and simple band structure near the Dirac point.

Although Bi_2Se_3 is theoretically an ideal candidate for 3D TIs, the as-grown Bi_2Se_3 single crystals have lots of defects, among which the Se vacancy is the majority type. Se vacancies lead to heavily n-type doping in Bi_2Se_3. As for Bi_2Te_3, the impurities are mainly from the Bi-Te antisite defects leading to heavily p-type doping in Bi_2Te_3. Then ternary compound, and even quaternary compound were introduced, such as Bi_2Te_2Se[21,22], Bi_2Te_2S, $(Bi_xSb_{1-x})_2Te_3$[23-26], $(Bi_xSb_{1x})_2(Te_ySe_{1-y})_3$[27,28], etc. In 2013, the quantum anomalous Hall effect (QAHE) was achieved in Cr-doped $(Bi_xSb_{1-x})_2Te_3$[26]. Moreover, the magnetism induced in topological insulators has also been studied extensively[23,26,29-31].

In addition to the traditional TIs, other topological insulators are being proposed and studied, such as the topological Anderson insulators[32-34], topological crystalline insulators[35], topological Kondo insulators[36], organic topological insulators[37], etc.

1.2 Graphene

Carbon atom is the fundamental element in organic compounds which form all kinds of lives. Among carbon's allotropes, graphene is a very special one since it can form carbon's other allotropes, ranging from the zero-dimensional (0D) fullerenes, one-dimensional (1D) carbon nanotubes[38], three-dimensional (3D) graphite, etc. The 0D fullerene can be considered as a special wrap of a certain area of graphene by introducing pentagons into the structure. 1D carbon nanotubes can be fabricated by rolling up a sheet of graphene along a certain edge. And 3D graphite is actually a stack of multiple graphene layers.

In graphene, carbon atoms are bonded together with the σ band, which is formed by the sp^2 hybridization in two adjacent carbon atoms. The sp^2 hybridization is formed from one *s* orbital and two *p* orbitals. The three hybridized sp^2 orbitals have an angle of 120 °between each other and lie in the same plane. The unhybridized *p* orbital is perpendicular to that plane and forms a π band throughout the entire graphene sheet. It is only half-filled due to the half-filled unhybridized *p* orbitals.

Figure 1-5 is the band structure of graphene. The valence band and conduction band meet at the **K** and **K'** points. Without impurities and disorder, the valence band is fully-filled and the conduction band is empty, which is called the charge neutral state. The Fermi level exactly crosses at the point where the valence band and conduction band meet, which is the charge neutral point, also known as the Dirac point. The electron's energy has a linear dispersion relationship with

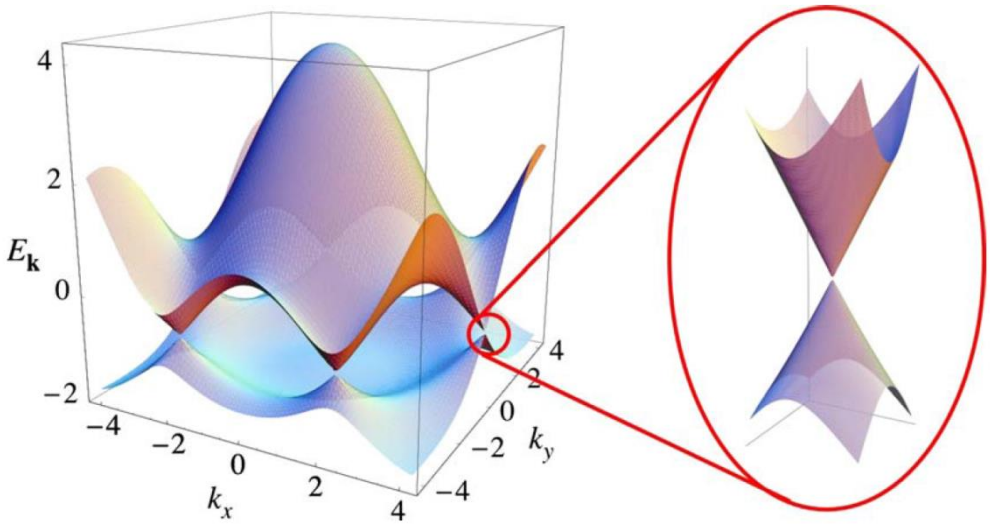

Figure 1-5 Band structure of graphene
Left figure is the band structure of graphene. Right figure is a zoom in plot near the Dirac point. [Castro Neto, *et al. Review of Modern Physics* **81**, 109]

respect to the wavevector ***k*** in the reciprocal space. With this linear dispersion, carriers in graphene are massless Dirac Fermions with extremely high mobility. When subjected to a magnetic field, the Dirac Fermions will exhibit new phenomena, for example, the quantum Hall effect (QHE)[39,40]. And they are not sensitive to external disorder and immune to some localization effects.

Since the first lab exfoliation and fabrication of graphene[1], this material has been studied for 10 years on different properties, including the magnetic properties, such as the introduced local magnetic moments along the edges of graphene nanoribbons[41], around vacancies in graphene[42], or adatoms[43]. But additional exchange coupling between local moments and graphene is required for the long-range ferromagnetic order. This can be approached either by doping graphene with transition metal atoms[44] or by coupling graphene with a magnetic insulator via the proximity effect. Random doping of impurities always lowers graphene's carrier mobility. With the proximity

coupling, one can expect the hybridization between graphene's π band and the spin-polarized *d*-orbitals in the magnetic insulator.

Carriers in graphene in the absence of exchange interaction or external magnetic field are spin-degenerate. For each state, there are spin-up and spin-down carriers with the same ground state energy. However, the spins will be split when the exchange coupling between graphene and the magnetic insulator exists. The populations of spin-up and spin-down carriers will be different. If graphene is provided with strong spin-orbit coupling, the anomalous Hall effect (AHE) and even the quantized anomalous Hall effect (QAHE) can be realized in graphene.

Recently, a theoretical paper[45] has proposed a mechanism for graphene with a magnetic exchange field and Rashba spin-orbit coupling (SOC). With the presence of both effects, graphene will open a gap at the Dirac point of the 2D spectrum and forms a gapless topological edge states. And the QAHE can be expected, which will be discussed specifically in Chapter 2.

1.3 Transition Metal Dichalcogenides

In this dissertation, transition metal dichalcogenides (TMDs) are referred to the group VI transition metal sulfides and selenides, which are MoS_2, $MoSe_2$, WS_2, and WSe_2.

These compounds have the same layered structure which is two layers of chalcogen atoms (S or Se) sandwiching one layer of the transition metal atoms (Mo or W). Layers are bonded together via the Van der Waals force. These materials in this group all have an indirect band gap between 1 to 2 *eV*. Similar to the graphene structure, the Van der Waals force between the layers is weak and easy to break. Together with the immunity to dilute acid and oxygen, they are excellent solid lubricant materials.

However, when the material is thinned down to only one layer, the band structure becomes different, and its electrical and optical properties will change dramatically. I will only discuss MoS_2 in this chapter and the rest of this group is similar to MoS_2. MoS_2 has an indirect bandgap of 1.2 *eV* in its bulk form. This indirect bandgap will change to a direct gap from 1.2 eV to 1.8 eV when MoS_2 is thinned down to single layer[3].

For bulk and bilayer MoS_2, the inversion symmetry preserves, which is $E(\boldsymbol{k}, \uparrow) = E(-\boldsymbol{k}, \uparrow)$, where E is electron energy, $\boldsymbol{k}$ is the wavevector of the electron, and $\uparrow\downarrow$ are the electron spin orientations. With the time-reversal symmetry protected by the strong spin-orbit coupling in MoS_2, $E(\boldsymbol{k}, \uparrow) = E(-\boldsymbol{k}, \downarrow)$, one can have $E(\boldsymbol{k}, \uparrow) = E(\boldsymbol{k}, \downarrow)$, which means the spin is degenerate in bulk and bilayer MoS_2, Figure 1-5**d**. But the situation is quite different for single-layer MoS_2, where the inversion symmetry is broken. The lack of inversion symmetry means electrons moving in opposite directions experience different potentials. With only time-reversal symmetry, $E(\boldsymbol{k}, \uparrow) = E(-\boldsymbol{k}, \downarrow)$, the spins are split in single-layer MoS_2, Figure 1-5**c**.

In the top view of the single-layer MoS_2 along z-direction, Figure 1-5**b**, MoS_2 atoms are assembled to a hexagonal structure, which is similar to graphene. And it also has two valleys, K and K', the same as graphene. The Berry curvatures for these two valleys are finite but opposite due to the broken inversion symmetry, which means that electrons in different valleys experience opposite effective magnetic fields and thus opposite forces. The opposite forces deflect the electrons in different valleys to different transverse directions in MoS_2 when a longitudinal electric field is applied. This is called the valley Hall effect (VHE), analogous to the spin Hall effect (SHE) in which electrons with different spins are deflected to different transverse edges when a longitudinal electric field is applied. Valley, similar to spin, is also a degree of freedom in MoS_2.

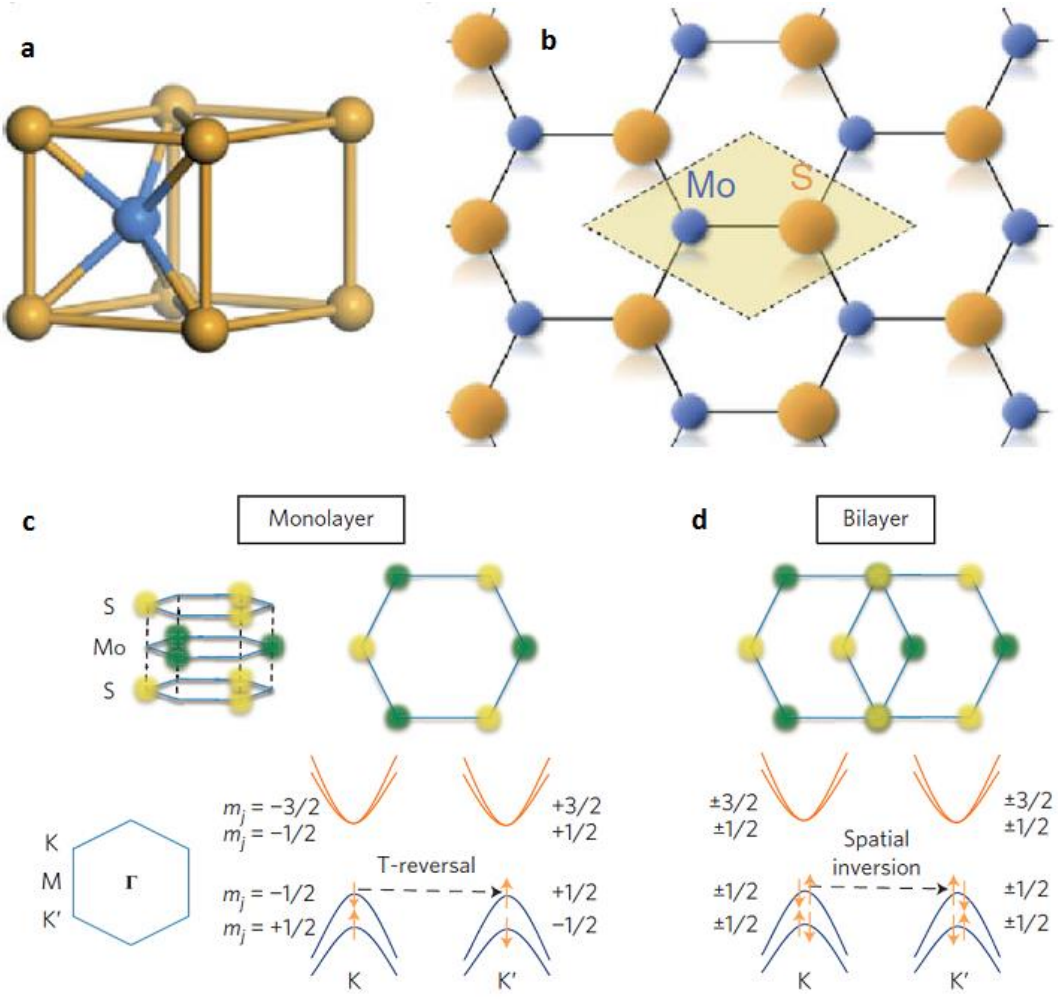

Figure 1-6 MoS_2 structures

a, a unit cell of MoS_2. **b**, top view of a single-layer MoS_2. Blue spheres are molybdenum atoms and yellow spheres are sulfur atoms. [Cao, *et al*. *Nature Communications* **3**, 887] **c**, Single-layer MoS_2 band structure. **d**, Bilayer MoS_2 band structure. Orange lines are conduction bands and blue lines are valence bands. [Mak, *et al. Nature Nanotechnology* **7**, 494]

The VHE is a consequence of the coupling of the valley degree of freedom to the electron's orbital degree of freedom while the SHE results from the spin-orbit coupling.

At the valence band maxima, the band is split by 160 meV due to strong spin-orbit coupling[46]. Spin-up and spin-down electrons reside in different bands because of the broken inversion symmetry, as is shown in Figure 1-5**c**. The valley and spin in the valence bands are inherently

coupled. However, the situation is quite different for bilayer MoS_2. Although there is a band splitting at the bulk band maxima, the spins are degenerate. The valley and spin are not coupled any more.

Particularly, when the Fermi level is adjusted in the valence band where it only crosses the higher split band but not the lower one, there will be only spin-up electrons in one valley and spin-down electrons in the other valley. When an electric field is applied, in addition to the VHE, the spins are polarized, too. Even more specifically, when the single-layer MoS_2 gets close to a magnetic material, the spins will be polarized. Then the valence bands at two valleys will have different height (chemical potential). Assuming valence bands at K is higher than those at K', when the Fermi level is tuned to the position where it only crosses the higher split band of the valence bands at K but not at K', then only carriers at K valley are populated with the same spin orientation. When subjecting a longitudinal electric field, there will be not only a spin current but also a charge current in this case.

Chapter 2 Topological Insulators

2.1 Bi_2Se_3 and Bi_2Te_2Se

2.1.1 Introduction to Bi_2Se_3

Bi_2Se_3 single crystal is a rhombohedral lattice system with the space group D_{3d}^5 ($R\bar{3}m$). It has a layer-stacked structure. As is shown in Figure 2-1, red square, for each layer of Bi_2Se_3, it consists 5 layers of atoms in the order of Se1-Bi1-Se2-Bi1'-Se1' (Figure 2-1**a** and **c,** red square region)[15], which is called a quintuple layer. These quintuple layers are bonded together with the Van der Waals force, which form the Bi_2Se_3 single crystal. Each quintuple layer of Bi_2Se_3 has a thickness of ~ 1 nm.

Compared to other 3D topological insulators, Bi_2Se_3 is an ideal material to study the properties of topological insulators because it has only one single Dirac cone in the bulk bandgap, simple band structures near the Dirac point, and a relatively large bulk bandgap[17] E_g ~ 300 meV. Figure 1-4**c** is the band structure of Bi_2Se_3. Moreover, Bi_2Se_3 is a stoichiometric compound, which means there are fewer defects in the single crystal (compared to Bi_xSb_{1-x} alloys). Due to the big bandgap in Bi_2Se_3, the thermal excitations, even at room temperature, are suppressed, indicating the possible application of topological surface states at room temperature.

Although Bi_2Se_3 has many superior properties among other binary compounds in this group (Bi_2Te_3, Sb_2Te_3), as-grown Bi_2Se_3 single crystals always have defects. A major source of the defects comes from the selenium (Se) vacancies[47,48]. Se atoms, leaving the materials, create Se vacancies and introduce excess electrons. Thus Bi_2Se_3 single crystals are turned to heavily n-doped materials,

$$Se_{Se} \rightarrow V_{Se}^{\bullet\bullet} + Se(g) + 2e' .$$

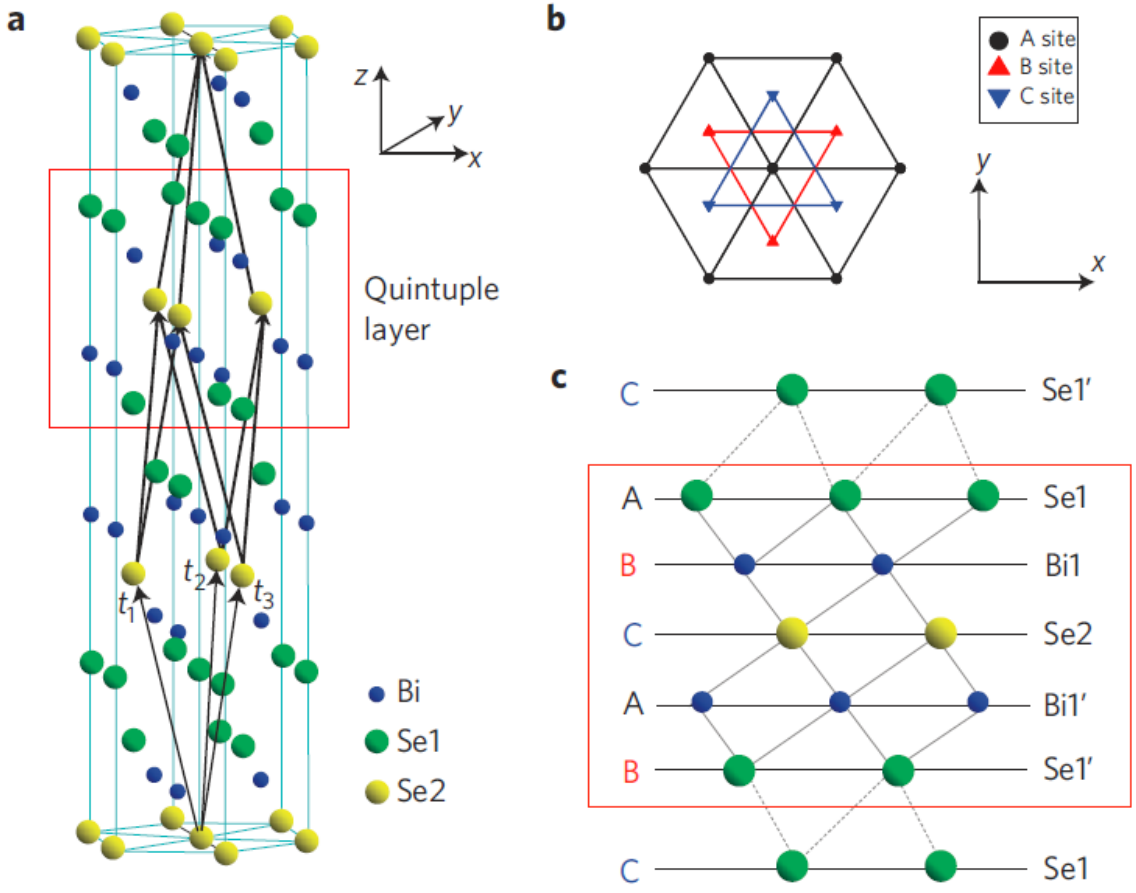

Figure 2-1 Lattice structure of Bi_2Se_3

a. Crystal structure of Bi_2Se_3. In the red square, it is one quintuple layer of Bi_2Se_3 in the order of Se^1-Bi^1-Se^2-$Bi^{1'}$-$Se^{1'}$ (As indicated in the red square in **c**). $\boldsymbol{t_1}$, $\boldsymbol{t_2}$, and $\boldsymbol{t_3}$ are the primitive lattice vectors. **b**. Top view of Bi_2Se_3 crystal lattice along the z-direction. The layers of Bi and Se atoms are in the ABC stacking way. **c**. Side view of Bi_2Se_3 crystal lattice. One quintuple layer of Bi_2Se_3 and the ABC stacking of Bi and Se layers can be clearly seen. [Zhang, H. *et al*, *Nat. Phys.* **5**, 438-442]

To reduce this type of defects, either high Se vapor pressure needs to be precisely controlled during the growth of single crystals or p-type dopants need to be incorporated. Hor, *et al*, proposed a method to introduce a p-type dopant, calcium (Ca), in Bi_2Se_3 to substitute bismuth (Bi) so as to introduce holes to compensate for the excess electrons[48],

$$2Ca \xrightarrow[Bi_2Se_3]{} 2Ca'_{Bi} + 2h^{\bullet}$$

.

After the introduction of Ca dopants, Bi atoms are replaced by Ca atoms. Ca atom has only two electrons in the outermost shell while bismuth atom has three. The Ca_{Bi} site will have a negative charge and then create one hole. The holes created by Ca dopants can compensate for the excess electrons generated by Se vacancies. As Ca doping level increases, the majority carriers will change from electrons to holes, realizing an n- to p-type transition in the materials. At a certain intermediate point, the holes created by Ca dopants could exactly compensate for the electrons generated by Se vacancies so that no free carriers exist in the bulk channels of Bi_2Se_3 crystals and bulk insulating state can be achieved[47,49,50].

However, there is another mechanism for Ca doping: the Ca atoms enter the interstitial position:

$$Ca \rightarrow Ca^{\bullet\bullet} + 2e' .$$

Each Ca atom will introduce two more electrons in the materials and thus increase the electron density. To avoid this mechanism, the exact stoichiometric elements should be precisely controlled in the growth process. Either less Bi or more Se needs to be added together with Ca dopants.

2.1.2 Introduction to Bi_2Te_2Se

Although binary 3D topological insulator Bi_2Se_3 and Bi_2Te_3 have ideal single Dirac cone and relatively large bulk band gap, the as-grown single crystals tend to have high bulk carrier density due to defects and impurities in both as-grown Bi_2Se_3 and Bi_2Te_3 single crystals. For Bi_2Se_3, the large density of Se vacancies leads to excess electrons and change Bi_2Se_3 to a heavily n-type doped degenerate semiconductor. And for Bi_2Te_3, the impurities come mainly from Bi-Te antisite defects and hence introduce excess holes, making Bi_2Te_3 a heavily p-type doped material. The high bulk carrier density due to defects and impurities dominates the overall conductance, making the topological surface states extremely difficult to be detected by transport.

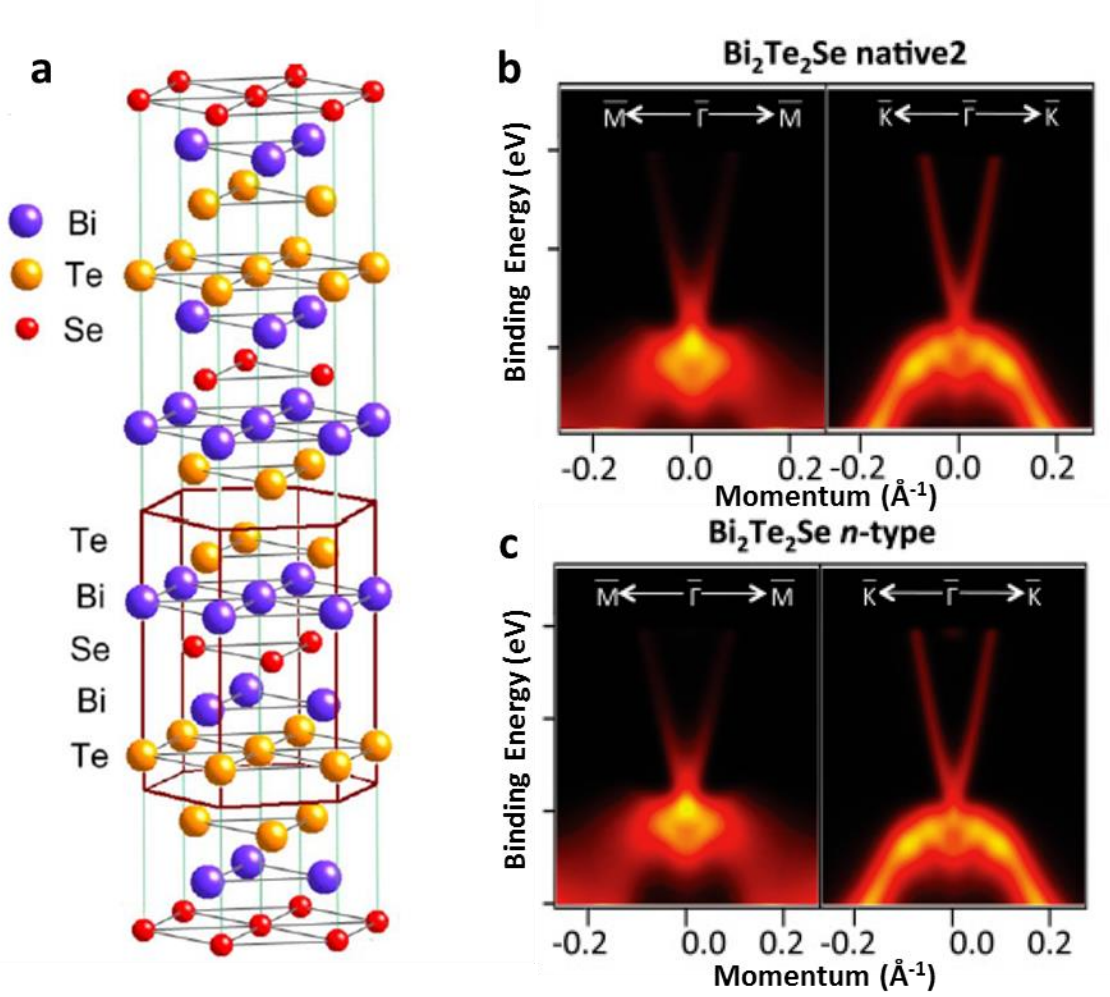

Figure 2-2 Lattice and band structure of Bi_2Te_2Se

a, Bi_2Te_2Se has the same tetradymite structure as Bi_2Se_3 and Bi_2Te_3. And it is also a layered structure with a basic quintuple layer in the order of Te-Bi-Se-Bi-Te. [Ren, *et al. Phys. Rev. B* **82**, 241306 (R)] **b, c**, ARPES of Bi_2Te_2Se in two different samples. Dirac point is buried in the valence band. [Neupane, *et al. Phys. Rev. B* **85**, 235406]

Neupane, *et al.* proposed a new ternary compound as a new candidate of 3D topological insulators, Bi_2Te_2Se, and was confirmed to have topological surface states by angle-resolved photoemission spectroscopy (ARPES) measurement[51], as is shown in Figure 2-2**b**, **c**. And later, this new candidate was proven to achieve insulating states with high resistivity at lowest temperature[21].

Bi_2Te_2Se has the same tetradymite crystal structure as Bi_2Se_3 and Bi_2Te_3. It is also a layered structure with a basic quintuple layer in the order of Te-Bi-Se-Bi-Te, Figure 2-2**a**. In this material, the Se layer is sandwiched in the middle and protected by the outer layers. So Se vacancy formation is expected to be greatly suppressed. Moreover, Se is more electronegative than tellurium (Te) and thus can bind Bi atoms more tightly. Then the Bi-Te antisite defect formation is also expected to be greatly suppressed. With the presence of Se and Te in the same material, not only Se vacancies but Bi-Te antisite defects is, theoretically, reduced tremendously. The total defect density in Bi_2Te_2Se is expected to be greatly reduced. And high resistivity bulk insulating states can be more easily realized in Bi_2Te_2Se than in binary compounds. Hence, it is possible to probe topological surface states in this new topological insulator candidate material.

2.1.3 Single Crystals and Bulk Samples Preparation

Single crystals of pure Bi_2Se_3, Ca-doped Bi_2Se_3 and Bi_2Te_2Se are grown by a multistep heating procedure in a programmable furnace. For pure Bi_2Se_3, high purity Bi_2Se_3 (99.999%, Alfa Aesar) is used for the single crystal growth. For Ca-doped Bi_2Se_3, high purity Bi_2Se_3 (99.999%, Alfa Aesar), Ca (99.98%, Alfa Aesar), and Se (99.999+%, Alfa Aesar) are used. And for Bi_2Te_2Se, high purity Bi_2Se_3 and Bi_2Te_3 (99.999%, Alfa Aesar) are used.

Stoichiometric compounds are put into and sealed in an evacuated quartz tube. After put into a programmable furnace, the tube is then slowly heated up to and kept at 800 ℃ for 24 hours. After that, it is subsequently cooled to and kept at 500 ℃ for another 72 hours before it is finally cooled down to room temperature slowly[48,49,52,53].

Single crystals up to ½ inch in length and ¼ inch in width are obtained after the growth, Figure 2-3. X-ray diffraction (XRD) spectroscopy is performed on the as-grown single crystals, which is

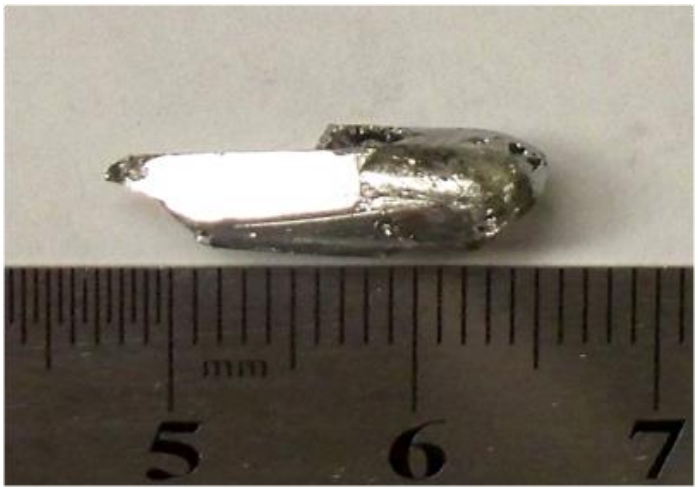

Figure 2-3 Bi_2Se_3 single crystal

Bi_2Se_3 single crystal after the multistep heating growth. A shiny plane was found after a few times of cleavage. And thin flakes could be peeled off from the shiny plane.

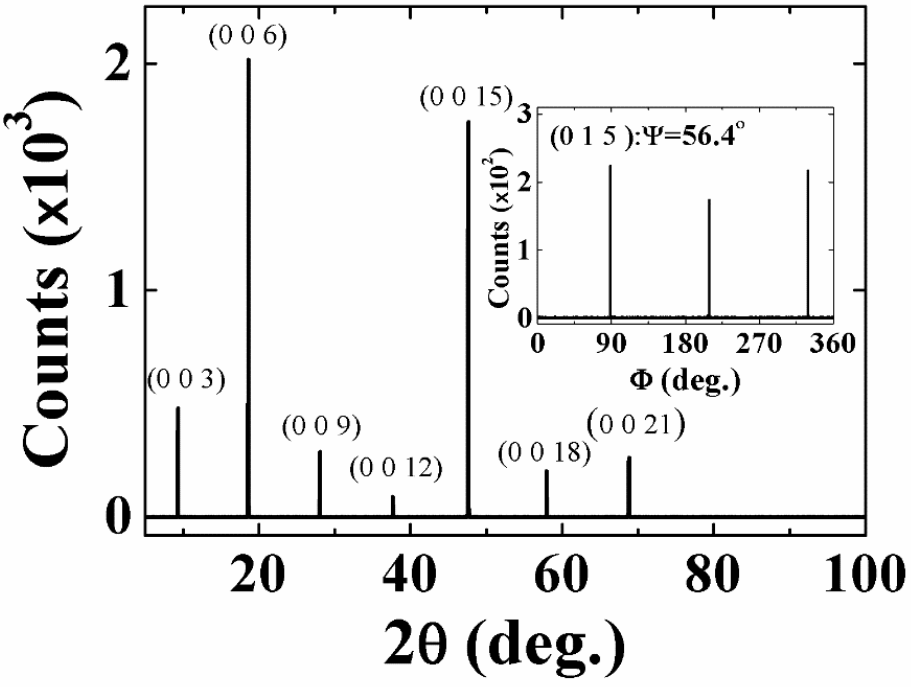

Figure 2-4 XRD pattern of Bi_2Se_3 single crystals

Only (0 0 3) family of diffraction planes are identified in the diffraction pattern. The full width at half maximum of the peaks is very small, indicating high crystal quality and large grain size. The inset is an azimuthal scan measured at a tilt angle of 56.4 º. It shows a threefold symmetry of the (0 1 5) plane which is consistent with expectation.

displayed in Figure 2-4. Only the (0 0 3) family of diffraction planes are observed in the diffraction pattern. The full width at half maximum of the peaks is very small (< 40 mdeg). And the peaks are very sharp, indicating high crystal quality and large grain size. The inset is an azimuthal scan measured at a tilt angle of 56.4 º. It shows a threefold symmetry of the (0 1 5) plane which is consistent with expectation. The x-ray diffraction pattern confirms that the as-grown single crystals are of high quality.

Shiny planes can be easily found after a few cleavages of the as-grown materials. Then thin flakes with a typical thickness of 20 μm are cleaved from the single crystals. The cleaved thin flakes are then performed with Fourier Transform Infrared Spectroscopy (FTIR) to characterize thickness and the relative Fermi level position. After characterization, the flakes are then connected with indium dots and gold wires for electrical transport property measurements. For small flakes, the Van der Pauw geometry connection is employed. And five-terminal geometry connection is employed for big flakes. Figure 2-5 is the pictures of samples with Van der Pauw geometry (left) and five-terminal geometry connections (right).

To use the Van der Pauw geometry, the sample should be homogeneous, isotropic, uniform in thickness, and has no isolated holes. Indium contacts should be at the edge of the sample and as small as possible. To measure the sheet resistance, R_S, two different measurements are needed. First, apply a current along one edge of the sample (for example from contact 1 through 2, left figure in Figure 2-5). Then measure the voltage across the opposite edge (contact 3 and 4). One can define $R_{12,34}=V_{34}/I_{12}$. Second, perform this measurement again on the perpendicular edges ($R_{23,41}$). Then R_S can be given by the following equation:

$$e^{-\pi R_{12,34}/R_S} + e^{-\pi R_{23,41}/R_S} = 1.$$

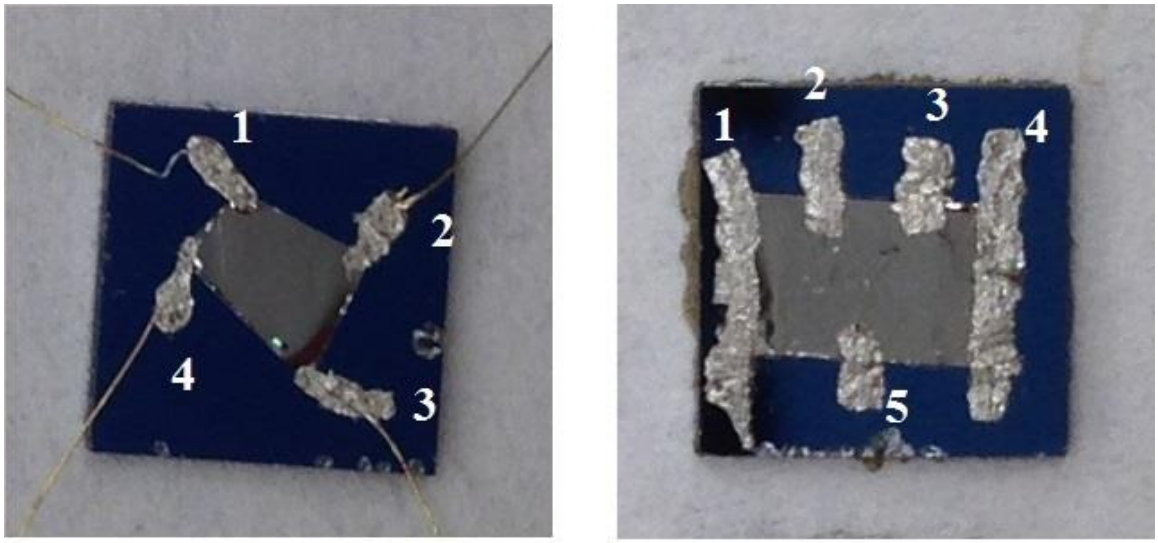

Figure 2-5 Van der Pauw geometry and Five-terminal geometry
Pictures of Van der Pauw geometry sample (left) and five-terminal geometry sample (right) on SiO2/Si substrate. The substrate size is 0.2 × 0.2 inch.

By solving this equation, one can obtain the sheet resistance R_S. Then the 3D resistivity can be calculated by $\rho_{3D} = R_S \cdot t$, where t is the sample thickness. For more accurate measurement, one can employ the following equation:

$$e^{-\pi R_{vertical}/R_S} + e^{-\pi R_{horizontal}/R_S} = 1,$$

where $R_{vertical} = (R_{12,34} + R_{34,12})/2$ and $R_{horizontal} = (R_{23,41} + R_{41,23})/2$. And further improvement in the accuracy can be make if $R_{vertical} = (R_{12,34} + R_{34,12} + R_{21,43} + R_{43,21})/2$ and $R_{horizontal} = (R_{23,41} + R_{41,23} + R_{32,14} + R_{14,32})/2$ are employed.

To measure the Hall effect, two different measurements are needed. First, apply a current through two opposite contacts (for example, contact 1 and 3, left figure in Figure 2-5), then monitor the Hall voltage change across the other two contacts (contact 2 and 4) when changing the perpendicular magnetic field from negative to positive. Second, switch the current leads to voltage

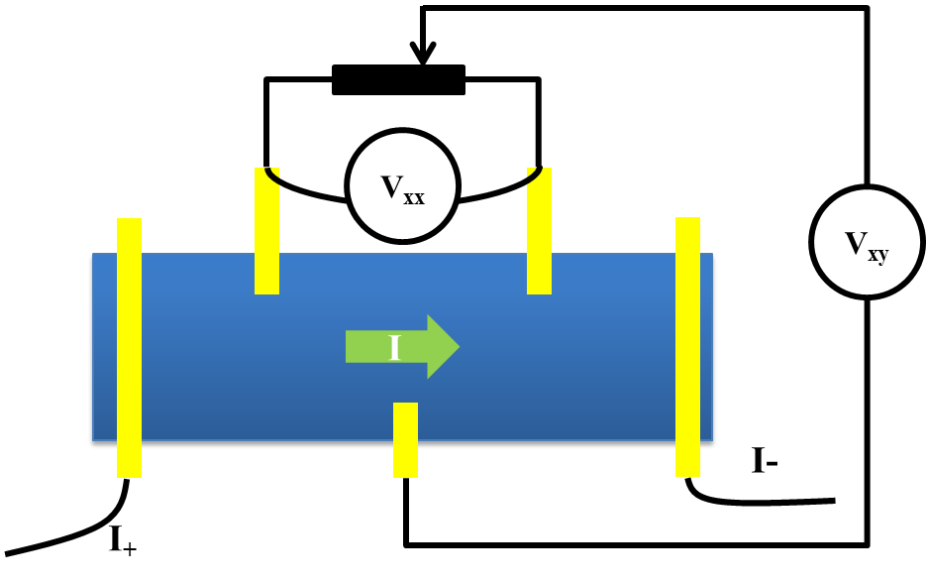

Figure 2-6 Schematic diagram of five-terminal geometry

leads, and voltage leads to current leads, then perform the measurement again. Theoretically, the Hall voltage as a function of perpendicular magnetic field should behave the same for both setups. Then average the measurements from both setups and carrier density can be extracted from the averaged value. To achieve accurate values, current with reversed direction needs to be applied. But this is not necessary for AC measurements.

For big thin flakes, the five-terminal geometry is employed. The flake is cut into rectangular geometry. Then indium dots are attached to the rectangular flake, as is shown in the left figure in Figure 2-5 and Figure 2-6. Contact 1 and 5 are the current leads. Contact 2 and 3 are for 4-terminal resistance measurement. If connecting contact 2 and 3 to a potentiometer, an electrical bridge forms. Then Hall effect can be measured by connecting the potentiometer and contact 5. By adjusting the potentiometer, one can get rid of the mix of longitudinal voltage and zero bias can be achieved between the potentiometer and contact 5 when no magnetic field is applied. By changing the magnetic field, Hall effect can be measured and carrier type and density can be extracted. When

performing Hall effect measurement, attention should be paid to the direction of current flow and magnetic field so as to figure out the carrier type in the materials.

2.1.4 Nanodevice Fabrication

Nanodevices are usually much thinner than the bulk samples (more than 1000 times). With less bulk channels and lower bulk carrier density, nanodevice is more preferred for the study of the topological surface state properties. Bi_2Se_3 and Bi_2Te_2Se nanoflakes are mechanically exfoliated by scotch tapes and placed on SiO_2/Si. However, the exfoliated flakes are not as thin as graphene. It is difficult to get extremely thin Bi_2Se_3 and Bi_2Te_2Se nanoflakes and optically difficult to identify the thickness of the nanoflakes. But when the nanoflakes are thin enough (<100 nm), the color starts to become dark. The thinner the nanoflake, the darker the color under optical microscope, especially after the spin-coating of electron beam resists. Figure 2-7 is an optical microscope image of Bi_2Se_3 nanoflakes after spin-coating of electron beam resists, methyl methacrylate (MMA) and poly(methyl methacrylate) (PMMA). Nanoflakes with purple colors are the thinnest ones while the yellowish color indicates thick flakes. Pink flakes have thicknesses between the purple ones and yellow ones.

A layer of MMA and PMMA are spin coated separately at a speed of 3600 rpm for 45 sec with the ramping rate of 10000 rpm/s (maximum rate). Then the substrate is baked on a hot plate after each spin coating. For MMA, the baking temperature is 150 ℃ and baking time is 5 min, while for PMMA, the baking temperature and time are 180 ℃ and 5 min. In order to reduce the influence of fabrication, after the patterning of alignment marks by e-beam lithography, the step of the metal deposition of alignment mark and respin-coating of resists is skipped. Thin nanoflakes are identified and the device electrodes are patterned directly. Although the contrast between resist

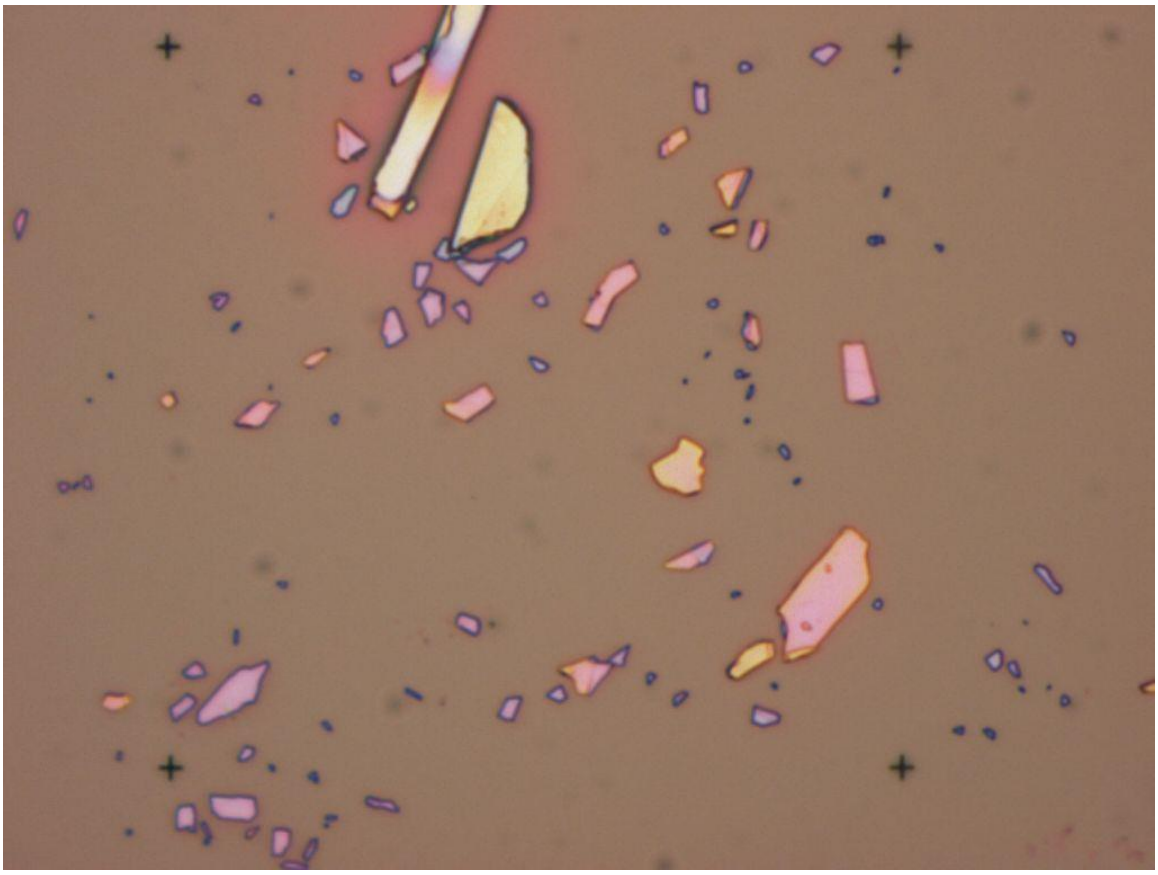

Figure 2-7 Optical image of TI nanoflakes after spin-coating
The length of each crossing mark is 2 μm. Brighter flakes are thicker while darker flakes are thinner.

and SiO_2/Si is not as strong as that between resist and metal under scanning electron microscope (SEM), the alignment marks can still be seen. After patterning device electrodes, electron beam evaporation is employed to deposit Ti/Au for device electrodes. However, a typical thickness of the topological insulator devices is over 100 nm. The thickness of the MMA resist layer is ~ 150 nm. In order to ensure the contacts are continuous, the electrodes should be thicker than the thickness of devices. But when it is higher than the MMA layer, electrode metal will have intimate contact with the PMMA layer. When the resist is lifted-off, electrodes will be more or less damaged. Then angle deposition is needed for the contact electrodes. Figure 2-8 is a schematic diagram of

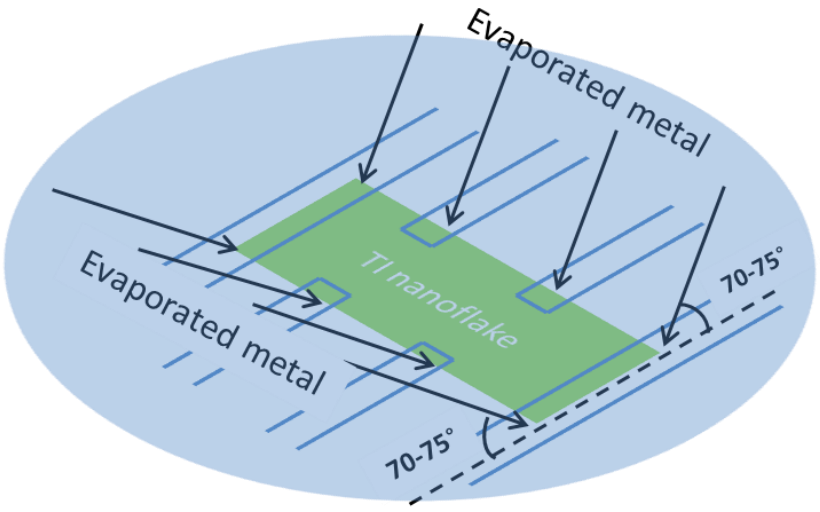

Figure 2-8 Schematic diagram of angle deposition
The entire wafer is coated with MMA/PMMA resist. Regions between blue lines are exposed to electron beam and developed. The black arrows in two different directions indicate the metal deposition direction. Both have a 70 °-75 °angle with the device plane.

the angle deposition. The electrode metal needs to be deposited twice with a thickness of 10 nm Ti and 60 nm Au in two different directions with respect to TI nanoflake's edges in order to get continuous electrodes. The black arrows in the Figure indicate the directions of the evaporation direction. It has a 70 – 75 °angle with the device plane but is perpendicular to the long edges of the device.

After device fabrication, we find that the fabrication process still increases the electron density in the device by a considerable amount although the process is already improved with fewer steps[11,54]. Then a completely new lithography-free device fabrication technique is developed in order to minimally influence device's carrier density. Without lithography processes, the quality of the device can be greatly improved.

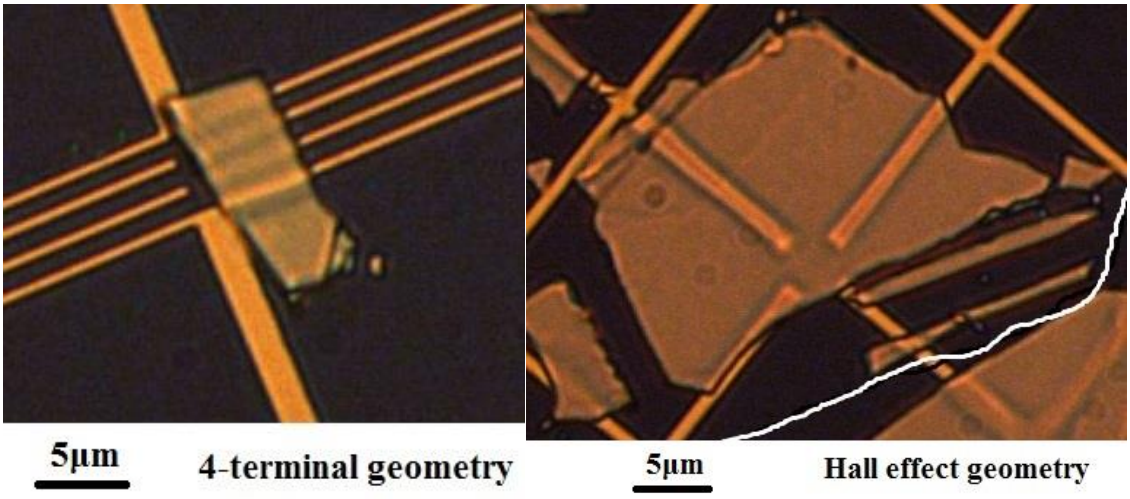

Figure 2-9 Optical images of lithography-free devices
Optical microscope images of devices fabricated with the lithography-free technique. Left, a device image with 4-terminal geometry electrodes. Right, a device image with Hall effect geometry electrodes.

Two sets of electrodes with either four-terminal geometry or Hall effect geometry are prepatterned and deposited on empty SiO_2/Si substrates. Then topological insulator nanoflakes are mechanically exfoliated on to the prepatterned electrodes. The exfoliation step may be repeated if no flakes are found on the electrodes. Devices fabricated by this method are expected to show high quality since this technique can be considered as a method to fabricate suspended devices, which is free of resist and avoid contact with substrate. The device experiences less charge impurity scatterings from the substrates and thus exhibits high mobility. Moreover, the surface states will be less affected.

2.2 Bi_2Se_3 Bulk samples

2.2.1 Fourier Transform Infrared Spectroscopy

The single crystal growth and bulk sample preparations are described in section 2.1.3. After thin flakes are peeled off from the single crystal and before bulk sample preparation for electrical

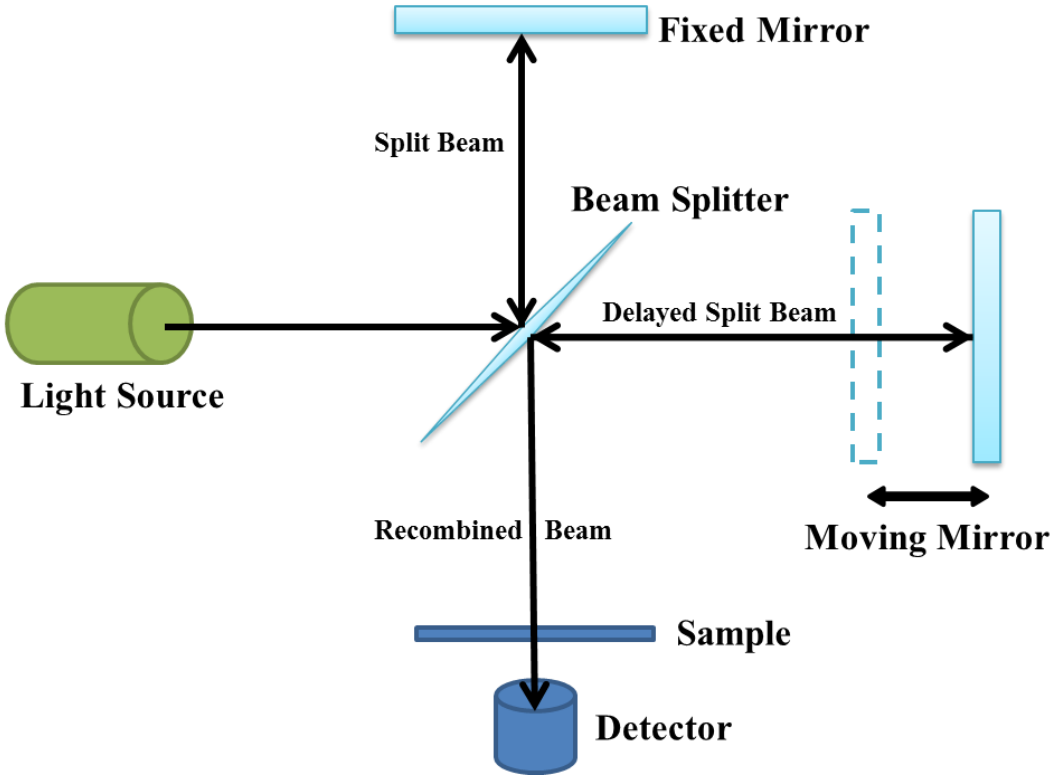

Figure 2-10 Schematic diagram of FTIR spectroscopy

transport measurement, room temperature Fourier Transform Infrared (FTIR) spectroscopy is performed on the flakes to determine the flake thickness and the relative Fermi level position.

Figure 2-10 is the experimental setup of FTIR spectroscopy. The transmittance *T* and reflectance *R* are both recorded within the range of wavenumbers from 400 cm^{-1} to 7000 cm^{-1}. However, the instrument's cut-off frequency in the lower limit is 500 cm^{-1}. A sharp decrease can be observed when the wavenumber is approaching 500 cm^{-1} in both Reflectance and Transmittance spectra.

Figure 2-11 is a typical reflectance *R* spectrum of a thin Bi_2Se_3 flake. In the low frequency (< 1000 cm^{-1}) range, there is a deep (~ 780 cm^{-1}) in *R*, which represents the plasma frequency of the sample. With equations below, carrier density can be estimated.

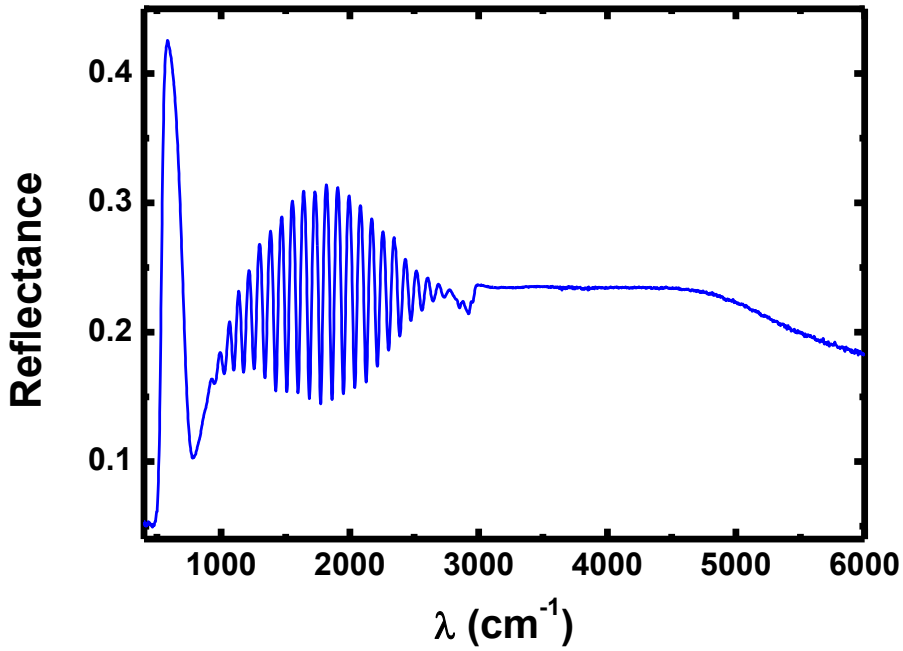

Figure 2-11 Reflectance spectrum of Bi_2Se_3

$$\omega_{pe} = \sqrt{\frac{n_e e^2}{m^* \varepsilon_0 \varepsilon_r}}$$

$$n = \frac{\omega_{pe}^2 m^* \varepsilon_0 \varepsilon_r}{e^2},$$

where ω_{pe} is the plasma frequency, m^* is the electron effective mass, ε_0 is vacuum permittivity, and ε_r is the dielectric constant.

In the high frequency range (> 3000 cm^{-1}), R stays as a constant but with a slight decrease which is due to the inaccuracy of the instrument sensor. The R at high frequency can be used to calculate the dielectric constant by the following equations,

$$R = \left(\frac{n_1 - n_2}{n_1 + n_2} \right)^2 .$$

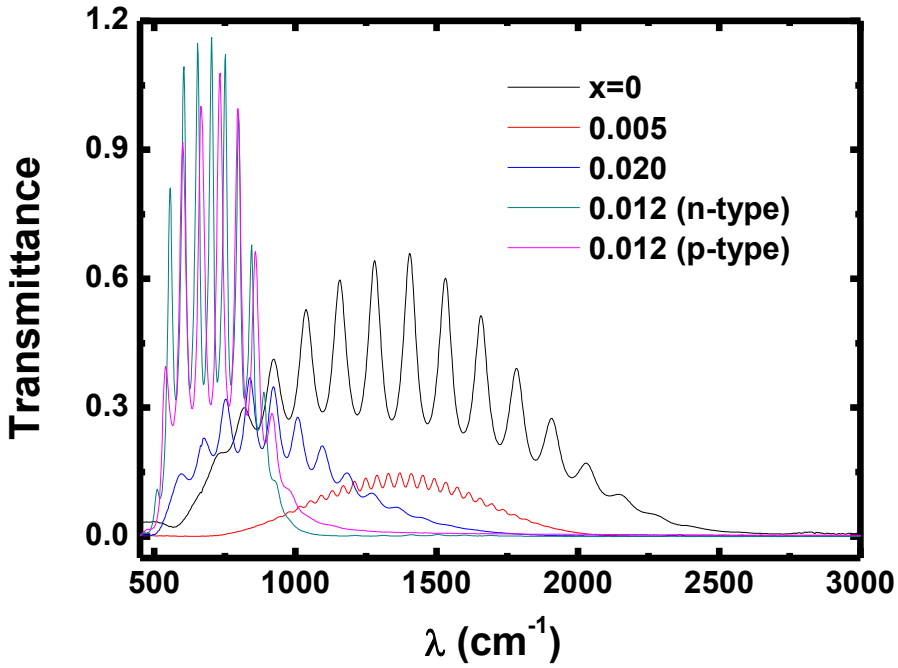

Figure 2-12 Transmittance spectra of $Ca_xBi_{2-x}Se_3$

The FTIR transmittance and reflectance (Figure 2-14) spectra are measured at room temperature. *T* spectra on flakes with different doping levels are shown.

The infrared light is incident from air to the flake, then $n_1 \approx 1$ and $n_2 = \sqrt{\mu\varepsilon} \approx \sqrt{\varepsilon}$, where $\mu \approx 1$ in Bi_2Se_3. Then one have

$$\varepsilon = n_2^2 = \left(\frac{1+\sqrt{R}}{1-\sqrt{R}}\right)^2,$$

where *R* should be the reflectance with infinite frequency, but here high frequency *R* can be used as an approximation. The high frequency *R* from different samples are extracted and averaged. Plug the averaged value in the equation, one can get the dielectric constant for my Bi_2Se_3 samples, which is $\varepsilon_r = 9$ and the refractive index is $n = 3$.

In the intermediate range (1000 – 3000 cm^{-1}), there are interference fringes in *R* which are a result of the Fabry-Perot interference of the infrared light reflected by the two flat specular surfaces

of the flake (top and bottom surfaces). The interference fringes can be used to determine the flake's thickness as follows. The Fast Fourier Transform is performed on the oscillation part. Then usually a single peak can be obtained after the Fast Fourier Transform. This peak position represents the optical path difference of the infrared light reflected by the top and bottom surfaces of the flake, which is twice of the flake thickness that the light travels. One can have a relationship between the peak position, P, and the flake's thickness, t, $P = 2t \cdot n$, where n is the refractive index of the flake. Several different spots are measured within the same flake to get an averaged value for the thickness.

The curves in Figure 2-12 are typical transmittance T spectra of a Bi_2Se_3 flake with different Ca doping levels. In the lower limit (~ 500 cm^{-1}), T decreases to zero due to the cut-off in detector's sensitivity. And in the high wavenumber range (> 3000 cm^{-1}), T goes to zero, as well. The infrared photon energy in the high wavenumber range is large enough for the interband transition of electrons in Bi_2Se_3 samples. The light is all adsorbed except for the reflected part, resulting in zero transmitted signals. In the intermediate range, T stays finite with oscillations. The highest wavenumber with finite T marks the onset of the interband transition, and it corresponds to the minimum interband transition energy E_0 which is determined by the Fermi level position, bulk band gap, and the effective masses of carriers. Pure Bi_2Se_3 is n-type and its Fermi level resides in the conduction band, Figure 2-13**a**. E_0 is the energy of the electron excited from valence band to Fermi level in the conduction band. And the initial and final states should have the same wave vector according to the selection rule. The oscillation part, same as the reflectance spectrum, is due to the Fabry-Perot interference. The same method of determining flake's thickness in R spectrum can be applied to the T spectrum. Thickness extracted from T spectrum is consistent with that from R spectrum.

As-grown pure Bi_2Se_3 single crystals have high Se vacancy concentration and thus high electron density, leading to an upshift of Fermi level and high bulk conductivity with metallic

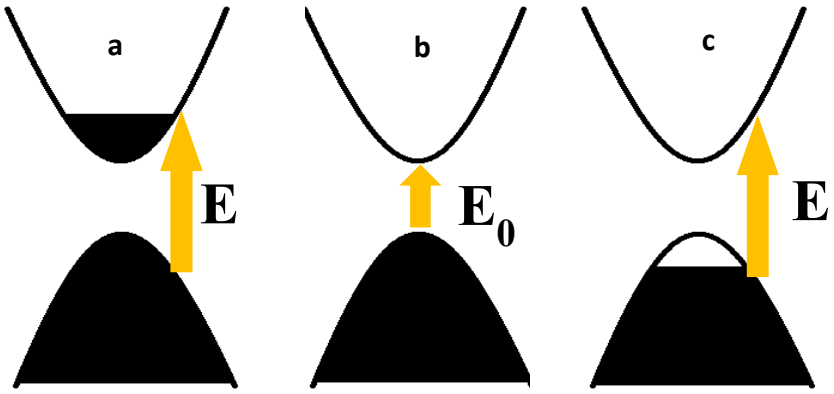

Figure 2-13 Fermi level revolution in Ca-doped Bi_2Se_3
a, as-grown undoped Bi_2Se_3, the Fermi level is in the conduction band. **b**, with $x = 0.012$ in $Ca_xBi_{2-x}Se_3$, the Fermi level is pulled into the band gap. **c**, As Ca concentration is continued to increase, the Fermi level is further pulled down into the valence band. Black areas are filled states.

behaviors, Figure 2-13**a**. In order to reduce the conducting bulk channels, Ca is added to the system to reduce excess electrons. Ca replaces Bi atom, which can be written in the form of $Ca_xBi_{2-x}Se_3$. Then transmittance spectra are obtained for $Ca_xBi_{2-x}Se_3$ flakes with different Ca doping levels, as is shown in Figure 2-12. For undoped Bi_2Se_3, it has the highest onset interband transition energy E_0, which is 2400 cm^{-1} or 0.30 eV. As the doping level is increased, E_0 decreases due to the decrease in carrier density and thus the downward shift of Fermi level. It reaches a minimum at $x = 0.012$. This point is defined as the compensation point, Figure 2-13**b**. When the doping level is further increased ($x > 0.012$), E_0 starts to increase since Fermi level is moved into valence band and carrier changes type from electrons to holes and its density starts to increase, Figure 2-13**c**. The change of the position of the Fermi level as the increase of Ca doping level can be explained in Figure 2-13.

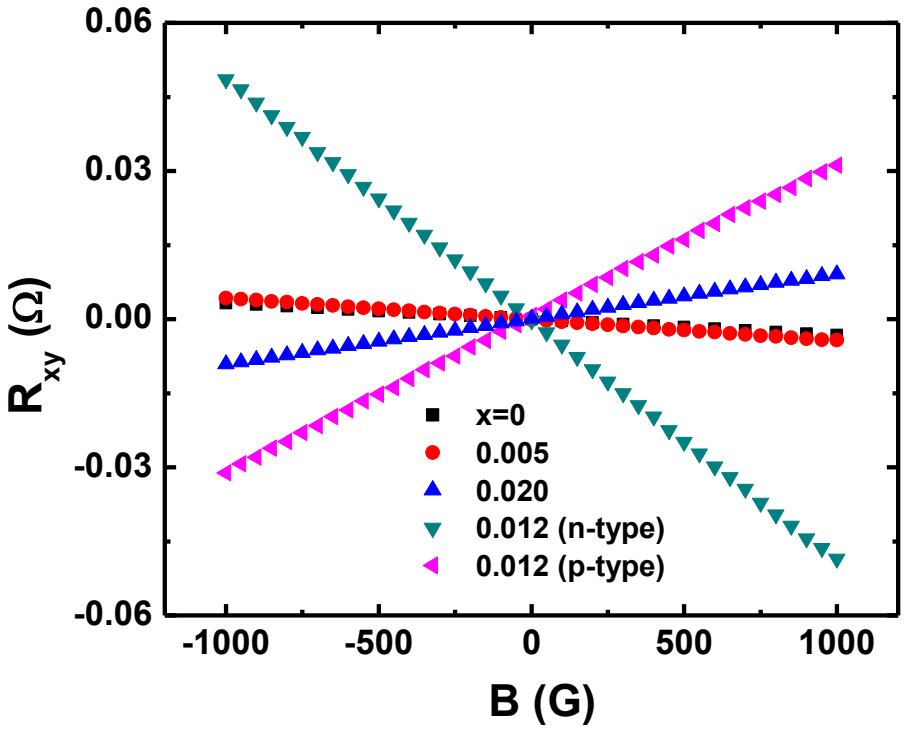

Figure 2-14 Hall effect in $Ca_xBi_{2-x}Se_3$

The Hall effect measurement in different $Ca_xBi_{2-x}Se_3$ flakes is performed at room temperature. Negative slope means the major carriers are electrons while positive slope represents holes.

2.2.2 Electrical Transport Properties

Hall effect is measured on Bi_2Se_3 samples with different Ca-doping levels. Figure 2-14 is a set of the Hall effect curves from samples with different doping levels. Straight lines in Hall effect are obtained. The Hall signal for undoped Bi_2Se_3 has a negative slope. And it has the smallest value among all the samples. The 2D carrier density n_{2D}, which is inversely proportional to the slope, is then extracted,

$$n_{2D} = \frac{1}{e \cdot slope}$$

And the 3D carrier density n_{3D} can immediately be calculated by using sample's thickness t, $n_{3D} = n_{2D}/t$. The 3D carrier density for pure Bi_2Se_3 is $n_{3D} \sim 5\times10^{18}$ cm^{-3}. As Ca concentration is increased, the absolute value of the negative slope grows bigger and bigger, and the slope eventually changes sign when passing through the compensation point. In the meantime, n_{3D} reaches minimum at the compensation point $x = 0.012$. However, as mentioned in the previous section, there is sample-to-sample variation during the growth process. Both n- and p-type are observed in $Ca_xBi_{2-x}Se_3$ sample when $x = 0.012$. The lowest carrier density is $\sim 4\times10^{17}$ cm^{-3} with a sample-to-sample variation of $\sim 5\times10^{17}$ cm^{-3}. The variation in both carrier density and type strongly indicates the spatial inhomogeneity of Ca concentration, which is more significant in low carrier density samples near the compensation point.

Table 1 E_0 and n_{3D} in $Ca_xBi_{2-x}Se_3$

x ($Ca_xBi_{2-x}Se_3$)	n_{3D} (cm^{-3})	E_0 (eV)
0.005	-6.08×10^{18}	0.287
0.005	-5.51×10^{18}	0.257
0.012	-3.52×10^{17}	0.119
0.012	7.66×10^{17}	0.131
0.014	2.00×10^{18}	0.168
0.019	2.75×10^{18}	0.189
0.020	3.62×10^{18}	0.205

With the E_0 estimated from the transmittance spectra and n_{3D} determined from Hall effect measurement on samples with different Ca doping levels, the relationship of E_0 and n_{3D} can be established. And the plot of E_0 with respect to n_{3D} is shown in Figure 2-15. n_{3D} with negative values

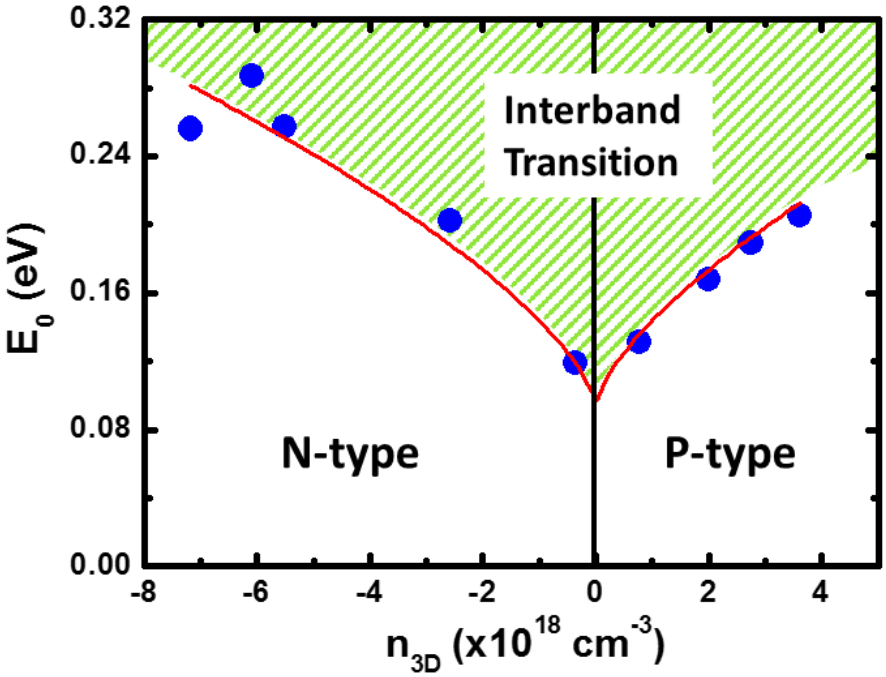

Figure 2-15 Relationship between E_0 and n_{3D}

Red line is a best fit to the relationship of E_0 and n_{3D}. Negative values in n_{3D} represents electron carriers while positive stands for hole carriers. Green shadowed region is the regime where interband transition happens.

means electron carrier type while positive values corresponds to hole carrier type. The reduced effective mass is define as μ^*, where $\mu^* = \frac{m_c \cdot m_v}{m_c + m_v}$. With the help of Figure 2-13, the relationship between the onset interband transition energy E_0 and bulk bandgap E_g can be deduced,

$$E_0 = E_g + E_c + E_v = E_g + \frac{\hbar^2 k_F^2}{2m_c} + \frac{\hbar^2 k_F^2}{2m_v} = E_g + \frac{\hbar^2 k_F^2}{2\mu^*} = E_g + \frac{\hbar^2 (3\pi^2 n_{3D})^{\frac{2}{3}}}{2\mu^*}$$

The red line in Figure 2-15 is the best fit of $E_0 = An^{2/3} + B$ to the data. And above the red line, the green shadowed region is the regime where the interband transition takes place. Then E_g and μ^* can be readily extracted from the fitting parameters. One have E_g = 0.093 eV and μ^* = 0.072 m_e, where m_e is the free electron mass. It is noted that the extracted E_g from E_0 and n_{3D} is smaller than

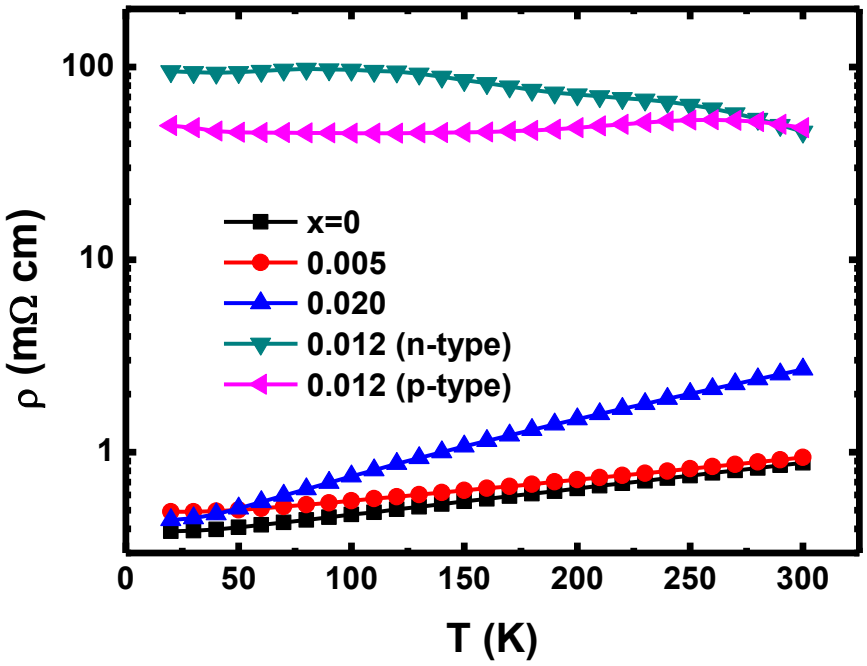

Figure 2-16 Temperature dependence of ρ_{3D} in $Ca_xBi_{2-x}Se_3$
The figure is plotted as a semi-log style in order to see the change of more than 2 orders in magnitude in the resistivity.

the theoretical value[15] 0.3 eV at 0 K or ARPES data[16] at 4 K. But this is very close to other experimental works[55,56]. Moreover, the reduced effective mass agrees with values in previous works[55,57]. It needs to be pointed out that the extracted bulk bandgap is a value at room temperature. This value should be smaller than the theoretical value at low temperature due to thermal excitations, as well as the band broadening from impurities and disorder.

The 3D carrier density spans over an order of magnitude for different. Table 1 is a list of n_{3D} and E_0 in samples with different doping levels. For samples with the lowest n_{3D}, it can be inferred from the transmittance spectra that the Fermi level is only ~25 meV (wavenumber form FTIR) above the top of the valence band (p-type) or below the bottom of the conduction band (n-type). An insulating temperature behavior is expected in samples with the lowest n_{3D}. The resistivity

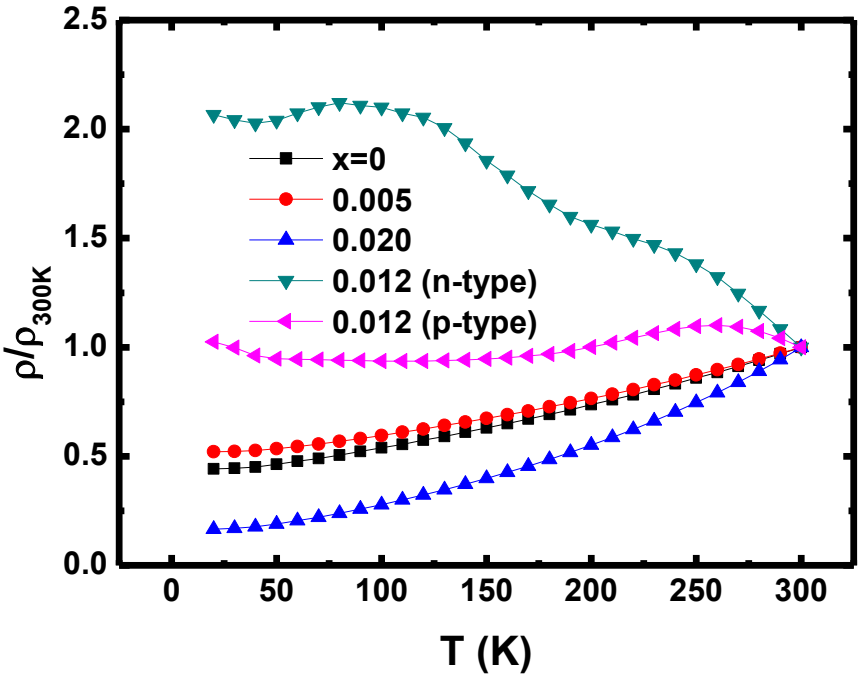

Figure 2-17 Temperature dependence of normalized ρ_{3D} in $Ca_xBi_{2-x}Se_3$
The ρ_{3D} is normalized with the value at 300 K and plotted as a function of temperature. The relative change in ρ_{3D} as temperature is clear to see.

measurements are performed on 5 samples with different Ca doping levels, which is shown in Figure 2-16. The 3D resistivity ρ_{3D} of different samples covers about 2 orders in magnitude at room temperature. The most resistive samples are at the compensation point where x = 0.012. The corresponding n_{3D} are -7.1×10^{17} cm^{-3} (n-type) and $+1.6\times10^{18}$ cm^{-3} (p-type). The resistivity either increases or stays almost unchanged when the temperature decreases, suggesting an insulating behavior. For the undoped Bi_2Se_3 samples and samples with other Ca doping levels, for example x=0.005, 0.020, ρ_{3D} is small at room temperature and decreases as the temperature decreases, exhibiting a metallic behavior. Such significantly difference in temperature behaviors can be attributed to the carrier density variation when the temperature is decreased. The normalized

resistivity (ρ/ρ_{300K}) temperature dependence is presented in Figure 2-17. The relative change in ρ_{3D} from room temperature to 20 K can be clearly seen.

2.2.3 Shubnikov-de Haas Effect

The topological surface states with strong spin-orbit coupling and the protection of time-reversal symmetry prohibiting backscattering carriers are superior to the bulk states. The surface states are predicted to have high carrier mobility while the bulk only has relatively low carrier mobility. To study the properties of the surface states in Bi_2Se_3, the Shubnikov-de Haas (SdH) effect measurement is performed which can easily detect high mobility channels even with the presence of low mobility ones. Several SdH effect studies are performed, attempting to reveal the topological surface states in TIs[21,57-68].

SdH effect is the quantum oscillations that require low temperature and high magnetic field. Under high magnetic field, the electron states are split into discrete Landau levels which are degenerate with the number of electrons directly proportional to the magnetic field. Considering that there is no spin degeneracy in topological insulator surface states due to the strong spin-orbit coupling, the carrier density required to fully fill each Landau level at a specific perpendicular magnetic field B is $n_{L.L.} = \frac{eB}{h}$. With a 2D carrier density $n_{2D} = \frac{\pi k_F^2}{(2\pi)^2} = \frac{k_F^2}{4\pi} = \frac{A_e}{4\pi^2}$, where A_e is the area of the cross-section of the Fermi surface perpendicular to the magnetic field, the number of fully-filled Landau levels is $N_{L.L.} = \frac{n_{2D}}{n_{L.L.}} = \frac{h}{eB} n_{2D} = \frac{B_0}{B}$, where $B_0 = \frac{h}{e} n_{2D} = \frac{\hbar}{2\pi e} A_e$. With a changing magnetic field, the Landau level at the Fermi surface is changing from empty to half-filled, and to fully-filled. One reflection of this change is the oscillations in resistance when subjecting a changing magnetic field. In order to change the numbers of Landau level from *N+1*

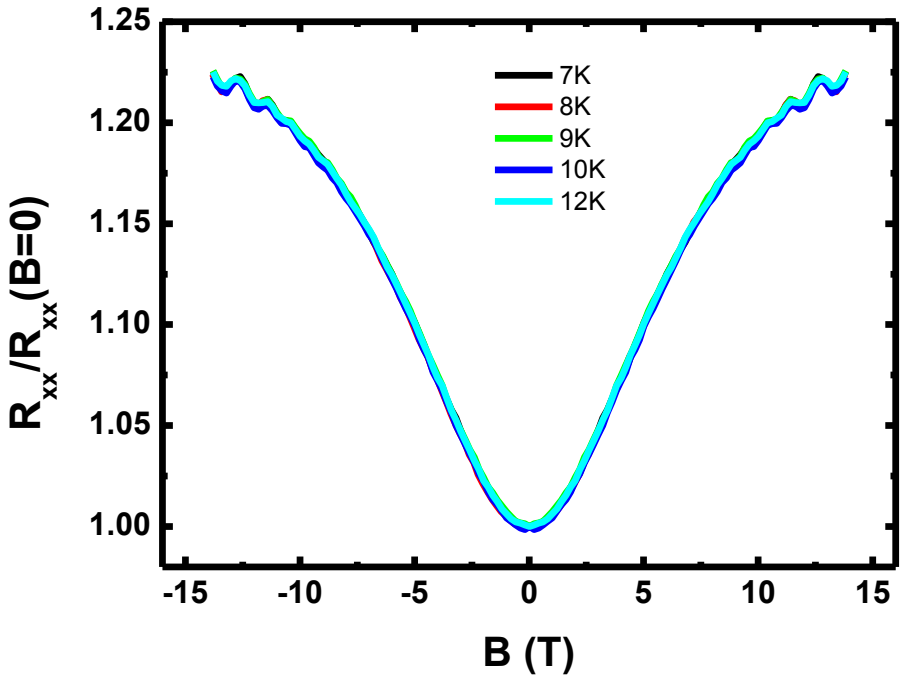

Figure 2-18 MR in an undoped Bi_2Se_3

The magnetoresistance in an undoped Bi_2Se_3 flake is measured from 7 K to 12 K in a perpendicular magnetic field up to 14 T.

to N, the magnetic field should change from $B_{N+1} = \frac{B_0}{N+1}$ to $B_N = \frac{B_0}{N}$, or from $\frac{1}{B_{N+1}} = \frac{N+1}{B_0}$ to $\frac{1}{B_N} = \frac{N}{B_0}$. Then one can get the period in $\frac{1}{B}$ is $\Delta\left(\frac{1}{B}\right) = \frac{1}{B_0} = \frac{2\pi e}{\hbar}\frac{1}{A_e}$, which is also the oscillation period in the magnetoresistance.

The SdH effect measurement is performed in a Quantum Design Physical Property Measurement System (PPMS). A perpendicular magnetic field is applied to the sample plane. Lock-in amplifiers are used for 4-terminal resistance and Hall effect measurements. At very low temperatures, oscillations can be found in magnetoresistance in the high magnetic field range (>7 T). Figure 2-18 is the magnetoresistance of an undoped Bi_2Se_3 sample at different temperatures. Here only the undoped sample is studied because it has high carrier density and the surface states

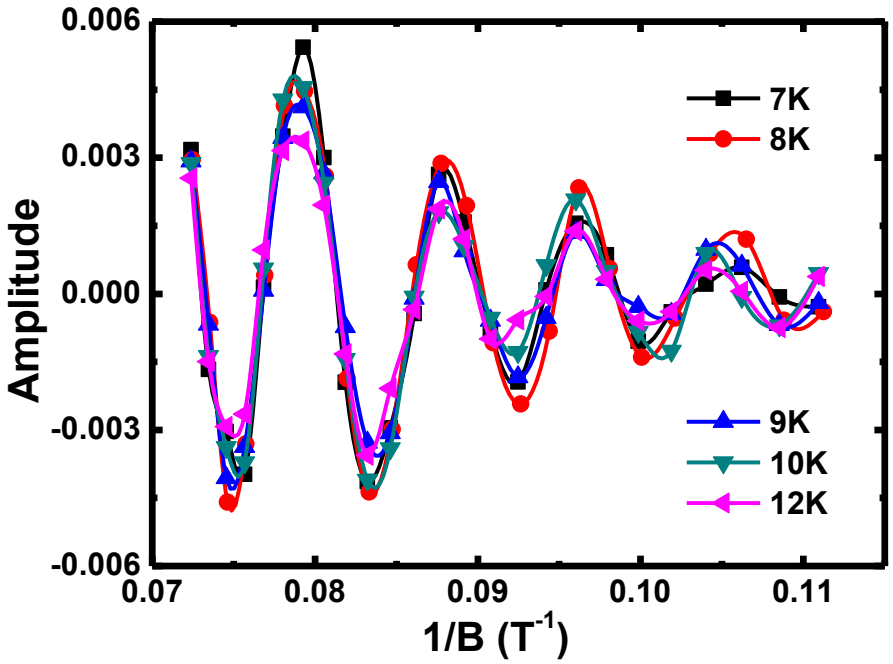

Figure 2-19 SdH oscillations at different temperatures
Once the normal magnetoresistance background is removed, the SdH oscillations are obtained. From 7 K to 12 K, the amplitude of the oscillations decreases.

are fully filled so that it is easier to realize more oscillations in the measurable field range. Furthermore, since the undoped sample has low resistance, the amplitude of small changes caused by the SdH oscillations can be easily observed. The SdH oscillations start to appear when the magnetic field reaches 8 T. There is an empirical estimation of the mobility with the knowledge of the onset SdH oscillation field, which is $B \cdot \mu \sim 1$, where μ is the mobility. With 8 T onset SdH oscillation field, the mobility is estimated to be $\mu \sim 1/8$ m^2/Vs or 1250 cm^2/Vs. As the magnetic field increases, the amplitude of the SdH oscillation grows. But there is always a non-oscillating background. The non-oscillating magnetoresistance background can be removed by a polynomial fit to the overall curve. After the background is carefully removed, SdH oscillations are obtained. Figure 2-19 is the SdH oscillations with respect to the inverse of the magnetic field, *1/B*.

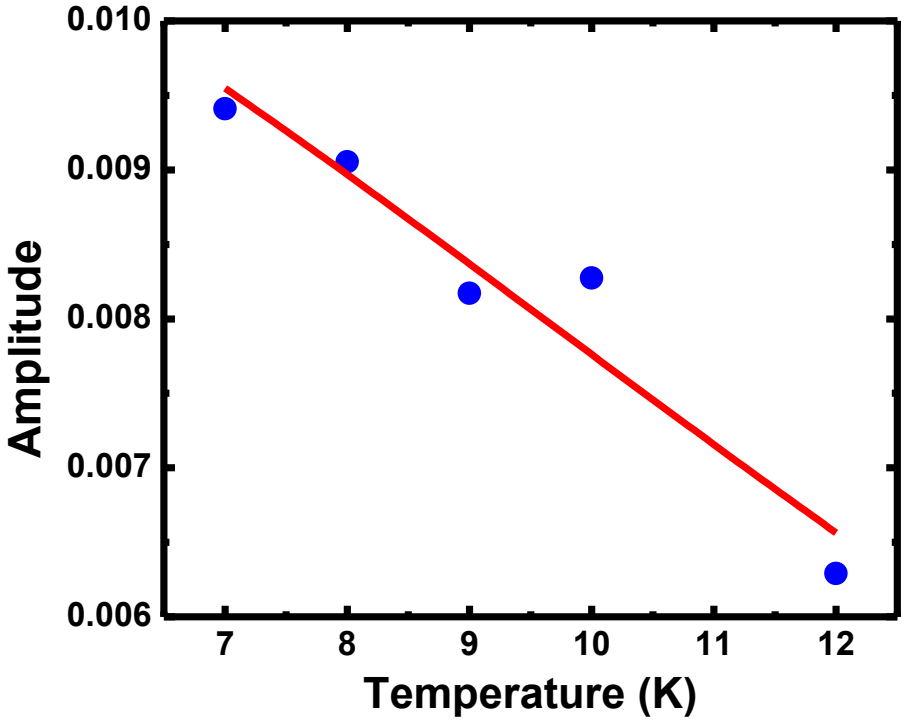

Figure 2-20 SdH oscillation amplitude as a function of *T*
The amplitude of the SdH oscillations around *B* = 13 T is plotted with respect to temperature. The red line is a best fit to the data of the equation shown in the main text.

For a specific carrier density, the fully-filled Landau level number is a periodic function of *1/B*. So the oscillations are a periodic function of *1/B*. And the period is related to the area of the cross-section of the Fermi surface perpendicular to the magnetic field. In order to extract the period, Fourier Transform is performed on the oscillation part. A single peak is obtained afterwards, representing only one set of oscillations is detected. And the peak position is the oscillation frequency in Tesla. Using the equations above, one can calculate the wavevector k_F and the 2D carrier density n_{2D}, $n_{2D} = 2.4\times10^{12}$ cm^{-2} and $k_F = 5.5\times10^{6}$ cm^{-1}. The 2D carrier density calculated from the Hall effect in this sample is $n_{2D} = 3.85\times10^{16}$ cm^{-2}, which is much higher than that extracted from the SdH oscillations. So the SdH oscillation should originate from the surface states.

Moreover, if the SdH oscillations are a result of the bulk carriers, assuming that the Fermi surface is a sphere for the bulk states (the Fermi surface is an infinite cylinder for the surface state), then the 3D carrier density can be estimated, $n_{3D} = 2.8 \times 10^{18}$ cm^{-3}, which is much smaller than the typical 3D carrier density for the undoped samples. This futher confirms that the SdH oscillations are from the surface state carriers.

More information can be extracted from the SdH temperature dependence, the oscillation amplitude is a function of temperature,

$$Amp = 4\exp\left(-2\pi k_B T_D/\hbar\omega_C\right)\frac{-2\pi k_B T/\hbar\omega_C}{\sinh\left(-2\pi k_B T/\hbar\omega_C\right)}$$

Figure 2-20 is a plot of the amplitude as a function of temperature. The amplitude of the oscillations becomes smaller and smaller as temperature increases. According to the equation above, a best fit to the curve is performed. From the fitting parameters, the effective mass m^* and Dingle temperature T_D are extracted, $m^* = 0.142$ m$_e$, $T_D = 35$ K. The effective mass is consistent with the results in previous works[55,57]. Since $m^* v_F = \hbar k_F$, one can have $v_F = \frac{\hbar k_F}{m^*} = 4.5 \times 10^5 m/s$. With the value of Dingle temperature, the relaxation time can be obtained by using the equation,

$$\tau_D = \frac{\hbar}{2\pi k_B T_D} = 3.5\times10^{-14} s,$$

which is consistent with previous works[57,59,60,64,69]. Then the mean-free path of the surface state carriers can be calculated, $\ell = v_F \tau_D = 16\, nm$. Then the mobility can be estimated with the equation $\mu = \frac{e\tau_D}{m^*} = \frac{e\ell}{\hbar k_F} = 441\ cm^2/Vs$. With the mobility and 2D SdH carrier density, one can obtain the 2D conductivity of this surface channel with Drude's model, which is $\sigma_{2D} = ne\mu = 0.169$ mS. Compared to the overall 2D conductivity in this sample is $\sigma_{2D} \sim 11$ S, it is only 1.5%, which means the surface states only take up 1.5% in the undoped samples.

2.3 Bi_2Se_3 Nanodevices

2.3.1 Lithography-Free Technique

The major factor that leads to high electron density in as-grown Bi_2Se_3 single crystals is believed to be the large amount of Se vacancies. During the Bi_2Se_3 device nanofabrication process, heating, electron beam exposure, and other process have the tendency to promote the formation of Se vacancies. To overcome this problem, the regular lithography process is intentionally bypassed and develop a lithography-free technique for device fabrication[54].

Prepatterned Ti/Au (10 nm/40 nm) electrodes are deposited on 290 nm SiO_2 atop highly doped Si substrate first and then followed by the exfoliation of Bi_2Se_3 nanoflakes onto the prepatterned electrodes. Two types of the electrodes are fabricated. As is illustrated in Figure 2-21, one is four-parallel 0.7-μm-wide electrodes separated by 1 μm, which is good for 4-terminal resistance measurement, Figure 2-21**a**. The other one is two orthogonal "crossed" electrodes with 4-μm^2-square gap right in the center, which is suitable for Hall effect measurement, Figure 2-21**b**. Optical microscope images of another two lithography-free devices are shown in Figure 2-9.

Nanoflakes only with suitable size and thickness are chosen for electrical transport characterizations. The typical thickness range is 100 – 200 nm. The measurement is performed with Stanford Research SR830 Lock-in amplifiers in an Oxford ^{3}He cryogenic superconducting magnet system. The temperature range is from 1.5 K to 300 K. And the magnetic field can reach up to 8 T. The contact resistance in devices fabricated by this technique is < 10 kΩ, which is stable at low temperatures and after several thermal cycles.

The device's thickness is determined by atomic force microscopy (AFM) in a Veeco Dimension 5000 system. Figure 2-22**a** is the AFM topographic images of the device showing in Figure 2-21**a**. The green and blue lines in the figure indicate two scans on the device, the green line

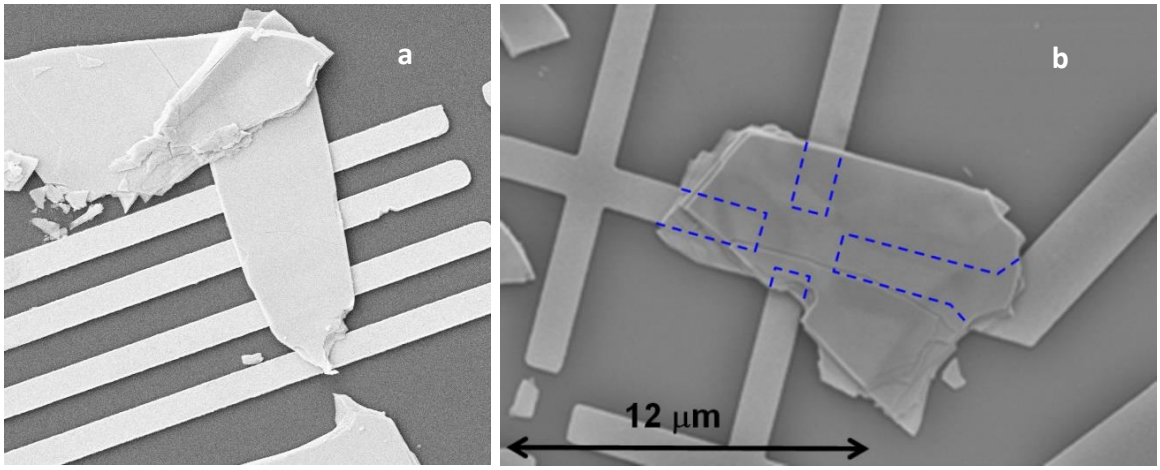

Figure 2-21 SEM images of lithography-free devices
a, a device with four-parallel electrodes. **b**, a device with Hall effect electrodes, blue dashed lines are indications of the electrodes shape profile.

is a scan on the device with the substrate background while the blue line is the one with the electrode background. Figure 2-22**b** is the thickness profiles of the two scans in green and blue lines. The two thicknesses are ~ 210 nm and ~ 160 nm, respectively. The one with the electrode background gives the thickness of the device, ~ 160 nm. The difference in the thickness of the green and blue scans is the electrode thickness (10 nm Ti and 40 nm Au). From both the topographic image and the thickness profiles, the device surface is flat, representing good device quality. And there is a 50-nm gap between the device and substrate (electrode thickness), indicating a suspended device structure.

This lithography-free technique can effectively reduce the excess electrons introduced during the normal fabrication process. Devices from the optimally doped $Ca_xBi_{2-x}Se_3$ ($x = 0.012$) insulating bulk samples show insulating behavior, indeed. But there is device-to-device fluctuation. Some of the devices still show metallic or weak insulating behaviors. This is probably due to the spatial inhomogeneity of the Ca distribution[49,50] and different exposure time to the atmosphere[70]. It is known that oxygen and water can be absorbed on TI's surface and dope the device, which always

increases

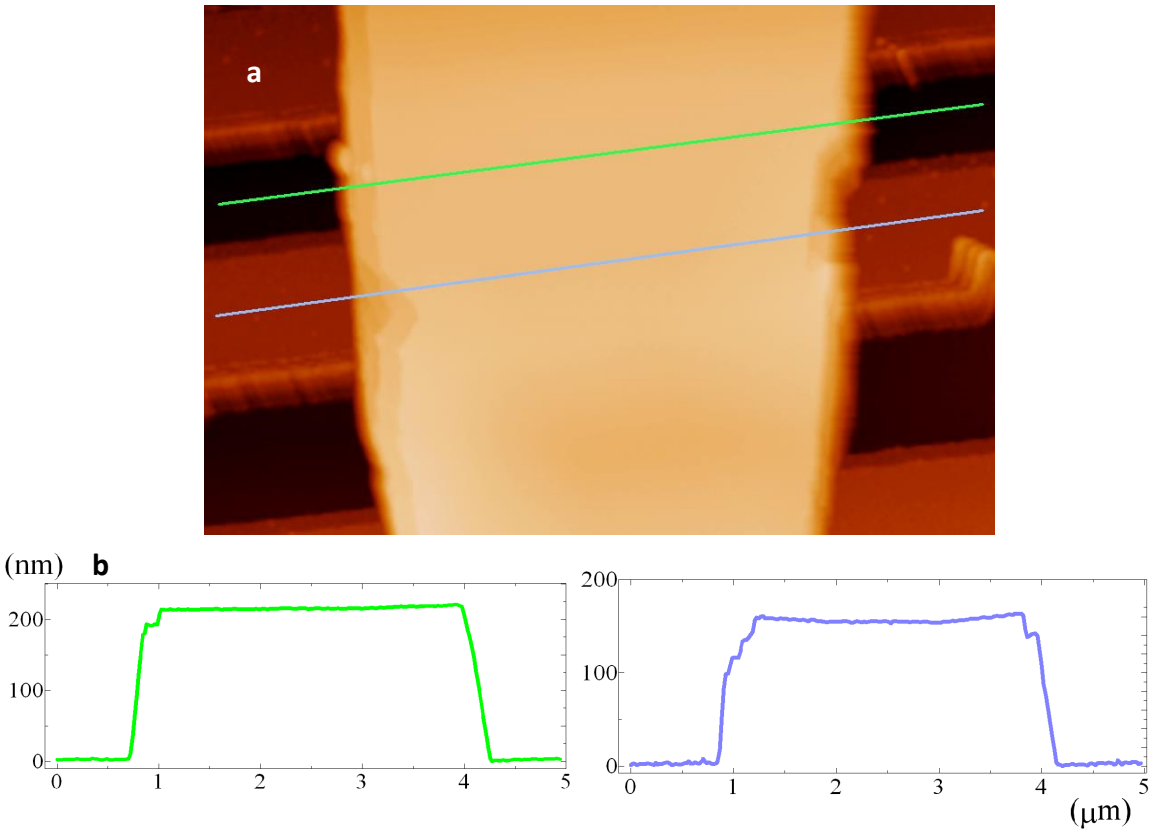

Figure 2-22 AFM on a lithography-free device

a, AFM topographic image of the device showing in Figure 2-24**a**. **b**, the thickness profiles of two scans marked on **a**. The green line is scanned on the area with substrate background. The blue line is scanned on the area with electrode background. The height scanned from the blue line is the device thickness and the difference between the green and blue lines are the electrode thickness.

the electron density. Figure 2-23 is the 2D resistivity ρ_{2D} of 3 devices from the same single crystal. Device S_2 and S_3 show insulating temperature behaviors while Device S_1 is metallic (S_1(M)). After post-treatment which will be discussed later, S1 shows insulating temperature features (S_1(I)). There is resistivity upturn in both S_1(I) and S_2's resistivity temperature curves, which is similar to that of the insulating bulk flakes.

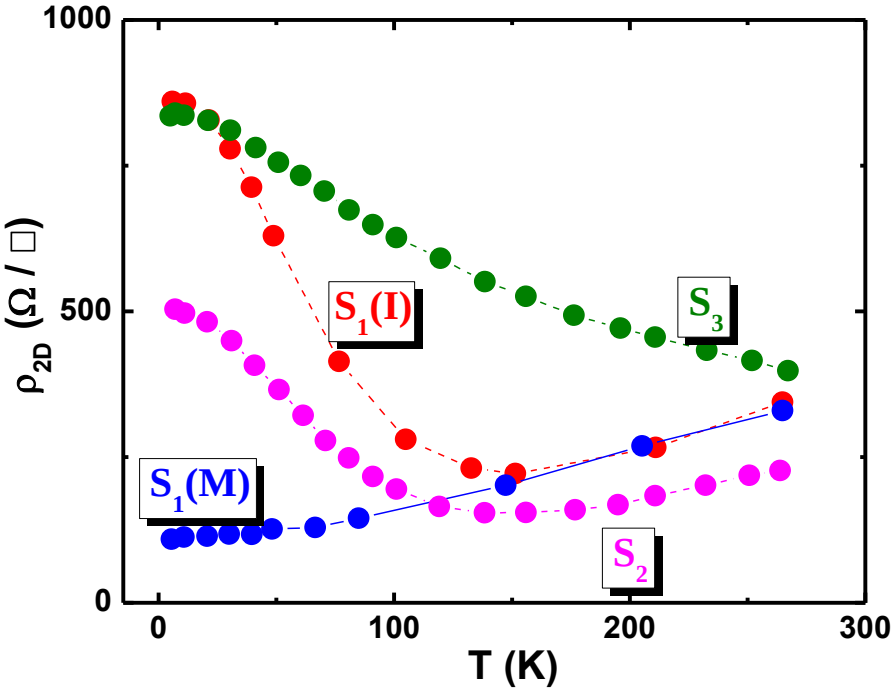

Figure 2-23 Temperature dependence of ρ_{2D} in 3 devices
These 3 devices are from the same single crystal. S1 shows a metallic temperature behavior, S2 exhibits a weak insulating behavior and S3 is insulating. After post-treatment which will be discussed later, S1 turns to weak insulating.

2.3.2 Electron Beam Irradiation

Since there is uncertainty in device fabricated from the optimally doped bulk samples, to overcome this problem, the slightly overdoped p-type $Ca_xBi_{2-x}Se_3$ (for example, x = 0.015 and the corresponding n_{3D} is ~ 2×10^{18} cm^{-3}) starting bulk material is intentionally selected for device exfoliation. As mentioned previously, the electron beam exposure always unavoidably increases the electron density in the device during the fabrication process[11]. Oppositely, one can utilize this property of electron beam exposure to compensate for the hole carriers in p-type devices. This is another reason why the slightly overdoped p-type $Ca_xBi_{2-x}Se_3$ starting material is selected.

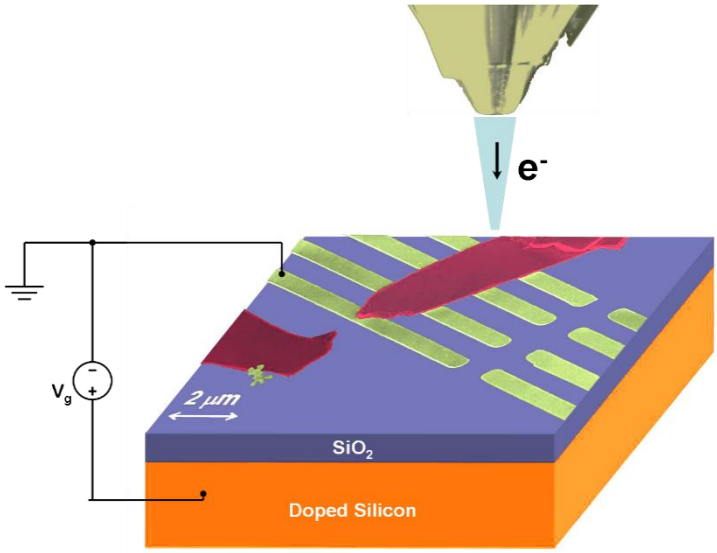

Figure 2-24 Schematic diagram of electron beam irradiation
The device is grounded and no gate voltage is applied while electron beam is scanned. The figure is of false color.

Moreover, the Dirac point is closer to the valence band than the conduction band[15-17,71]. It will be easier to be approached if the device is tuned from p-type.

With deliberate irradiation of the electron beam, the dosage is able to be systematically tuned gradually from low to high. Electron beams with low energies are scanned on the device in a raster pattern at different acceleration voltages V_a starting from 4 kV to 16 kV. For each scan, the exposure time is fixed and beam current is measured so that the exact dosage can be calculated, listed in table 2. The schematic of the electron beam irradiations (EBI) on devices is demonstrated in Figure 2-24. For acceleration voltage V_a higher than 16 kV, a decrease in device mobility is found, indicating device degradation after high energy beam exposure. Then the acceleration voltage V_a is limited to 16 kV. During electron beam irradiation, all electrodes are grounded. And right after the irradiation, the device is immediately put into the cryogenic system and cooled down to 1.5 K.

2.3.3 Electrical Transport Properties

Figure 2-25 is the resistivity temperature dependence of the same device but with different states after several EBIs. The room temperature resistivities for all the states are almost the same. But at low temperatures, there is a resistivity upturn with an insulating behavior after several electron beam irradiations, indicating the transition from metallic to insulating state. Moreover, the resistivities of all states tend to saturate at the lowest temperature. The pristine state has a residual resistivity of 110 Ω/□ at 1.5K. As the EBI dosage increases, the saturation resistivity and the resistivity upturn temperature increase accordingly. The residual resistivity increases from 110 Ω/□ in pristine state to 860 Ω/□ in the state with the highest dosage, which is almost one order change in magnitude. In the meanwhile, the resistivity in high temperature range has rarely changed, indicating there is no significant additional scattering impurities introduced by EBI which causes the degradation of the device and decrease in the mobility.

There are two possible scenarios for the low temperature insulating states. One is caused by the carrier localization induced by the defects after EBI. But this could also result in the decrease of high temperature resistivity, which is contrary to the experimental data. The other is the carrier density decrease after EBI. Upon irradiation, the hole carriers are decreased and the Fermi level is shifted upwards, leaving the valence band for the bulk bandgap. After a couple of EBIs, the Fermi level gets into the bulk band gap but only ~ k_BT higher than the valence band maxima. In the high temperature range, the thermal excited carriers are mainly responsible for the resistivity. When the temperature is lowered, the excited carriers freeze and then the resistivity increases. It can be inferred that the Fermi level in this device with the pristine state is close to the top of the valence band so that it can easily be tuned into the gap upon EBI. To support this scenario, devices with Hall effect electrodes (2nd geometry in Section 2.3.1, Figure 2-21**b**) are exposed with EBI. For p-type devices, the hole carrier density decreases after EBI. And for n-type device, the electron carrier

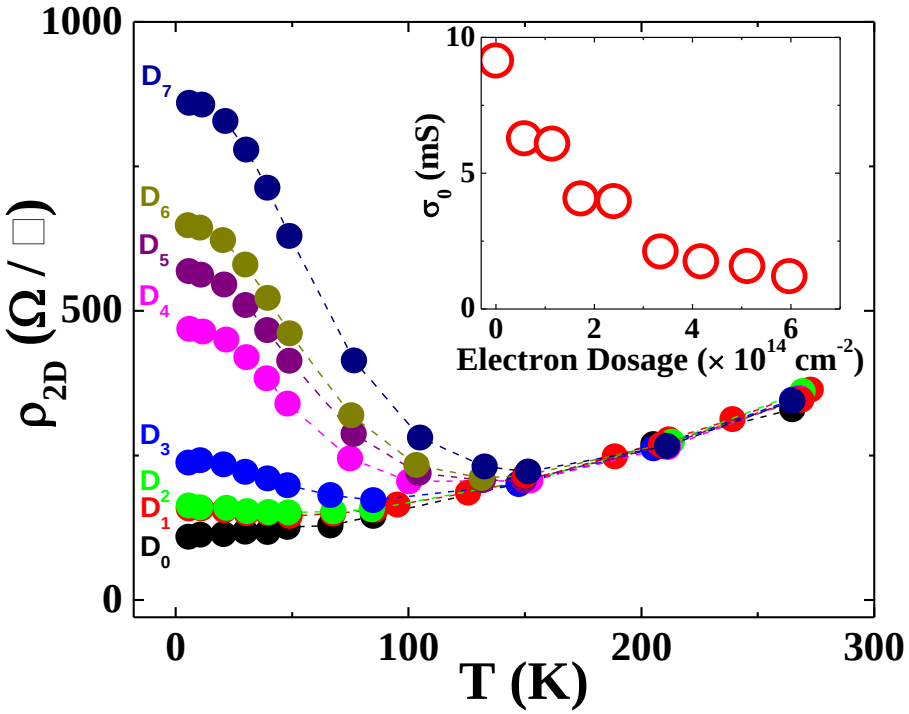

Figure 2-25 Temperature dependence of ρ_{2D} after EBI
D_0 is the prinstine state. From D_1 to D_7, the EBI dosage is increased gradually. Inset is the residual conductivity σ_0 vs. EBI dosage.

density increases after EBI. Both cases confirm the hypothesis that EBI can introduce excess electrons into the system and shift the Fermi level upwards. However, the mechanism of the increase in electron carriers is not clear. One possible scenario could be that the electrons get trapped in the devices. It should be noted that after EBI, if the device is not put into the cryogenic system and cooled to low temperature but stay at room temperature, it will go back to a previous state, becoming less insulating. So the EBI with low energies is a reversible process. However, the evidence is not strong enough to support this scenario. Detailed mechanisms need further studies of this phenomenon.

For each state with different EBI dosages, the conductivity always saturates when the temperature approaches zero, $T \rightarrow 0$. There are two major sources that contribute to the residual

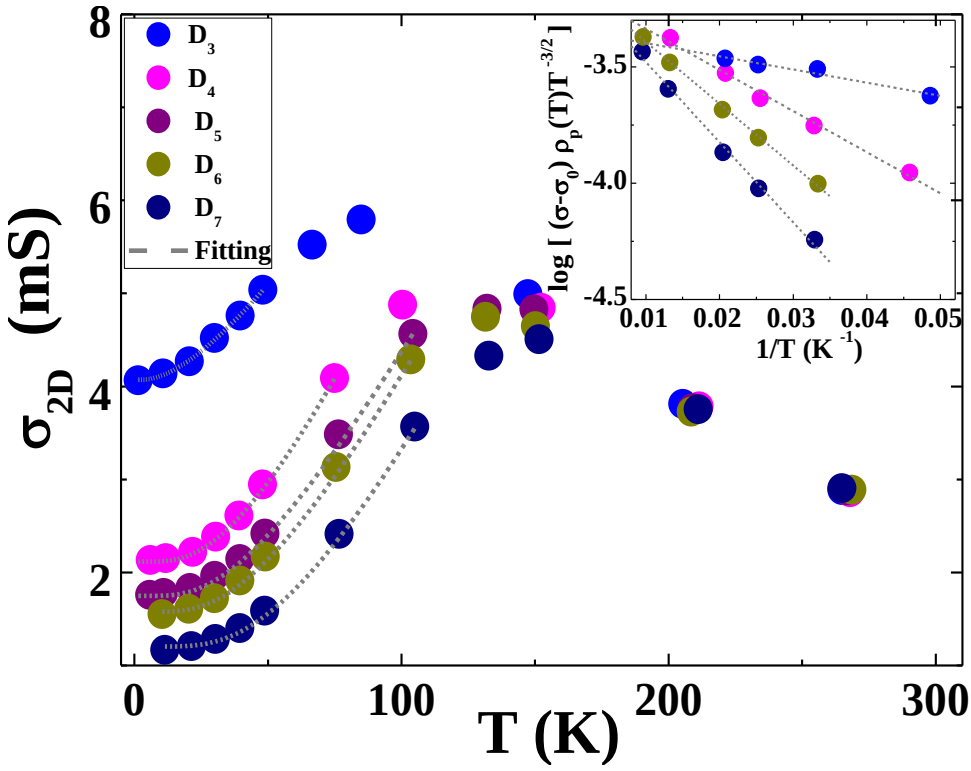

Figure 2-26 Temperature dependence of σ_{2D} after EBI

The σ_{2D} in the states from D_4 to D_7 is plotted. Dashed lines are the best fit to the data in low temperature range. Inset is a plot of $\log\left[(\sigma-\sigma_0)\rho_{d_0}(T)T^{-3/2}\right]$ as a function of *1/T*.

conductivity σ_0. One is from the surface states σ_{ss} and the other is from the impurity states σ_{imp}, $\sigma_0 = \sigma_{ss} + \sigma_{imp}$. In the intermediate temperature range, the situation is complicated. Here, only the low temperature range is discussed. Before the analysis, several assumptions need to be made. First, the hopping conductivity contribution is neglected. Second, σ_{ss} has no temperature dependence. Third, the temperature dependence of the total conductivity is only from the thermal activated bulk carriers excited from the valence band since the Fermi level is only ~ k_BT away from the valence band. Fourth, the conductivities for different states have the same mobility temperature dependence. And Fifth, Bulk states quickly dominate the conductivity as temperature increases. With the assumptions above, the conductivity can be wrote as,

$$\sigma(T) = A\frac{T^{3/2}}{\rho_{d_0}(T)}e^{-(E_F-E_V)/k_BT} + \sigma_0 \ ,$$

where $\rho_{d_0}(T)$ is the resistivity of the pristine state and its change with temperature is mainly due to the mobility change, which is assumed to be the same for all the states. The low temperature conductivity can be fit with this equation. Thus the relative Fermi level position with respect to the valence band maxima can be extracted. In Figure 2-26, the dashed lines are the best fits to the conductivity in different states. The inset is a plot of $\log[(\sigma-\sigma_0)\rho_{d_0}(T)T^{-3/2}]$ as a function of *1/T*, which is expected to show linear lines. The Fermi level positions with respect to the valence band maxima can be calculated from the slopes which are $-(E_F - E_V)/k_BT$. The pristine state of this device is metallic with the Fermi level buried in the valence band. It is impossible to get the relative Fermi level position with this equation. However, once the Fermi level gets into the bulk band gap, the relative Fermi level position can be readily obtained. Table 2 is a list of the EBI dosage, corresponding acceleration voltage, and the relative Fermi level position. The following trend can be found: the higher the EBI dosage, the higher position the Fermi level gets to.

Table 2 List of EBI dosage, Electron Acceleration Energy and relative Fermi level positions

	Electron Beam Irradiation Dosage ($\times 10^{14}$ cm^{-2})	Electron Acceleration Energy V_a (keV)	E_F - E_V (meV)
D_0	-	-	< 0
D_1	0.58	4.0	< 0
D_2	1.14	4.0	< 0
D_3	1.72	6.0	0.89
D_4	3.35	8.0	3.93
D_5	4.17	10.0	4.59
D_6	5.11	9.0	5.67
D_7	5.97	12.0	8.20

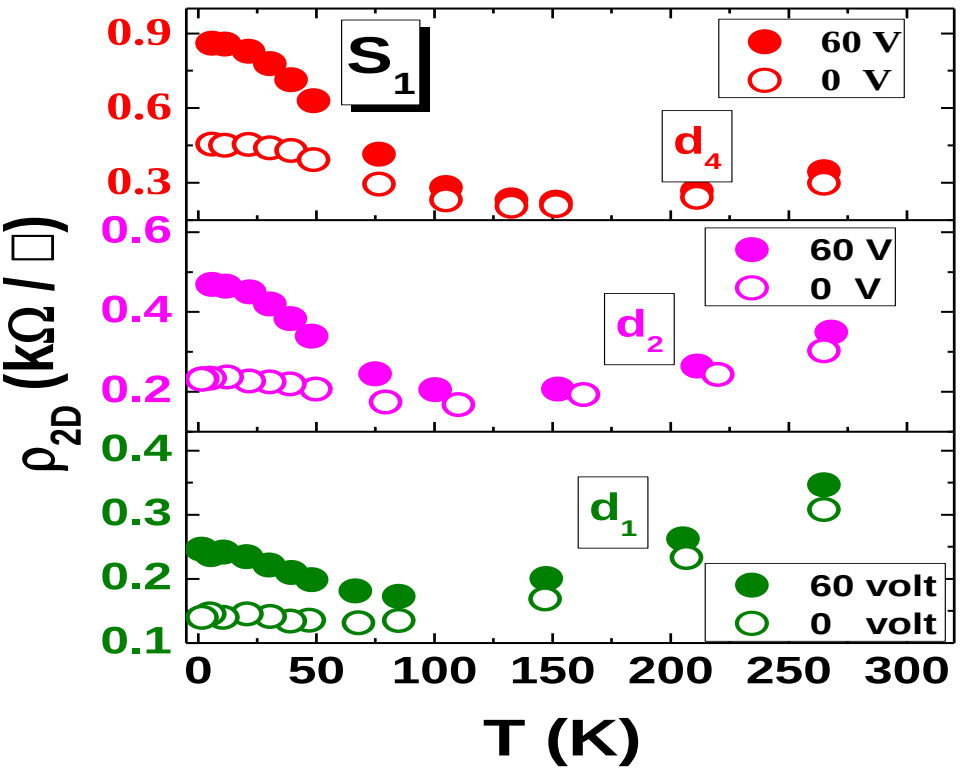

Figure 2-27 Temperature dependence of ρ_{2D} with gate voltages
For each state, the V_g = 0 V and +60 V are applied. The temperature dependence is monitored in three different states, D_1, D_2, and D_4.

With the application of a back gate voltage, the Fermi level can be further tuned. Figure 2-27 is the temperature dependence of ρ_{2D} at 3 different states with no gate and V_g = +60 V. For the states after EBI, the Fermi level is in the bulk band gap, the carrier density from the surface states gets smaller as the Fermi level is shifted upwards by applying positive gate voltage. An increase in ρ_{2D} at low temperature is expected. In Figure 2-27, ρ_{2D} has increased with V_g = +60 V gate voltage, indeed. For all the 3 states, the residual ρ_{2D} at V_g = +60 V increases about twice as that at V_g = 0 V. And it shows a stronger thermal activated behavior with V_g = +60 V gate voltage. For a specific

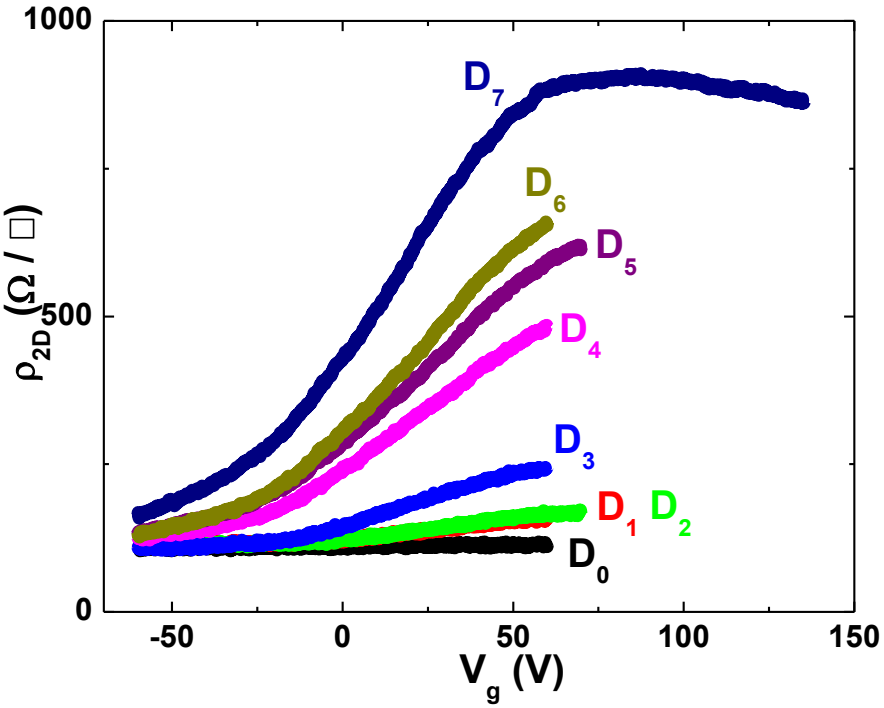

Figure 2-28 Gate dependence of ρ_{2D} after EBI

EBI dosage, the more positive the gate voltage is applied, the bigger the residual ρ_{2D} gets, and the stronger thermal activated behavior the state has. For a specific gate voltage, with higher EBI dosage, the residual ρ_{2D} is bigger and the thermal activated behavior is stronger. This can lead to a conclusion that both EBI and gate voltage have the same effect on the device, that is depleting the hole carriers and upshifting the Fermi level towards the Dirac point. The increase in residual ρ_{2D} is mainly due to the decrease in the carrier density from the surface states. It further confirms that the EBI (with V_a < 16 keV) only decreases the carrier density without affect the device's quality (mobility).

At T = 1.5 K, the gate dependence is measured in the device with different states after each EBI, as is shown in Figure 2-28. In the pristine metallic state, the change in ρ_{2D} from V_g = -60 V to +60 V is tiny compared to the other states. As the EBI dosage increases, the gate modulation gets

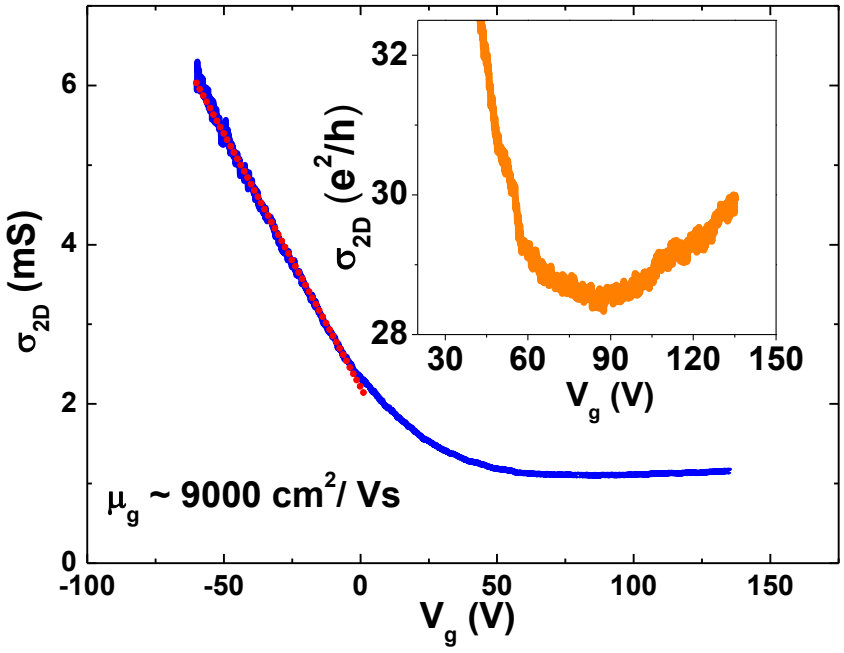

Figure 2-29 Gate dependence of σ_{2D} in the d_7 state
Red line in the curve is a linear fit to the part that is away from the Dirac point. Inset is the zoom-in plot of the gate dependence from 30 V to 135 V.

stronger and stronger. Since the Fermi level is already in the gap after a couple of EBIs, state with higher EBI dosage has a Fermi level closer to the Dirac point which has a stronger gate modulation. The largest change in ρ_{2D} is from the most insulating state, which is from 165 Ω/□ to 910 Ω/□ within a 120V gate voltage range (from -60V to 60V). It shows a ρ_{2D} maxima around V_g = 80 V, indicating the position of the Dirac point. To further study this state, the 2D conductivity σ_{2D} as a function of V_g is plotted in Figure 2-29. The inset is a zoom-in plot of the minimum part in σ_{2D}. The minimum value for σ_{2D} is ~ 28.5 (e^2/h). It should be pointed out that the minimum conductivity comes from the surface states including both the top and bottom surfaces. Obviously, it is still much higher than the quantum conductance[39,72] e^2/h. It can be attributed to the contribution from the extended impurity states.

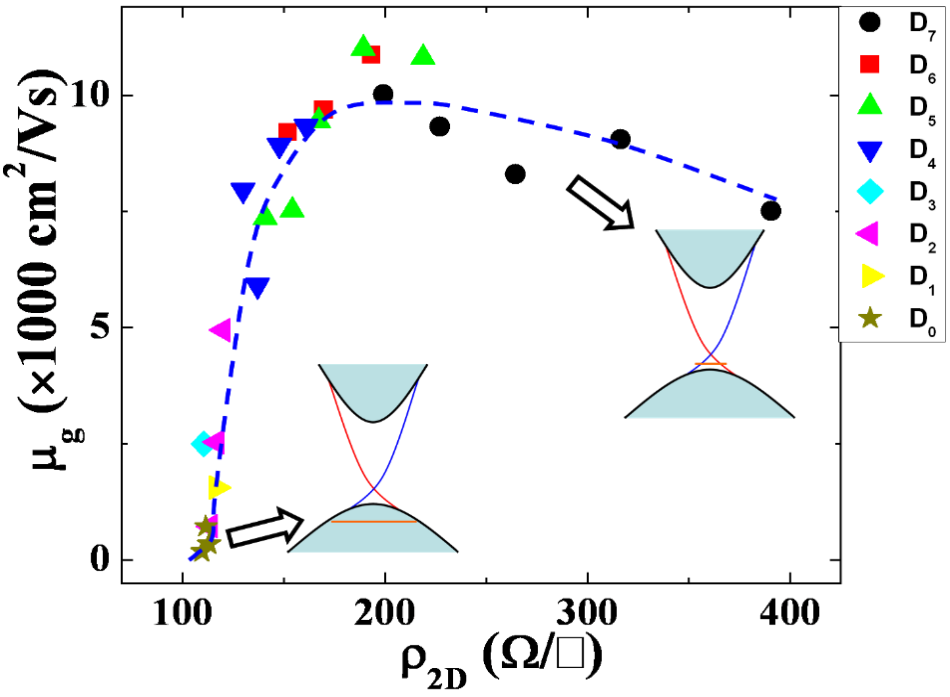

Figure 2-30 Field-effect mobilities after EBI
The mobilities extracted from different regions of the resistivity gate dependence (away from Dirac point) in different states are plotted as a function of ρ_{2D}. The insets are cartoons showing the Fermi level positions related to the corresponding states.

With the gate modulation, the field-effect mobility can be extracted. With the equation of a parallel capacitor which is similar to the back gate setup of the device, $Q_S = C_S \cdot V$, it can be deduced that $e \cdot n_{2D} = C_S \cdot V_g$, where C_S is the effective capacitance per unit area. For the lithography-free devices, the effective capacitance contains the 290-nm-thick SiO_2 and the 50-nm air gap in series. With the dielectric constants for SiO_2 and air, the effective capacitance per unit area can be estimated, which is $C_S = 7 \times 10^{-5}$ F/m^2. From the Drude's model, $\sigma_{2D} = e \cdot \mu \cdot n_{2D}$, one can get $\frac{\sigma_{2D}}{\mu} = C_S \cdot V_g$ or $\sigma_{2D} = \mu C_S \cdot V_g$. Then the field-effect mobility can be extracted from the slope of the σ_{2D} gate dependence. While extracting the slope, a linear fit is made in the region away from the Dirac point. The mobilities for different states with respect to the 2D resistivity is plotted in

Figure 2-30. The insets are cartoons showing the Fermi level positions of the corresponding states. The reason why the region near Dirac point is avoided is that there is always more than one channel of carriers in the vicinity of the Dirac point which is difficult to distinguish one from another. The mobility extracted from the vicinity of the Dirac point has a huge deviation from the actually value.

The field-effect mobility for the pristine state is only 800 $cm^2/V{\cdot}s$. This is a reasonable value for the pristine state and its bulk state carriers since the pristine state is metallic and the bulk carriers dominate the transport property. Upon EBI, the field-effect mobility increases as the dosages increases. It reaches 9000 $cm^2/V{\cdot}s$ in the most insulating d_7 state. Normally, the mobility gets lower when the device becomes more insulating. But the observation is opposite. There must exist high mobility channels in the device, especially when the Fermi level gets into the bulk band gap and the bulk carriers are suppressed. The high mobility channels are attributed to the topological surface states in the device. There are massless Dirac fermions in the surface states of a 3D TI. The topological surface states are protected by the time-reversal symmetry so that the backscattering carriers are greatly suppressed, resulting in a high mobility of the surface state carriers. With this lithography-free technique, the device is much cleaner, free of resist residuals. Moreover, it is suspended from the substrate. Both contribute to the high surface state carrier mobility. It is very reasonable to attribute the high mobility channels to the topological surface states.

2.4 Bi_2Te_2Se Bulk Samples

2.4.1 Electrical Transport Properties

Bi_2Te_2Se single crystals are synthesized in an evacuated quartz tube and heated in a programmable furnace described in Section 2.1.3. Bi_2Te_2Se thin flakes are characterized with FTIR in order to get the flake thickness described in Section 2.2.1. And 5-terminal geometry is employed

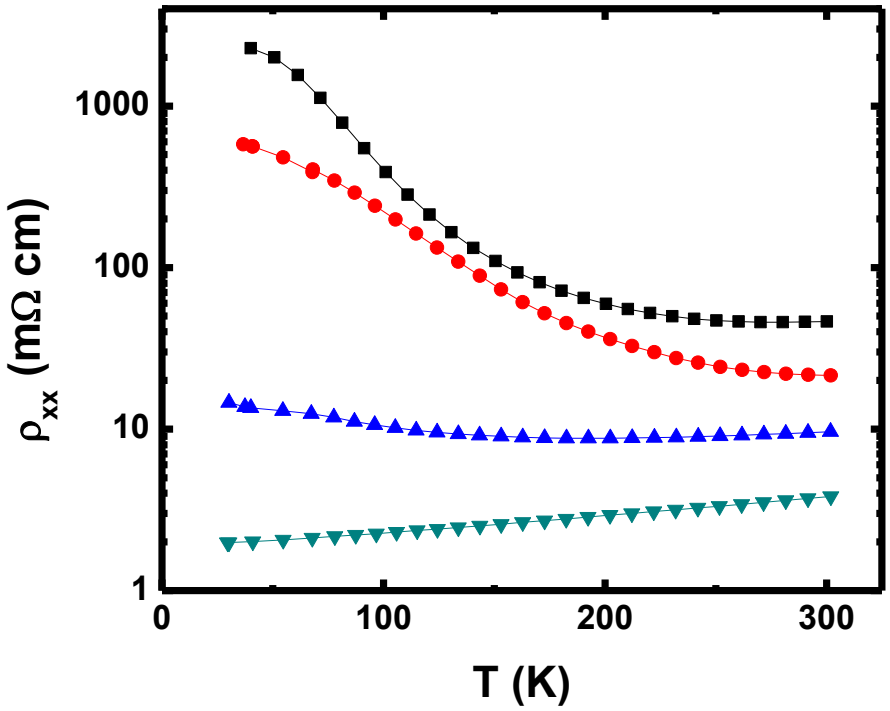

Figure 2-31 Temperature dependence of $\rho_{3D,xx}$ in four Bi_2Te_2Se flakes

for sample electrode's connection. Electrical transport properties are tested in a closed-cycle system with lock-in amplifiers (Stanford Research SR830). The temperature can be varied between 300 K and 20 K. High pulsed magnetic field experiments are done in National High Magnetic Field Laboratory at Los Alamos National Laboratory, New Mexico.

4-terminal resistance R_{4T} and Hall effect are both measured at different temperatures. It is necessary to point out that there is inhomogeneity in the as-grown single crystals as is mentioned previously in $Ca_xBi_{2-x}Se_3$ single crystals. This is somehow unavoidable in the single crystal growth. Even flakes from the same batch have sample-to-sample variations. And within the same crystal, flakes from different regions exhibit fluctuations. But, flakes from the same region always have similar resistivity temperature dependence. The insulating states can be easily found after the test

of several flakes. The 2D resistivity ρ_{2D} can be calculated with R_{4T} and aspect ratio (AR), which is $\rho_{2D} = R_{4T}$ /AR. And the 3D resistivity ρ_{3D} can then be calculated by equation $\rho_{3D} = \rho_{2D} \cdot t$, where t is the flake thickness.

Figure 2-31 is ρ_{3D} temperature dependence of four different Bi_2Te_2Se flakes. In order to see the entire change of both insulating and metallic samples, the y-axis in the figure is plotted in a semi-log style. Different insulating states are observed in the samples, among which the bulk insulating state is achieved. At room temperature, the bulk insulating samples have a much higher ρ_{3D} (~ 45 mΩ·cm) which is more than one order higher in magnitude than that of the metallic state (~ 4 mΩ·cm). When temperature is lowered, weak insulating samples and metallic sample have only slight changes from 300 K to 20 K. But for the insulating samples, ρ_{3D} increases nearly two orders in magnitude and reaches 2 Ω·cm, ~ 45 times bigger than that at room temperature! Compared with the ρ_{3D} at 20 K for the most insulating Ca-doped Bi_2Se_3 bulk flake which is ~ 100 mΩ·cm, it is 20 times larger. This clearly demonstrates that the realization of highly insulating bulk state in the Bi_2Te_2Se flakes and confirms the theory, which predicts the suppression of Se vacancies and Bi-Te antisite defects in this material.

At different temperatures, the Hall effect is recorded for the most insulating samples. Figure 2-32 is a typical temperature dependence of the Hall coefficient in an insulating sample. At room temperature, the Hall coefficient is small and positive, meaning hole carriers with a high density. It increases gradually as the temperature is cooled down, indicating the decrease in the carrier density. At T ~ 110 K, the Hall coefficient reaches maximum and starts to decrease. It then crosses zero at T ~ 60 K and turns to negative at even lower temperatures. This sign change of Hall coefficient indicates that the dominating carriers change from holes to electrons during the cool-down process. In the intermediate temperature range, both holes and electrons exist in the sample. Two different channels of carriers with different mobilities result in a nonlinear curvature in the

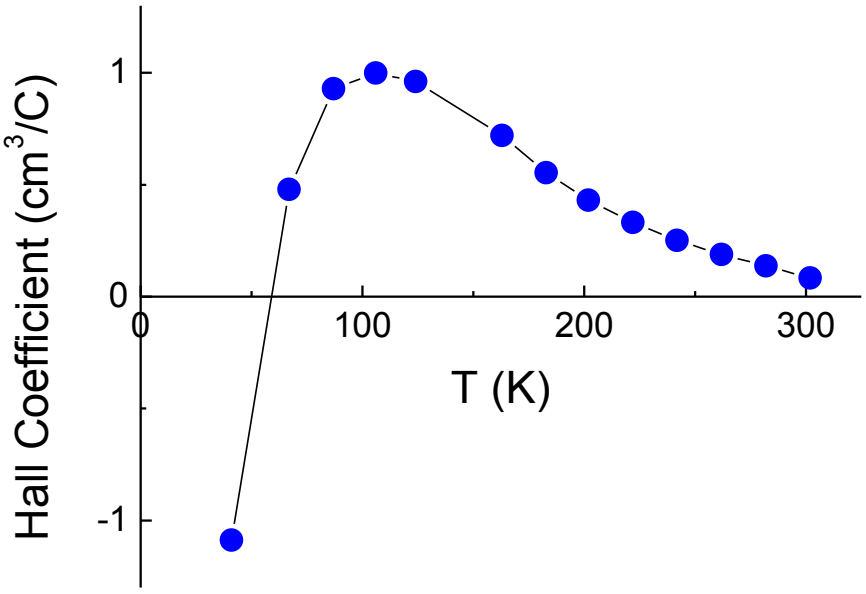

Figure 2-32 Temperature dependence of the Hall coefficient in Bi_2Te_2Se

Hall resistance. This can be clearly seen in Figure 2-33. The Hall resistance at temperatures from 100 K to 10 K shows a clear nonlinear feature. Due to the existence of two channels of carriers, the simple carrier density calculation derived in Section 2.2.2 from the Hall effect measurement is no longer applicable. To extract the carrier densities and mobilites from the two channels, more sophisticated calculation should be used[73]. In the lowest temperature T = 4.3 K, a relatively straight line is obtained for this sample which gives a 3D carrier density $n_{3D} \sim 6.9\times10^{17}$ cm^{-3}. This is comparable with the carrier density of the most insulating Ca-doped Bi_2Se_3 flakes, showing the success of the decrease of carrier density in Bi_2Te_2Se samples.

For samples with bulk insulating states and low carrier density, the signal from the topological surface states takes a larger fraction of the overall transport signal, which is more likely to show

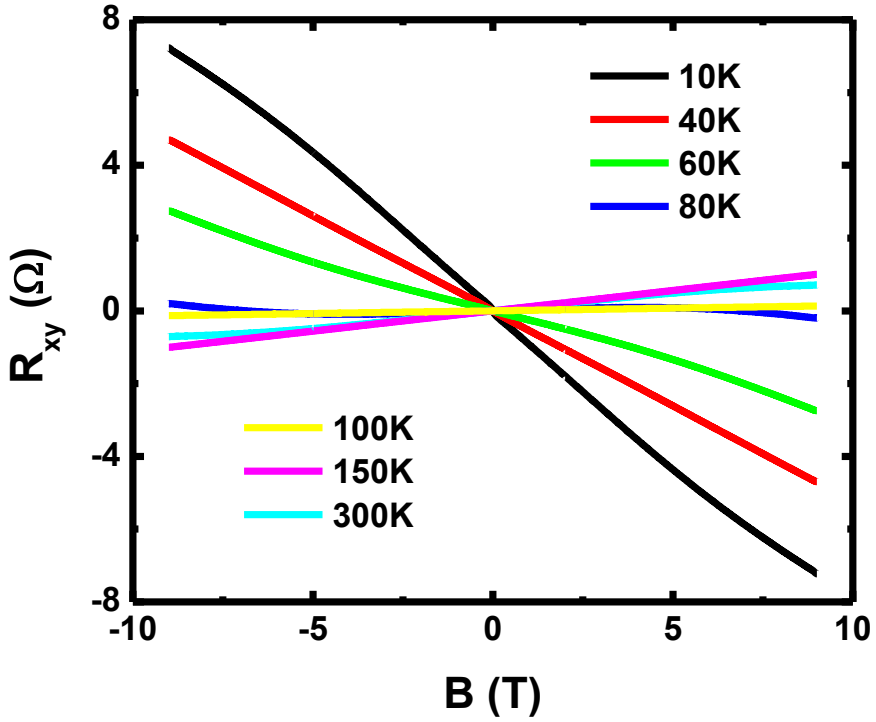

Figure 2-33 Hall effect of Bi_2Te_2Se at different temperatures

the properties of surface states. Compared to bulk states, surface states have massless Fermions with a linear energy dispersion with the respect to momentum ***k***. And they are protected by the time-reversal symmetry due to the strong spin-orbit coupling. The backscattering is believed to be greatly suppressed. Subsequently, it leads to a high mobility in the surface states, while the mobility is relatively low in the bulk channels. One technique that can track the high mobility channels is the Shubnikov-de Haas effect measurement. At low temperature and high magnetic field, high mobility carriers are more likely to show an oscillating behavior in resistance due to the split of the Landau levels. As is discussed in Section 2.2.3, the oscillations are periodic with the change in magnetic field. The periodicity in magnetic field should be 1/B is inversely proportional to the channel's carrier density. In order to study the surface states of 3D topological insulators, high field

is needed since the carrier density in 3D topological insulator's surface states is relatively low ~ 10^{12} cm^{-2}.

2.4.2 High Pulsed Magnetic Field Measurements

The SdH effect of Bi_2Te_2Se flakes is studied in a high pulsed magnetic field up to 65 T at the National High Magnetic Field Laboratory at Los Alamos National Laboratory, New Mexico. Figure 2-34 is the schematic diagram of the electric circuit of the measurement. The AC voltage source V_S is applied through a transformer to ensure the entire circuit connected to the sample is discretely floating without connection with any other noise sources. If DC measurement is needed, a battery can be used to take the place of the AC source and the transformer. After transformer, the source voltage is changed to V_S' and the real voltage applied on the sample is V_S'', as is shown in Figure 2-34. Before sample, a voltage dividing resistor R is added to the circuit in order to protect the sample. Another small resistor R_I is added after sample and a voltmeter V_I is used to measure the voltage drop across R_I. Then the current flowing in the circuit can be instantly calculated, $I = V_I/R_I$. To ensure good contacts, indium dots are employed to connect sample to gold wires which are soldered to the sample carrier. In order to suppress the vibrating noise from the gold wires, they are cut as short as possible with the consideration of thermal contraction at low temperature. On the sample carrier, the gold wire is soldered to the pins. And then the electrodes connected to the sample carrier socket coming out from the cryogenic system must be twisted in pairs: two source electrodes, two 4-terminal longitudinal resistance electrodes, and two Hall effect electrodes.

Before the release of the pulsed magnetic field, a series of capacitors needs to be charged according to the desired magnetic field. Then the charges are released within a very short time period (typically a few milliseconds), high magnetic field is then reached. If the change in

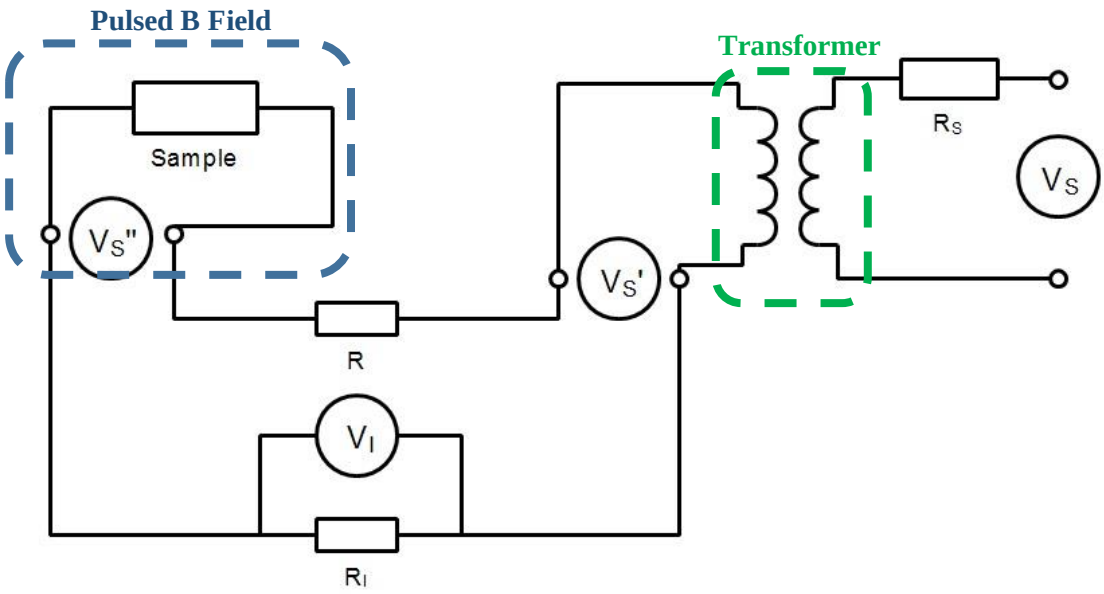

Figure 2-34 Schematic diagram of the electric circuit in high pulsed magnetic field
Green dashed area is a transformer box that transforms the source into the discrete circuit. A battery can be used when DC is needed. Blue dashed area is on the sample holder which is in the perpendicular pulsed magnetic field.

magnitude of the magnetic field is monitored, there will be a sharp increase in the magnetic field at first (rising field). And then the field reaches maximum which should be around the desired value, followed by a decrease in the field (falling field) with a relatively slower rate than that of the rising field. A negative magnetic field can be realized by negatively charging the capacitors. During the release of the magnetic field, a digitizer is employed to record signals and signal changes in the sample in an extraordinarily fast fashion. The recorded data is then processed with a technique which is similar to the data process in a lock-in amplifier.

Figure 2-35 is the magnetoresistance of a high resistivity sample in a perpendicular pulsed magnetic field at 1.55 K. The field range is from 3 T to 56 T. For the field close to 0 T, there is a clear low field cusp in the MR curve indicating the weak antilocalization in the sample which is due to the strong spin-orbit coupling and is a characteristic feature of a topological insulator. In the

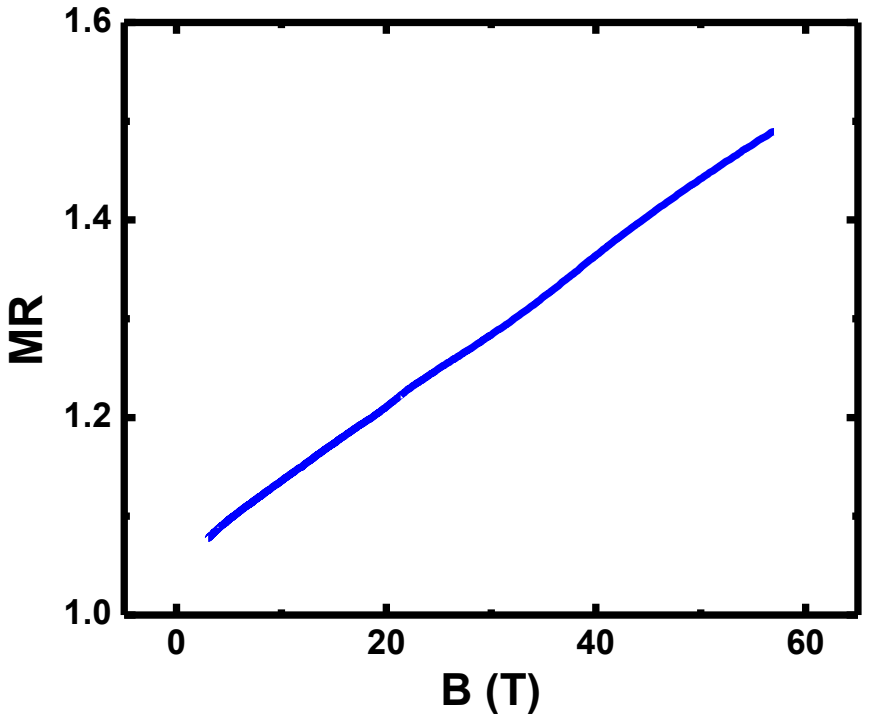

Figure 2-35 MR of Bi_2Te_2Se in high magnetic field

high field range, clear oscillations can be seen in the MR curve, even without subtracting the non-oscillating MR background. Figure 2-36 is the MR residual after the removal of a 2-order polynomial background, which shows the SdH oscillations. It is plotted as a function of the inverse of the magnetic field, *1/B*. More than two periods of the oscillations are observed. By using equations deduced in Section 2.2.3, the SdH carrier density, n_{SdH} can be revealed, $n_{SdH} = 2.87 \times 10^{12}$ cm^{-2}, which is a typical density for the topological surface state, as is discussed in Section 2.2.3.

For the most insulating bulk samples, the resistance is relatively high at low temperatures, for instance 1.5 K. And the resistance is even higher for the Bi_2Te_2Se nanodevices. The pulsed magnetic field is released only within a few milliseconds. The heating problem will become serious in samples with high resistance, which can lead to an inaccuracy in the measurement. Moreover,

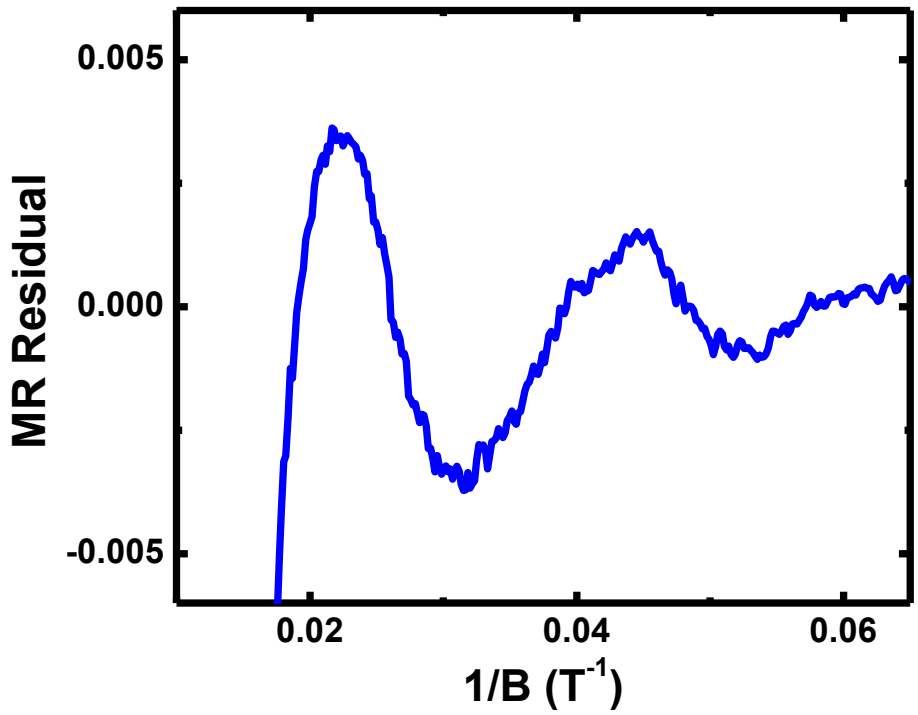

Figure 2-36 SdH oscillations in Bi_2Te_2Se

the connecting wires between the sample and sample holder are very likely to move during the release of the pulsed field, which could increase the noise level in the detected signals. This is why the connecting gold wires are pressed firmly to the sample with indium dots and are soldered to the sample holder with as short length as possible. Another reason of pressing the wires firmly to the sample is to reduce the contact resistance which is another major source of the heating problems. Here, only the data from the falling field is shown (Figure 2-35 and Figure 2-36), since the data from rising field and falling field are almost the same, the difference is less than 1%, which means the heating problem is not serious in the Bi2Te2Se bulk sample, even with high resistive states. Moreover, the data from both rising and falling fields are smooth, indicating a relatively low noise in Bi_2Te_2Se bulk samples.

For Bi_2Te_2Se nanodevices, the resistance and contact resistance are both very high since the device is very thin, the scaled resistance will be much higher than that of bulk samples. Although there will be extra electrons introduced in the device during fabrication process, which leads to lower resistivity than that of the bulk samples, yet the device is thinned to more than 1000 times thinner than the bulk sample. So the resistance is usually much higher than the bulk samples. Moreover, the deposited metal electrodes always have a contact resistance bigger than 1 kΩ due to the resist residual or surface oxidation during the fabrication process. The overall resistance is usually close to or more than 10 kΩ for devices while it is only 400 Ω for the most insulating bulk sample. Moreover, it has to use a wire bonder to connect the device to the pins on the sample carrier. The wires are thin, long and unstable, which could lead to a high noise level. The curves obtained from the measurement of Bi_2Te_2Se nanodevices are not smooth, meaning a relatively high noise level. And the heating problem is very serious in the devices, as indicated by a hysteresis loop between the data from the rising field and the falling field. Due to this heating problem, it is not easy to obtain useful signals Bi_2Te_2Se nanodevices.

2.5 Bi_2Te_2Se Nanodevices

Bi_2Te_2Se nanodevices are fabricated from flakes exfoliated from high resistivity bulk samples with a standard electron beam lithography method first. Figure 2-37 is a typical SEM image of the device with angle position for the contact electrodes. On the end of each electrode, two clear steps can be observed, which is due to the two angle depositions.

Figure 2-38 is a typical resistivity temperature dependence of a Bi_2Te_2Se devices. The resistivity has very weak temperature dependence. The relative change from room temperature to 1.5 K is very small. It shows a metallic behavior in the high temperature range (ρ_{2D} decreases as T

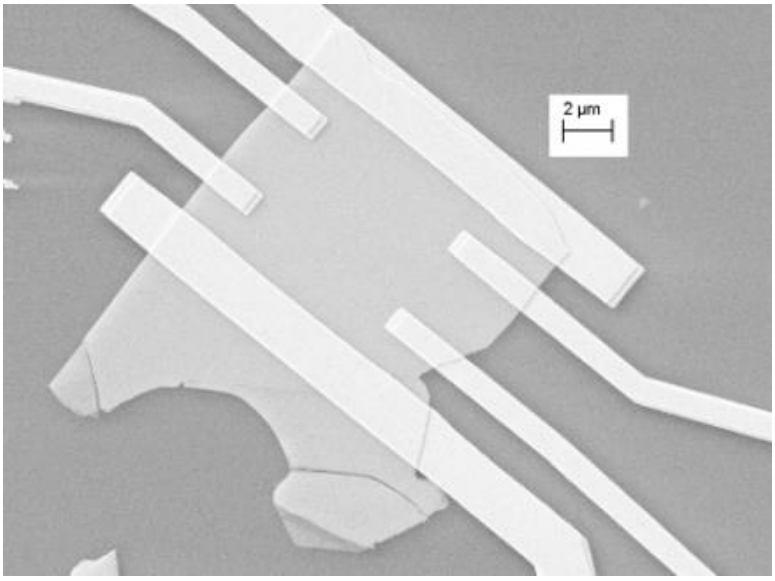

Figure 2-37 SEM Image of a Bi_2Te_2Se device

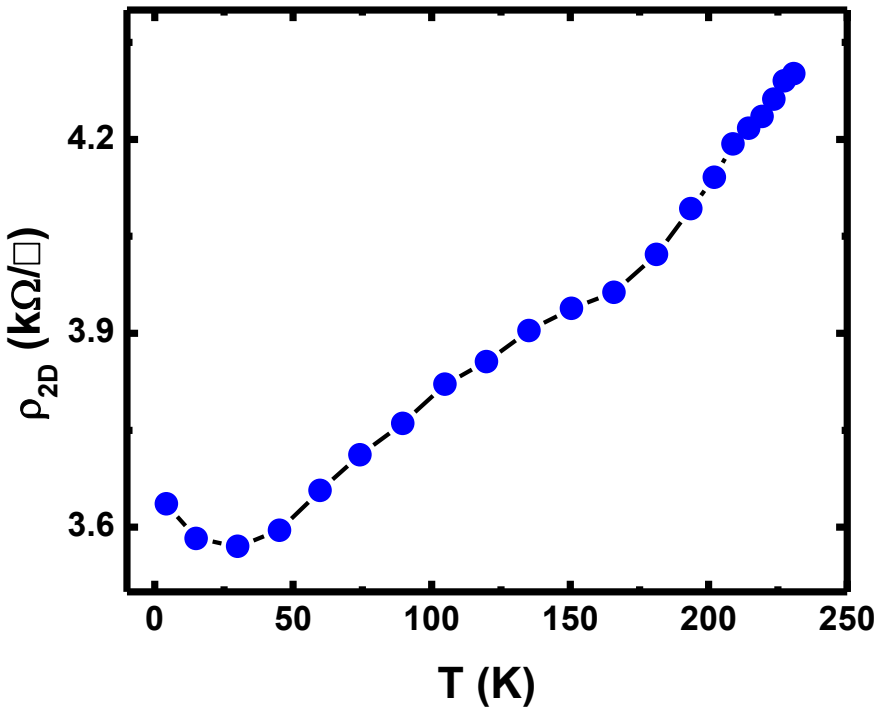

Figure 2-38 Temperature dependence of ρ_{2D} in a Bi_2Te_2Se device

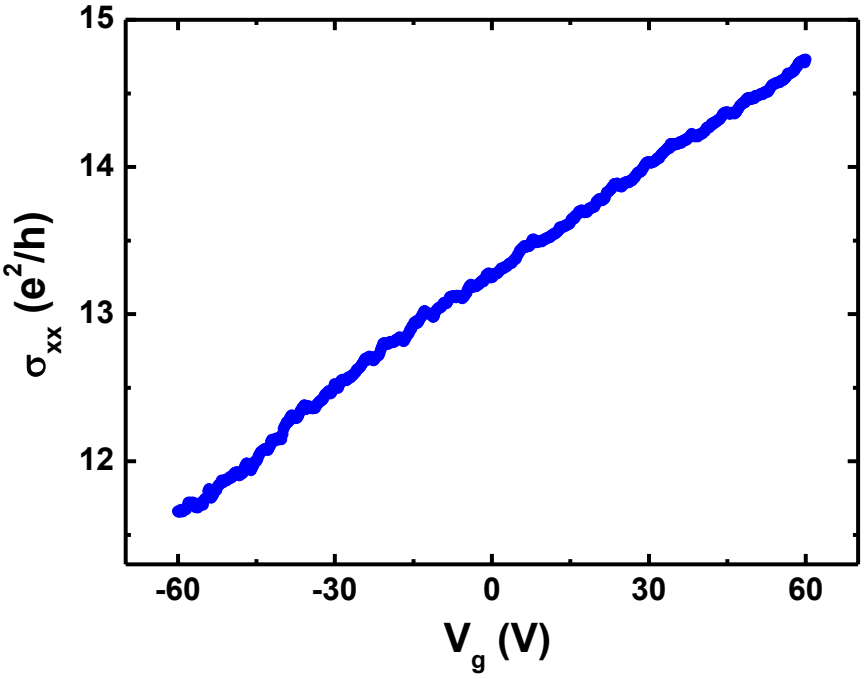

Figure 2-39 Gate dependence of σ_{xx} in a Bi_2Te_2Se device

decreases). But there is an upturn emerging in the low temperature range. Figure 2-39 is the gate dependence of this device. And for most devices studied, the gate dependence is similar to this one. The gate modulation of the conductance is small, indicating that the total carrier density in the nanodevice is still high.

Figure 2-40 is the Hall effect measurement. The perpendicular magnetic field is applied from -8T to 8T. The red line is a linear fit to the Hall effect data. It fits very well to the original data, indicating a linear relationship between the Hall resistance and magnetic field, even in the high magnetic field range. This linear relationship suggests that there is only one majority channel in the device. The 2D carrier density calculated from Hall effect is ~ 6.5×10^{13} cm^{-2}, which is very high if compared to the SdH carrier density discussed in the previous section. So it can be attributed to

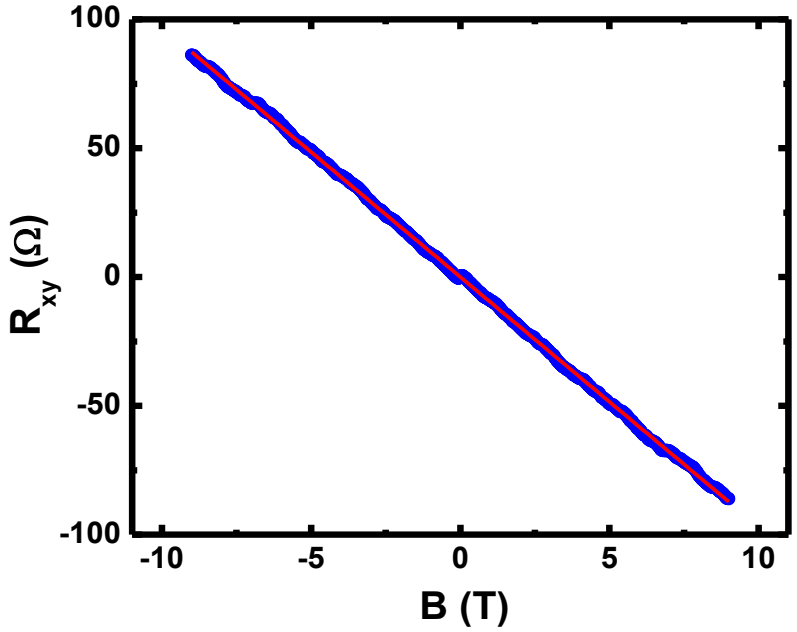

Figure 2-40 Hall effect in a Bi_2Te_2Se device

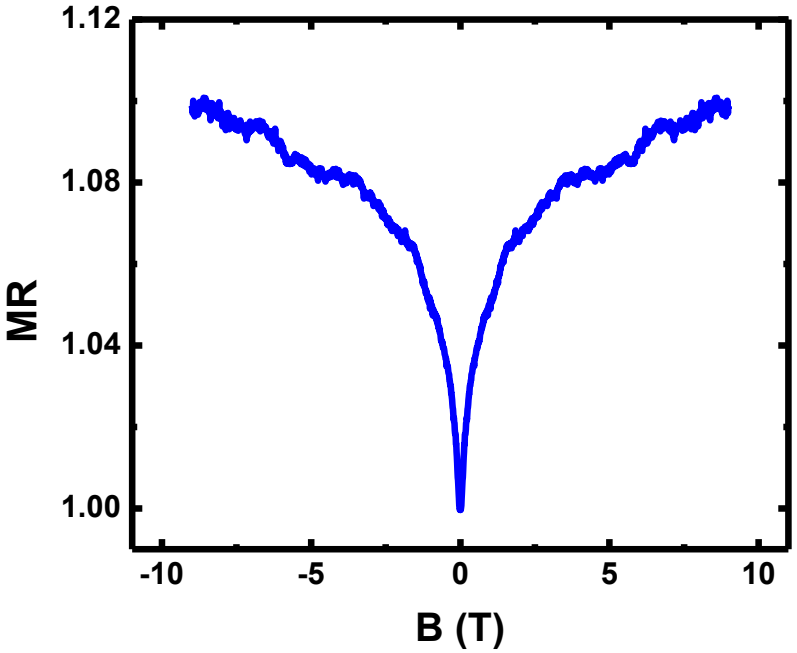

Figure 2-41 MR in a Bi_2Te_2Se device

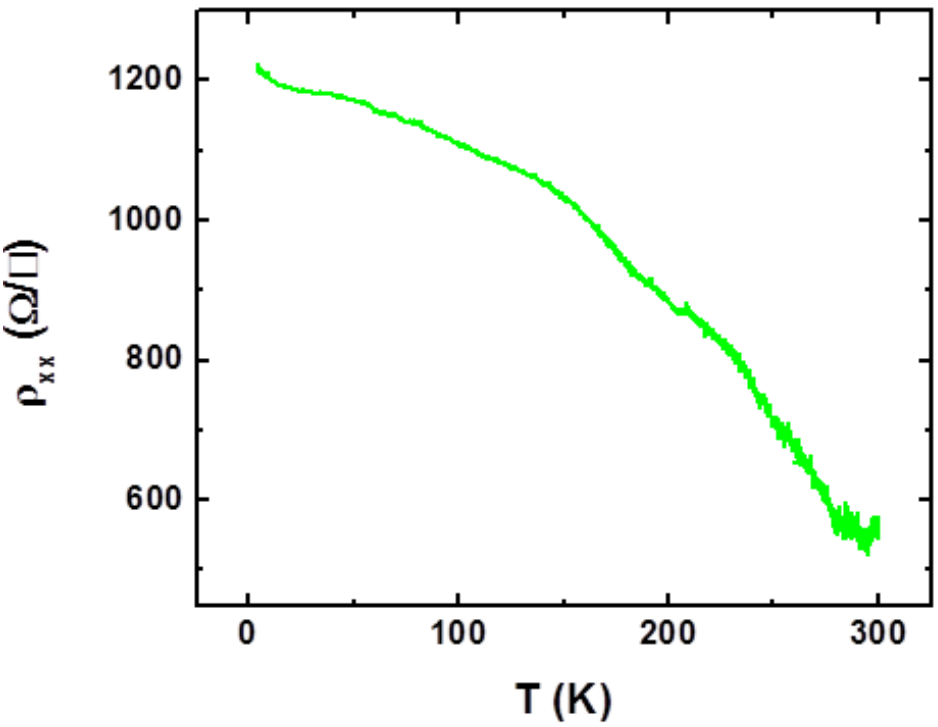

Figure 2-42 Temperature dependence of ρ_{xx} in a lithography-free device

the bulk carriers. This high carrier density smears out the topological surface states in the device so that the two-band Hall effect cannot be observed and only a linear line is obtained in the Hall effect measurement.

The magnetoresistance is recorded at the same time when Hall effect measurement is performed, as is shown in Figure 2-41. In the magnetoresistance curve, there is always a sharp low field cusp, indicating the weak antilocalization effect which is due to the strong spin-orbit coupling in the device, an indicative feature of the topological insulators.

Devices fabricated in the normal approach seem to have high carrier density, which can be confirmed from the Hall effect and gate dependence measurements. High carrier density always

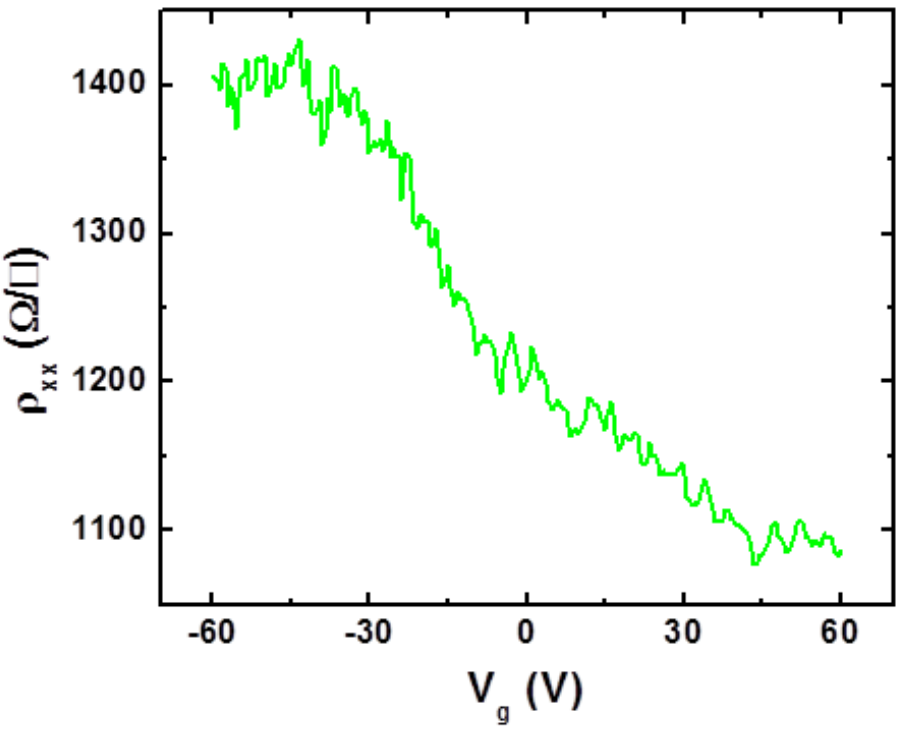

Figure 2-43 Gate dependence of ρ_{xx} in a lithography-free device

comes with metallic temperature behaviors and weak gate modulations. To reduce the high bulk carrier density, the lithography-free technique is again employed. Figure 2-42 is the resistivity temperature dependence of a device on the four-parallel electrodes. Although the ρ_{xx} is not big, it shows an insulating temperature behavior. The relative change in ρ_{xx} from 300 K to 4.3 K is much higher than that in the devices fabricated with normal lithography. Moreover, the gate modulation is bigger than that in most of the lithography-fabricated devices, as is shown in Figure 2-43. However, the strong gate dependence of ρ_{xx} is not able to be realized in devices fabricated with lithography-free technique. One possibility should be the air doping after device fabrication, as is mention in previous sections. Unfortunately, since the device is fabricated on a set of four-parallel electrodes, Hall effect cannot be performed. The carrier density remains unknown for this device.

Another difficulty in Bi_2Te_2Se is the control of the carrier type in the starting bulk samples. Different from the Ca-doped Bi_2Se_3 which can be systematically tuned with different Ca doping levels, slight change in composition of Bi_2Te_2Se can hardly lead to a p-type sample which is an essential condition for the lithography-free technique and thus further tuning of the Fermi level with electron beam irradiation.

Further effort is made to reduce the influence of the environment. Immediately after device fabrication (nanoflake exfoliation on the pre-patterned electrodes), a protection layer of PMMA is made right on top of the device area in a N_2-filled glovebox. However, several devices fabricated with this method behave quite similar to the device with the protection PMMA layer. No improvement is found in the device's resistivity, the corresponding temperature dependence, the Hall effect, and the gate dependence. One possible reason could be the interaction between the PMMA resist and the device surface. Or the prepatterned electrodes are already contaminated by the air. After device exfoliation, device is then contaminated by the electrodes. Another possibility could be the inefficiency of the protection PMMA layer. It might be porous and cannot prevent the device from being contact with air (oxygen, water molecule) Another attempt is to fabricate device with normal lithography method first, and then clean and etch device surface with Argon ions in a sputtering system and follows the deposition of a protection layer (MgO). But from the carrier density calculated from the Hall effect measurement, the carrier density increases after Ar ion milling. Possible reasons could be the doping of Ar ions or the protection layer (MgO) molecules into the device.

Similar to Ca-doped Bi_2Se_3 nanodevices, in order to achieve high insulating state and gate modulation, starting p-type bulk materials and carrier density control in the bulk materials are essential. A systematic study of the relationship between the carrier type/density and the

composition of Bi_2Te_2Se should be conducted so that the systematically tuning of Fermi level in Bi_2Te_2Se can be realized.

2.6 Discussion

In this chapter, the Bi_2Se_3 and Bi_2Te_2Se single crystals are successfully synthesized. The single crystals are firstly characterized with XRD. The narrow full-width-at-half-maximum of sharp peaks obtained in the XRD pattern demonstrates that the materials are with large grain size and of high quality. μm-thick flakes are exfoliated from Bi_2Se_3 and Bi_2Te_2Se single crystals and then characterized with FTIR spectroscopy, from which flake thickness and the relative Fermi level position are revealed.

Then indium dots and gold wires are connected to the flakes with either Van der Pauw geometry for small or irregular samples or 5-terminal geometry for big samples. Resistivity and Hall effect measurement are carried out afterward. Ca is added to Bi_2Se_3 during the single crystal growth in order to generate holes to compensate for excess electrons introduced by Se vacancies. And the bulk insulating states are achieved in Ca-doped Bi_2Se_3. For Bi_2Te_2Se, the material itself has a property to suppress Se vacancies and Bi-Te antisite defects, which are major defect sources in Bi_2Se_3 and Bi_2Te_3, respectively. So the insulating behavior is also expected in Bi_2Te_2Se. Indeed, from the resistivity temperature dependence, the bulk insulating states are successfully achieved in Bi_2Te_2Se flakes. 3D resistivity as high as 0.1 Ω·cm is observed in the most insulating Ca-doped Bi_2Se_3 sample and 2 Ω·cm in the most insulating Bi_2Te_2Se sample. This is also further confirmed by the Hall effect measurement. In the most insulating samples, 3D carrier density is also the lowest, in the order of 10^{17} cm^{-3}.

With the 3D carrier density and the relative Fermi level position in Ca-doped Bi_2Se_3, the bulk bandgap E_g and the reduced effective mass μ^* are extracted, E_g = 0.093 eV and μ^* = 0.072 m_e, which are consistent with previously reported results by other groups. However, the same analysis could not be performed on Bi_2Te_2Se. Different from Ca-doped Bi_2Se_3 in which Ca concentration can be adjusted, the carrier density is difficult to manipulate. Moreover, the band structure near the Dirac point in Bi_2Te_2Se is more complicated than Bi_2Se_3. Its Dirac point is buried in the valence band. The bulk density of states are very high in the valence band, close to Dirac point. The bulk bandgap and carrier effective mass cannot be extracted in the same way as in Bi_2Se_3.

Shubnikov-de Haas effect are both measured and clearly observed in both Bi_2Se_3 and Bi_2Te_2Se bulk samples. In the undoped Bi_2Se_3, the SdH carrier density $n_{2D,SdH} = 2.4\times10^{12}$ cm^{-2}. Since the bulk has a relatively low mobility, this SdH oscillation should be separated from the bulk carriers. Then it has to be from the surface stare carriers. And this density can be attributed to the surface state carrier density. . With the temperature dependence of the SdH oscillations, the electron effective mass and Dingle temperature are obtained, m^* = 0.142 m_e and T_D = 35K which corresponds to τ_D = 2.2×10^{-13} s. In Bi_2Te_2Se, a similar density is obtained, $n_{2D,SdH} = 2.87\times10^{12}$ cm^{-2}.

Bi_2Se_3 nanodevices are then fabricated from the optimally doped (insulating) Bi_2Se_3 bulk samples. Normal electron beam lithography approach is then found always increasing the electron density in the device. Moreover, exposure to the atmosphere is another factor that increases the electron density. To overcome the negative effect of the electron beam lithography, a generic lithography-free technique is developed for device fabrication. Further, the negative effect of electron beam lithography, that is the increase in electron density upon electron beam exposure, can be intentionally used to compensate for the holes in p-type devices. Then the overdoped p-type starting bulk samples are employed for the device fabrication with the lithography-free technique. The excess hole carriers in the p-type sample will be compensated by the electrons unavoidably

introduced during the preparation process (for example, exposure to air) and the electrons from the electron beam irradiation, which can be systematically controlled and tuned.

With the application of electron beam irradiation and electrostatic gating, the Fermi level in the lithography-free fabricated device is tuned into the bulk bandgap. Insulating temperature behaviors are observed in the device after several EBIs. After analyzing the temperature dependence curve, the Fermi level positions with respect to the top of the valence band are calculated in the states after each EBI. A maximum in the resistivity gate dependence, an indicative sign of the Dirac point, is found. The field-effect mobility extracted from the gate dependence increases from 800 $cm^2/V{\cdot}s$ in the pristine metallic state to 9000 $cm^2/V{\cdot}s$ in the most insulating state, which represents the mobilities for the bulk channels and topological surface state channels, respectively.

For Bi_2Te_2Se devices, the strong gate modulation cannot be achieved although the insulating state is observed. The employment of the lithography-free technique could improve the device performance. However, the improvement is limited. Various efforts are made to avoid problems in the fabrication process or exposure to air. The expectations are not met. One major problem could be the difficulty in obtaining high p-type starting materials. Without this condition, the lithography process and other factors could easily change the device to a heavily n-type doped material. Further control of the Fermi level through gating or EBI becomes difficult or even impossible. A systematic study of the relationship between the material composition and the corresponding carrier type needs to be carried out. There is another problem with Bi_2Te_2Se. The band structure near the Dirac point is complex, which can be referred to Figure 2-2. The Dirac point is almost buried in the valence band. The high density of states in the valence band makes it difficult to detect the position of the Dirac point. It also makes it difficult to use the EBI to tune the Fermi level from the valence band. More studies on the Bi_2Te_2Se needs to be done in the future.

Chapter 3 Graphene and Transition Metal Dichalcogenides

In the first part of this chapter, it is focused on the study of the ferromagnetism induced in graphene devices. People use the proximity effect to induce order parameters within a certain characteristic length scale, such as the proximity-induced superconductivity, ferromagnetism and ferroelectricity. Due to carbon's weak spin-orbit coupling, graphene has a relatively long spin relaxation time and diffusion length, which are properties of an ideal spintronics material. But people always need to inject spin to graphene using ferromagnetic sources. To introduce spin degree of freedom, people have proposed ideas such as putting on adatoms[43], creating vacancies[42], introducing sp^3 bonds[74], edge states in nanoribbons[41], etc. Because of the single layer nature of graphene, it provides us an unprecedented opportunity to control the band structures with the proximity effect. In this chapter, we describe a distinctive approach which combines the best graphene with the best magnetic materials together so as to deliver unique properties without doping or introducing any defects.

The second part is a preliminary study on the properties of transition metal dichalcogenides (TMDs). As discussed in Chapter 1, single-layer TMDs has many distinctive properties, such as the inversion symmetry breaking and the subsequent spin splitting, the valence band splitting, the spin and valley coupling, etc. With the control of the Fermi level, the valley Hall effect can be realized in single-layer TMDs. In the valley Hall effect, which is analogous to spin Hall effect, when a longitudinal electric field is applied, electrons in different valleys experience opposing effective magnetic fields and will be deflected to different transverse edges in TMDs. It opens up a new opportunity for the study of valleytronics materials. Moreover, with the manipulation of its band structure, for example the magnetic proximity effect in TMDs, more interesting phenomena will emerge. We explored different dielectric materials to manipulate the Fermi level in TMDs and therefore to realize the valley Hall effect.

3.1 Graphene on Insulating Magnetic Thin Films

3.1.1 Quantized Anomalous Hall Effect

To discuss about the quantized anomalous Hall effect (QAHE), one has to know the anomalous Hall effect (AHE) first. And to know the AHE, one needs to know why it is anomalous and what ordinary Hall effect is. For the ordinary Hall effect, when a conductor is subjected to a perpendicular magnetic field, with a longitudinal current applied, the moving carriers (electrons and holes) will experience the Lorentz force in the perpendicular magnetic field, which is $\vec{F} = q\vec{v} \times \vec{B}$, where q is the charge of the electron or hole, $\vec{v}$ is the velocity that the electron or hole travels within the conductor, and $\vec{B}$ is the magnetic field. The carriers will be deflected transversely to the edges and a voltage difference will build up between the two transverse edges. However, the Hall signal is different in ferromagnetic materials. There is an anomalous part in addition to the ordinary Hall signal (usually much larger than the ordinary Hall signal), which cannot be explained with the ordinary Hall contribution from the internal magnetization. This is called the anomalous Hall effect, which is found to be related to the spin-orbit coupling and broken time-reversal symmetry in ferromagnetic materials. The QAHE is a quantized version of the AHE. In QAHE, the AHE conductivity becomes quantized in certain materials, under certain conditions, which will be discussed in next paragraphs.

In 2013, the QAHE is realized in a 3D topological insulator Cr-doped $(Bi_xSb_{1-x})Te_3$ at temperatures[26] below 30 mK. Although the topological insulator is fundamentally different from graphene, they share many superior properties, such as linear energy dispersion or the massless Dirac Fermions, high surface carrier mobility, etc. Moreover, it is known that a non-magnetic thin film is expected to exhibit magnetic behaviors when it gets very close to magnetic material, which is known as the magnetic proximity effect[30,31,75-77]. Furthermore, for atomically thin layers, for example graphene, this effect should be even stronger and readily to be detected in the electrical

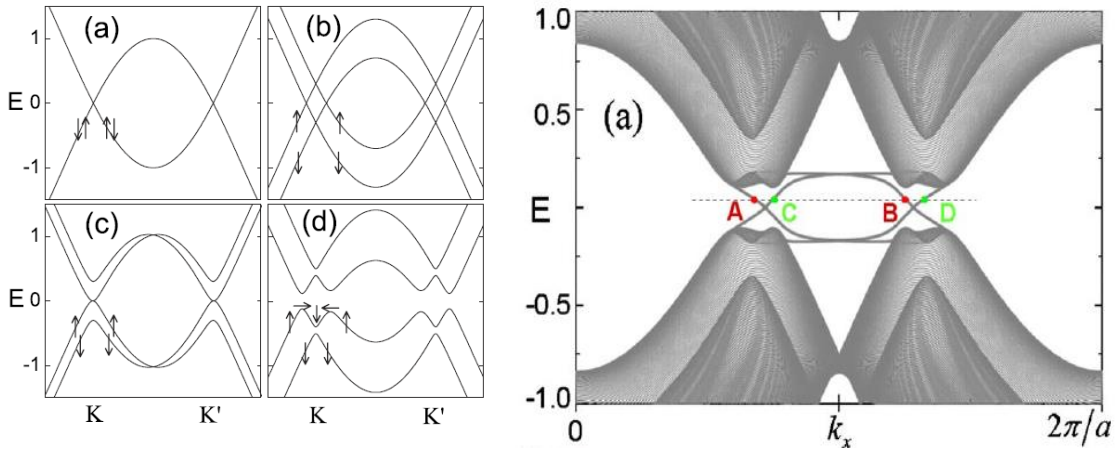

Figure 3-1 Band structures of graphene

Left, band structure evolution of graphene with (a) no Rashba spin-orbit coupling and magnetic exchange field, (b) magnetic exchange field only, (c) Rashba spin-orbit coupling only, and (d) both Rashba spin-orbit coupling and magnetic exchange field. Right figure is the calculated energy spectrum of zigzag-edged graphene ribbons with specific spin-orbit coupling and exchange coupling parameters. Four different edge states A, B, C, and D are present on the Fermi level. [Qiao, *et al. Physical Review Letter* **82**, 161414]

transport properties. Time-reversal symmetry in graphene is broken with the presence of ferromagnetism, which can lead to profound effects on graphene's band structures and electrical transport properties such as the quantum anomalous Hall effect (QAHE)[45], and superconductivity[78]. Similar to the Cr-doped TI, one can expect the realization of QAHE in graphene. It is noted that the Curie temperature in Cr-doped $(Bi_xSb_{1-x})Te_3$ is very low. Since the spin-orbit coupling in the material is already very high. The low Curie temperature must result from the high impurity and disorder level since it is a doped material. But for the proximity-induced ferromagnetism in graphene, the device can be made clean with much fewer impurities and disorder. One can expect high Curie temperature of the ferromagnetism in graphene devices.

In recent papers[45,79], it is proposed that a topological gap can be opened at the Dirac point in graphene with the presence of magnetic exchange field and Rashba spin-orbit coupling. Additionally, it forms topological edge states in the gap, as is illustrated in Figure 3-1. In Figure 3-1 left figure, there are four band structures in graphene under different conditions. (a) is the band

structure in ordinary graphene. (b) is the band structure with the presence of magnetic exchange field only. In this case, the spin degeneracy in graphene is removed and the spin-up and spin-down bands are split. But there is no gap opened. (c) is the band structure with Rashba spin-orbit coupling only, the spins are split but the structure is different with that in (b). No gap exists in this case, either. (d) is the band structure with both magnetic exchange field and Rashba spin-orbit coupling. Not only the bands are spin-split, also there is a bandgap opened near the Dirac point. The gap size is mainly determined by the smaller of the two factors, the exchange field and the Rashba spin-orbit coupling. The right figure is a detailed plot of the band structure in case (d). The Berry curvature is non-zero in case (d) and the QAHE is resulted.

It is known that a pre-requisite for the AHE is the spin-orbit coupling (another one is the broken time-reversal symmetry). The ordinary Hall effect is a result of the Lorentz force provided by the external magnetic field. In traditional conducting ferromagnetic materials, the contribution from the ordinary Hall effect due to the external field only takes up a small fraction of the large Hall signal. The anomalous Hall signal is a result of the strong spin-orbit coupling and spin polarization in the materials. The AHE can be explained by either an intrinsic mechanism or an extrinsic mechanism. The intrinsic mechanism is a result of the band structure effect and the non-zero Berry curvature, whereas the extrinsic mechanism is due to the spin-dependent scatterings of impurities. For the intrinsic mechanism, the AHE conductivity can be calculated by integrating the Berry curvature over all the occupied states. For case (d) in Figure 3-1, when the Fermi level is inside the gap, the integration of the Berry curvature over all the occupied states gives a quantized value for the AHE conductance, which is $2e^2/h$. And the integration remain finite when the Fermi level is out of the gap (in the valence band or conduction band), which gives an unquantized AHE conductance. In traditional ferromagnets, one can always have unquantized AHE. But in graphene, it is a wonderful system because, at least in theory, there is such a marvelous quantized Hall effect in zero

magnetic field. (When we say zero magnetic field, we imply the magnetization has perpendicular anisotropy.)

In order to realize QAHE in graphene, as is pointed out in the previous paragraph, magnetic exchange field and strong spin-orbit coupling should be provided simultaneously, which cannot be easily satisfied. We firstly came up with the high-quality yttrium iron garnet (YIG) thin films deposited in our pulsed laser deposition system. The YIG film is a ferrimagnetic material with atomically flat surface and chemical and magnetic stability in air. It can provide graphene with the magnetic exchange field when they are close enough to each other. As for the spin-orbit coupling in graphene, the carbon atoms have a low atomic number and therefore low intrinsic spin-obit coupling[80], ~ 10 μeV. Generally, the spin-orbit coupling is the interaction between the electron's spin and orbital degrees of freedom. An electric field to a moving electron behaves like a magnetic field which acts on the electron's spin. For the intrinsic spin-orbit coupling, it is the interaction between the positively charged atomic nucleus and the moving electrons. For elements with low atomic numbers, the electric field generated from the nucleus is weak. Therefore, the interaction between the nucleus and electrons is weak, which means a weak intrinsic spin-orbit coupling. For elements with high atomic numbers, the intrinsic spin-orbit coupling is much stronger. Although graphene's intrinsic spin-orbit coupling is weak, there is also extrinsic spin-orbit coupling. With an external electric field, there is a Rashba spin-orbit coupling between the electrons and the external field. This external field can be provided by a certain substrate, which can create asymmetric potential above and below the device and thus a perpendicular electric field. For graphene grown on substrates, strong Rashba spin-orbit coupling (225 meV) has been observed[81,82]. The Rashba spin-orbit coupling is also expected to be provided by the YIG film. In addition to the magnetism and Rash spin-orbit coupling, YIG is insulating, which means there will not be any shunting current from the film. It is very difficult to have all the required properties together just in one material.

But YIG does. In this dissertation, yttrium iron garnet (YIG) thin films are deposited on a gadolinium gallium garnet substrate in a pulsed laser deposition system, which will be described in next section.

3.1.2 Yttrium Iron Garnet

As is mentioned in the previous section, yttrium iron garnet (YIG) is a ferrimagnetic material with a Curie temperature T_C = 550 K. A ferrimagnetic material is one that has atoms with opposing spin orientations below the Curie temperature. But the populations of the opposing spins are unequal so that there is a spontaneous magnetization in the material. Figure 3-2 is a unit cell of YIG. The chemical composition of YIG is $Y_3Fe_5O_{12}$ or $Y_3Fe_2(FeO_4)_3$, in which 3 yttrium atoms are

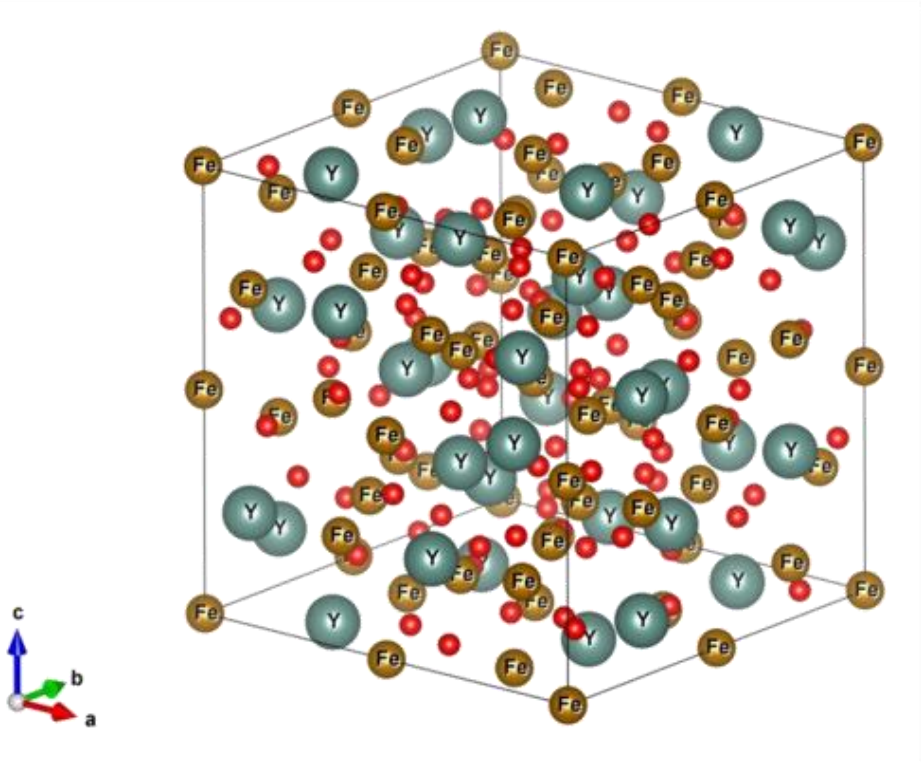

Figure 3-2 YIG unit cell
Blue, brown and red spheres represent yttrium, iron and oxygen atoms, respectively

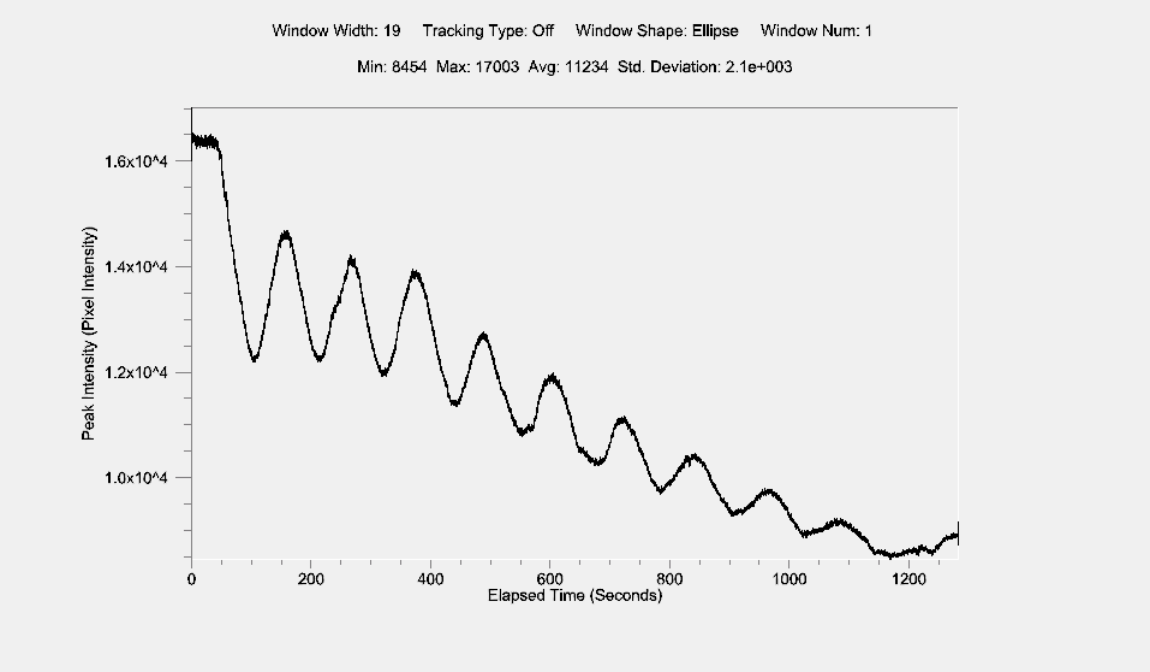

Figure 3-3 RHEED intensity oscillations
Each period in the oscillation corresponds to one layer of deposition. Oscillations tend to be attenuated with the growth process. However, annealing in oxygen environment can recover the oscillations.

coordinated by 8 oxygen atoms (octahedral site) in an irregular cube while 3 iron atoms are surrounded by 4 oxygen atoms (tetrahedral site, -FeO_4 in the formula) and the other 2 iron atoms are in the octahedral sites. The magnetism of YIG is determined by the iron atoms. The iron atoms in the two different chemical environments have different spin orientations. Since there are 3 iron atoms in the tetrahedral site and 2 iron atoms in the octahedral site, the iron atoms with spin-up electrons are not equal to the iron atoms with spin-down electrons, which leads to a net magnetization in the material.

20 nm YIG thin films are deposited on gadolinium gallium garnet (GGG) substrates in a pulsed laser deposition system[77]. Epitaxial deposition is realized in the growth of YIG thin films. Reflection high-energy electron diffraction (RHEED) pattern shows oscillations during the growth,

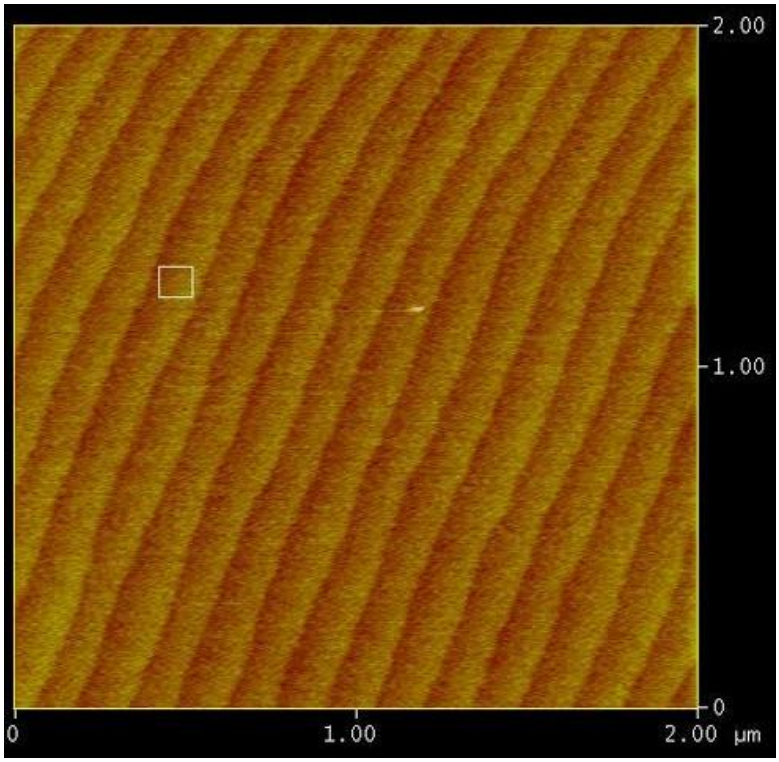

Figure 3-4 AFM image of a YIG thin film
Atomic terraces can be seen in the AFM images of YIG (110) thin film. The mean roughness within one terrace is only 0.066 nm, as is shown in the white square, indicating extremely flat surface.

indicating the layer-by-layer deposition of YIG thin film. When one new layer of YIG film starts to form, the RHEED intensity decreases. As the layer is growing and half-full layer is formed, the intensity reaches minimum. When it finally forms a full layer, the RHEED intensity recovers. One oscillation corresponds to one layer of YIG film deposition, as is illustrated in Figure 3-3. The films are then annealed in an oxygen-flowing furnace at 850 ℃ for 6 hours with slow heating and cooling rate to minimize oxygen deficiency.

Atomic force microscopy (AFM) is performed on the YIG thin films to further confirm the atomic layer-by-layer deposition with a Veeco Dimension 5000 atomic force microscope. Figure 3-4 is an AFM topographic image of a YIG film. The parallel lines are the edges of atomic terraces separated with the atomic height. The width of the terraces is about 150 nm while the height is only

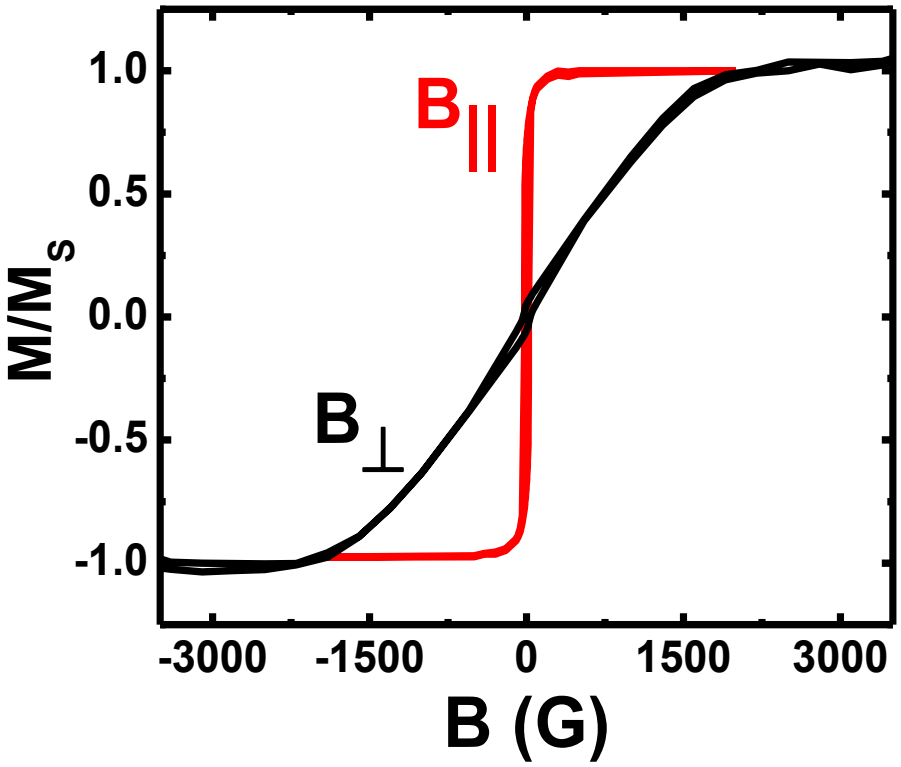

Figure 3-5 Magnetic hysteresis loop of a YIG film
At room temperature, YIG thin film has in-plane anisotropy. The hysteresis loops of both in-plane and out-of-plane direction are small. The saturation field on the out-of-plane direction is ~ 2000 G.

0.45 nm. And the mean roughness within on terrace is only 0.066 nm, as is indicated in the white square. This less-than-1-Å roughness means the extremely flat surface of the YIG thin film. Moreover, the each terrace has a width ~ 140 nm while the height is only 0.45 nm, which means the tilt angle is only less than 0.2 °. However, the atomic terraces cannot always be observed. But the mean roughness is always less than 0.1 nm for all the YIG films no matter the atomic terraces are observed or not. This extremely flat surface is essential for the transferred graphene device, with which graphene is able to have intimate contact with the YIG surface so that strong proximity effect could be induced. Moreover, the flat YIG substrate surface greatly reduces external disorder and suppresses electron scatterings in graphene, which is good for maintaining high carrier mobility.

Room temperature magnetic hysteresis loop is measured in a Lakeshore vibrating sample magnetometer system (VSM) to characterize the magnetization in the as-grown YIG thin films. A typical room temperature magnetic hysteresis loop of the film is shown in Figure 3-5. Evidently, the YIG film has in-plane anisotropy, which is demonstrated by both of the in-plane and out-of-plane magnetic hysteresis loops. The in-plane anisotropy energy is small because of the small in-plane saturation field and coercive field, usually less than 20 G and a few G, respectively. And the in-plane hysteresis loop is also small. In the out-of-plane direction, the coercive field and hysteresis loop are still small. The corresponding saturation field has a value around 2000 G. The loop has a typical hard-axis behavior[77]. Here it needs to be point out that the out-of-plane saturation field has sample-to-sample variation in a range of 1500 G to 2500 G due to the uncontrolled deposition parameters and condition fluctuations.

3.2 Device Fabrication

3.2.1 Device Fabrication on SiO_2/Si

One would like to fabricate graphene devices on YIG/GGG substrate with the same way on SiO_2/Si substrate. However, it is of great difficulty to do it on YIG/GGG substrates. First of all, the mechanically exfoliated single-layer graphene flakes are nearly invisible on YIG substrates and are difficult to be identified. The color contrast between single-layer graphene and bilayer graphene on YIG substrates under the optical microscope is not sufficient enough to tell. Second, the YIG film and GGG substrate are thick and insulating, which could easily accumulate electron charges so that electron beam can easily be deflected away from the substrate and patterns could not be wrote during electron beam lithography. Then a universal method is developed to transfer the entire

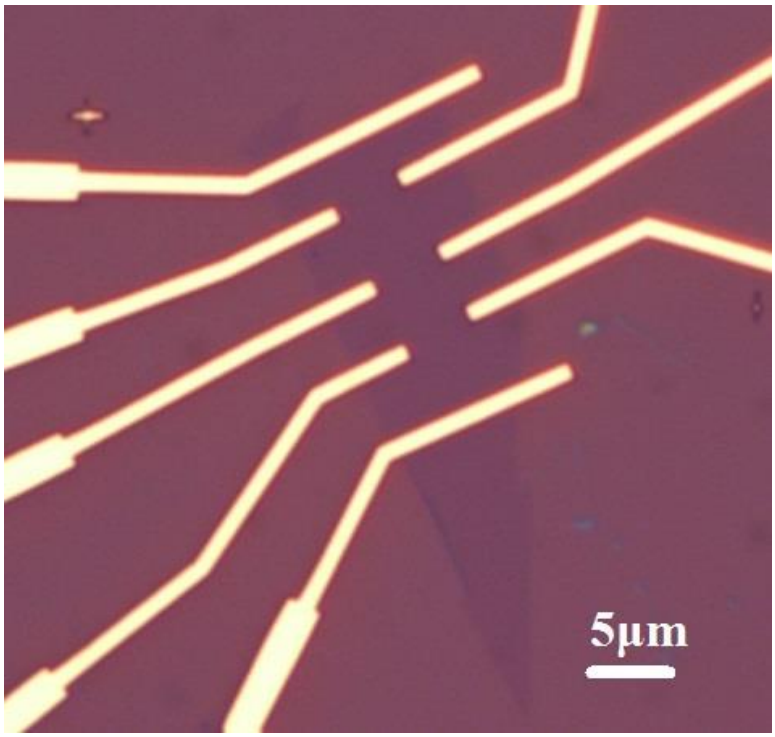

Figure 3-6 Graphene device fabricated on SiO_2/Si

device from SiO_2/Si substrates to any other flat substrates, which was successfully performed to transfer graphene devices to strontium titanate substrates[83].

Single-layer graphene flakes are mechanically exfoliated on 290-nm SiO_2 atop highly doped Si substrate. Then they are spin-coated with one layer of MMA and one layer of PMMA at a speed of 3600 rpm with a ramping rate of 10000 rpm/s (as fast as possible) and baked on a hot plate at 150 ℃ for MMA layer and 180 ℃ for PMMA layer for 5 minutes, separately. Then alignment marks are patterned with an electron beam lithography system (Leo SUPRA 55). After developing the alignment marks, optical microscope images of the graphene area with alignment marks are taken for electrode pattern design and following by another time of electron beam lithography of the electrodes pattern. To develop this MMA/PMMA resist, a solution with the ratio of MIBK (methyl isobutyl ketone): IPA (isopropyl alcohol) = 1: 3 is employed. The developing time is 65 s. More

time might be needed if the resist is not fully developed. Finally, 80 nm Au (gold) electrodes are deposited in an electron beam evaporation system (Temescal BJD-1800). A typical nanofabricated Hall bar geometry graphene device on SiO_2/Si substrate is show in Figure 3-6. The devices are then transferred to YIG/GGG substrate after some preliminary electrical characterization.

3.2.2 Device Transfer Technique

To perform the transfer process, two layers of PMMA is spin-coated at a speed of 3000 rpm with a ramping rate of 1500 rpm/s. Each layer of PMMA is baked on a hot plate at 170 ℃ for 10 min. Then the entire chip (PMMA layer, graphene device with Au electrodes and SiO_2/Si substrate) is soaked in 1 M NaOH solution for 2 days to etch the SiO_2 layer in the substrates. After the top SiO_2 layer is etched up by NaOH, the PMMA layer with graphene device will be released from the SiO_2/Si substrate. It is worth to point out that the SiO_2 layer will not be completely etched by this process, only the top portion of SiO_2 layer is being etched up. Moreover, this etching process also depends on the quality of SiO_2 layers. For some SiO_2/Si substrates used in this dissertation, the etching process is very slow, and it can take up to a couple of weeks to release the PMMA layer. One efficient way to speed up the process is to heat the NaOH solution to a higher temperature. But the risk is to have air bubbles around the PMMA layer, the substrate, and even between the device and substrate. Sometimes, the buoyant force from the air bubbles are unbalanced and strong enough to flip the entire substrate.

When spin-coating, the PMMA resist will spread over the entire SiO_2/Si substrate. And for most of the time, the resist will also spread to the edges and corners of the substrate, bypass SiO_2 layer and stick to the Si substrate, which slows down the etching process and increases the difficulty of releasing the PMMA layer. After soaked in NaOH solution for two days, some corners and edges

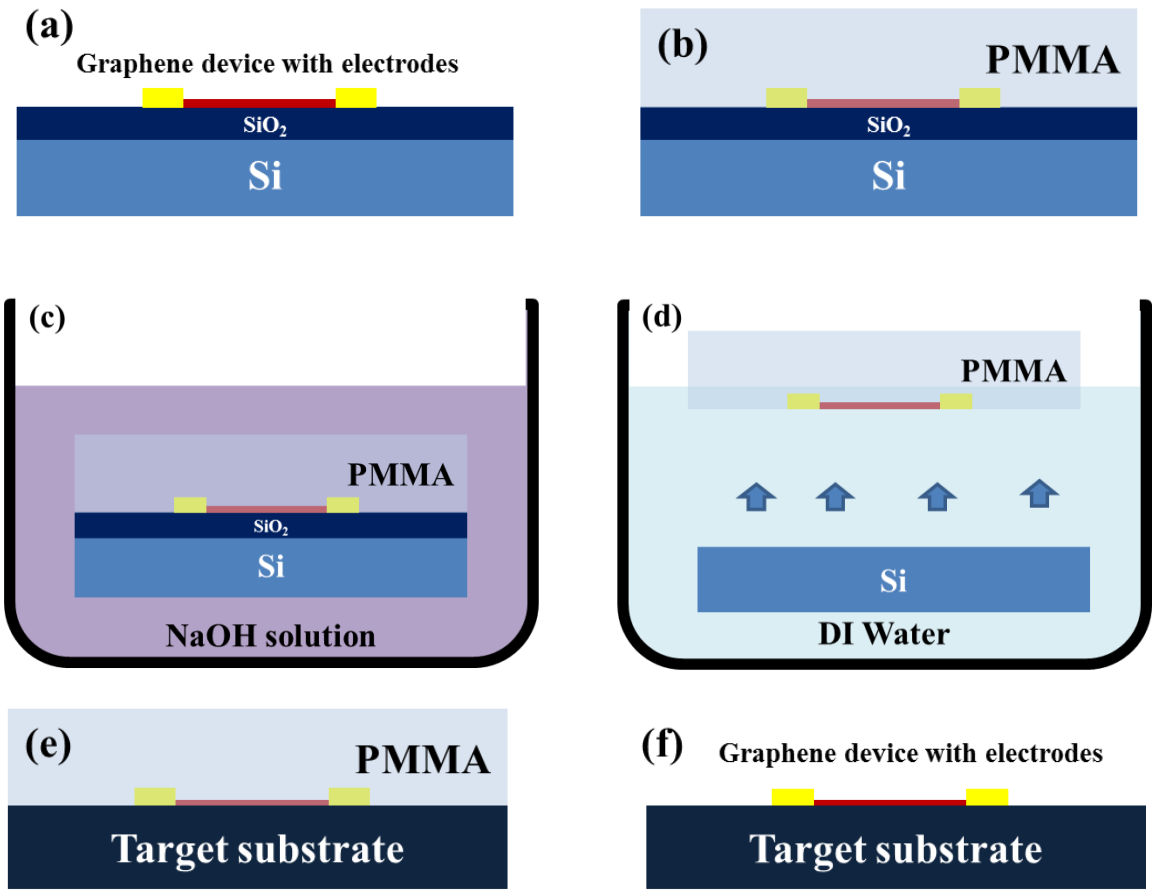

Figure 3-7 Device transfer technique

of the PMMA layer are floating in the solution while the rest is still stick to the substrate. Then the chip is transferred to a beaker with sufficient DI water. The PMMA layer can be released by careful removing the sticking part with tweezers. Target substrate can then be put under the PMMA layer with caution. Sometimes, the sticking part can be very difficult to remove, so pretreatment can be done before the etching process. Removing the PMMA on all the corners and edges except for one corner will make this process much easier.

In this chapter, the YIG/GGG substrate is used as the target substrate. After the transfer, the YIG/GGG substrate is baked on a hot plate at 50 ℃ for 5 – 10 min. During this step, some slightly

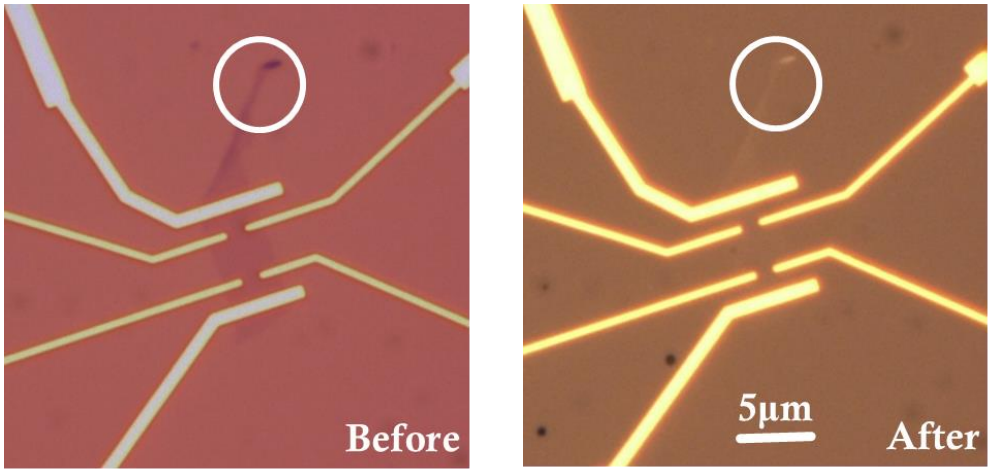

Figure 3-8 Optical Images of a graphene device before and after transfer
Left figure is the graphene device before transfer on SiO2/Si substrate. Right figure is the graphene device after transfer on YIG/GGG substrate. Single-layer graphene is nearly invisible on YIG/GGG substrate, but multilayer part could be identified.

wrinkled part can be spread out flat to some extent. It also helps graphene and the electrodes to stay firmly on the substrate. After that, the substrate is put into acetone to lift-off PMMA resist and followed by rinse in IPA. The device should be handled with caution and slow motion when in acetone or IPA. At last, it can be dried by a slow-flowing nitrogen gas. The whole transfer process is illustrated in Figure 3-7.

Graphene is extremely difficult to locate in YIG substrate. Only careful observation can give its shape profile. However, the multilayer graphene can still be identified. In Figure 3-8, the left figure is a graphene device before transfer. Both single-layer and multilayer graphene can be seen. The right figure is the same graphene device after transferred to YIG/GGG substrate. Only the multilayer part of the flake is visible in the optical image, while the single layer part turns to nearly invisible. The visible multilayer part of the graphene flakes and the metal electrodes indicate the success of this transfer technique.

3.2.3 Top Gate Fabrication

Normally with the SiO_2 atop highly-doped Si substrate, Si is conductive and the back gate can be applied through the SiO_2 layer. But in the transferred device, both YIG and GGG are insulating. Moreover, the GGG substrate are 500-μm thick. The application of the back gate becomes impossible. To tune the carrier density in the transferred graphene device, one has to fabricate a top gate on the device. Considering that any dielectric deposition involves different environmental influence to the device so as to affect the device quality and mobility, the PMMA and MMA resist is adopted as the top gate dielectric. This may also be the easiest way. A layer of PMMA or MMA is spin coated on the device/substrate at a speed of 3600 rpm with a ramping rate of 10000 rpm/s. Then it is baked on a hot plate at 170 ℃ for 20 min. After naturally cooled down to room temperature, a gold wire with 0.002 inch in diameter (99.995%, Alfa Aesar) is attached to the PMMA or MMA layer right on top of the device area with high purity silver paint (SPI Supplies). The device schematics can be represented in Figure 3-9.

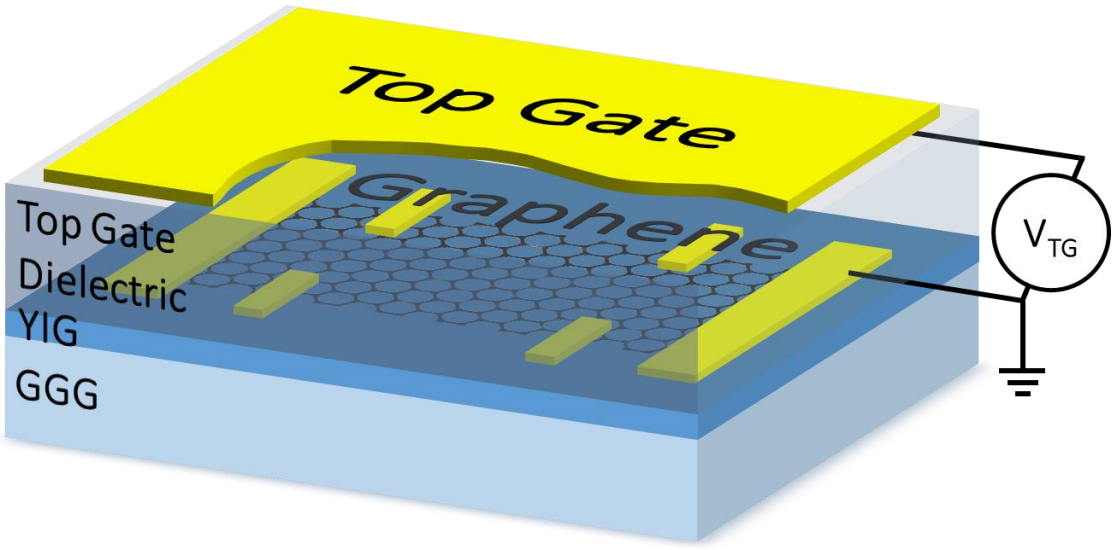

Figure 3-9 Device schematic diagram
The top gate is fabricated with silver paint and gold wires which connects to the voltage source.

When using this type of polymer gate dielectric, gate leakage can be occasionally found. This could have several possible reasons. The major probability should be the cracks in the polymer layer and they are happened to be at the position close to the device or device electrodes. When top gate electrode wire is attached, silver paint diffuses into the cracks and establishes weak connection between the device and ground. Another issue that needs to be paid attention to is the thermal expansion and contraction of the polymer layer when cooling or heating. Rapid temperature change can induce huge stretching force which could damage the contact between graphene and electrodes or even damage the graphene flake.

3.3 Graphene Characterization

3.3.1 Raman Spectroscopy

Raman spectroscopy is an effective tool to characterize graphene's thickness and quality (disorder can be reflected from the D peak intensity in Raman spectrum). So room temperature optical Raman spectroscopy is employed to characterize both bare graphene exfoliated on SiO_2/Si substrate and the transferred graphene device on YIG/GGG substrate before top gate fabrication with a 532-nm laser. Figure 3-10 is the Raman spectra of the transferred graphene device (purple), the bare graphene (red) and YIG thin film only (blue). Graphene's G peak (~1580 cm^{-1}) and 2D (~2700 cm^{-1}) peak[84] can be clearly observed in the spectra of both bare graphene and transferred device. And no obvious D peak (~1350 cm^{-1}) is detected in both cases, implying no observable defects is introduced during the transfer process. Moreover, the YIG's characteristic peaks between the measured ranges (from 1100 to 3000 cm^{-1}) can also be identified in the transferred device's spectrum. Generally, the Raman spectrum of the transferred device is the sum of those of bare graphene and YIG thin film, suggesting the success of the transfer process.

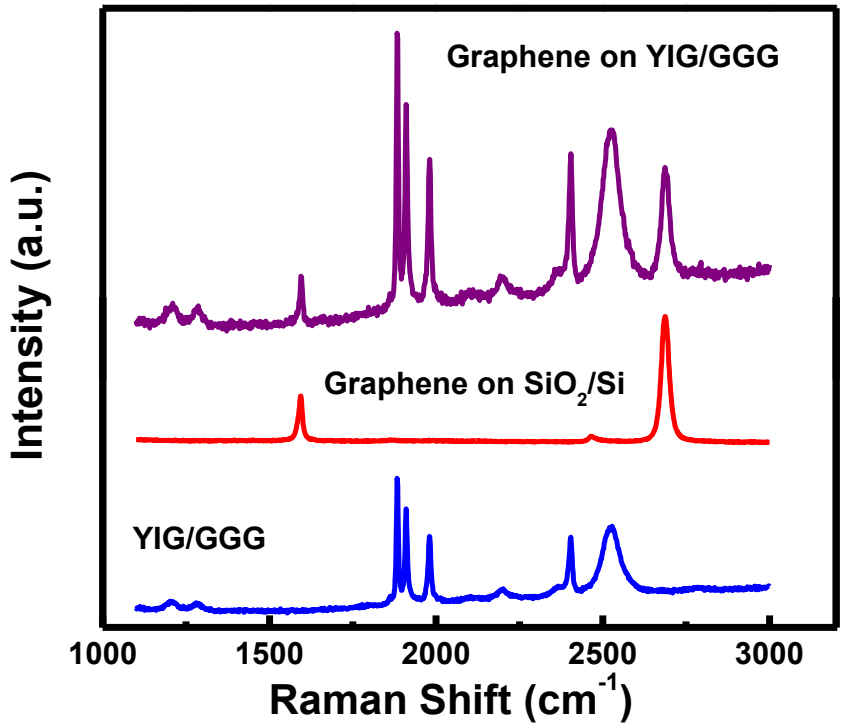

Figure 3-10 Raman spectroscopy of graphene and YIG films
Purple, red, and blue lines are room temperature Raman spectra of graphene on YIG thin film, graphene on SiO2/Si substrate and YIG thin film on GGG substrate , respectively

3.3.2 Gate Modulations

After the nanofabrication of the devices on SiO_2/Si substrate and before the transfer process, room temperature transport properties are measured to characterize the pristine states of the devices. Back gate is applied through the SiO_2 dielectric layer to tune the Fermi level and carrier density in the devices. After transfer, the use of back gate becomes impossible since the thickness of YIG/GGG substrate is ~ 0.5 mm and YIG/GGG is insulating and its dielectric constant is not high. Hence, the devices are fabricated with a top gate described in Section 3.2.3 due to the difficult of the back gating through the thick, insulating, and low-dielectric-constant YIG/GGG substrate.

4-terminal resistance and Hall effect are measured with Stanford Research SR830 Lock-in amplifiers at 300K and low temperatures in a Quantum Design's Physical Property Measurement System (PPMS). The back/top gate dependence of the same device before and after transfer is shown in Figure 3-11. For a neutral graphene without impurities and disorder, the Fermi level crosses its Dirac point, where the density-of-states is zero, indicating an infinite resistance. However, in as-fabricated graphene devices, impurities and disorder are unavoidable, which results in a shift of the Fermi level and a finite resistance at the Dirac point. So usually the Dirac point is not exactly at zero gate. And the deviation of the Dirac point away from the zero-gate, as well as the width of minimum resistance in gate voltages, represents the impurity level to some extent, which will be discussed in Section 3.5. Moreover, in the region away from the Dirac point, due to the linear energy dispersion in graphene, the carrier density changes linearly with the change in gate voltages. According to the Drude's model, $\sigma = ne\mu$, where σ is the conductivity, n is the carrier density, e is electron charge and μ is the mobility, the conductance or resistance also changes linearly with the change in gate voltages.

Due to the difference of the dielectric materials used for the back gate and top gate, the conductivities are scaled by the effective capacitances per unit area calculated from quantum Hall effect measurement which will be discussed in Section 3.3.3. From the equation of parallel capacitors, $Q_S = C_S \cdot V$, where Q_S is the area charge density, C_S is the capacitance per unit area and V is the voltage across the capacitor, it can be deduced that $e \cdot n_{2D} = C_S \cdot V_g$, where n_{2D} is the carrier density, e is the electron charge, C_S is the effective capacitance per unit area and V_g is the corresponding gate voltage. With the change in gate voltage, carrier density changes, $e \cdot \Delta n = C_S \cdot \Delta V_g$. where Δn is the carrier density change and ΔV_g is the change in gate voltage. For graphene with low density, Drude's model can be applied. Then one have $\sigma_{xx} = e\mu n_{2D}$ and $\Delta\sigma_{xx} = e\mu\Delta n_{2D}$. With the equations derived above, the relationship between the conductivity scaled by capacitance per

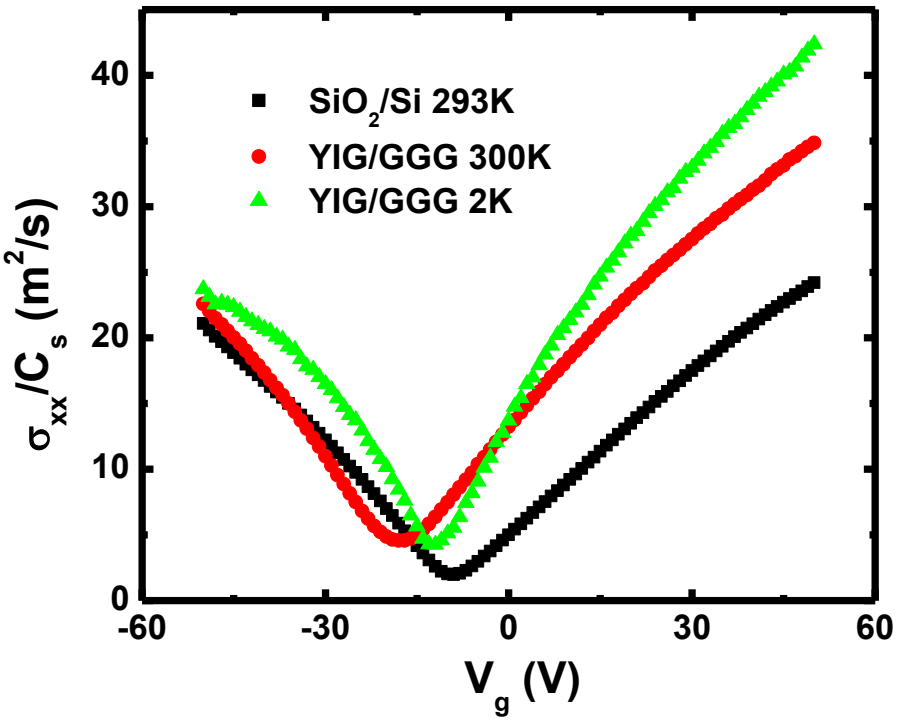

Figure 3-11 Gate dependence of σ_{xx} scaled by C_S

Black curve is back gate voltage dependence of σ_{xx}/C_S on SiO_2/Si substrate at room temperature. Red and green curves are top gate voltage dependence of σ_{xx}/C_S on YIG/GGG substrate at 300 K and 2 K, recpectively.

unit area and gate voltage can be deduced, which is $\sigma_{xx}/C_S = \mu V_g$ or $\Delta\sigma_{xx}/C_S = \mu\Delta V_g$. The slope of the σ_{xx}/C_S vs. V_g reflects the field-effect mobility of the carriers in graphene.

Before transfer, the Dirac point of the device in Figure 3-10 is around V_g = -9 V and the field-effect mobility is ~ 6000 $cm^2/V{\cdot}s$. After the device is transferred to YIG/GGG substrate, the Dirac point is shifted to V_g = -18 V at 300 K and is shifted back a little to V_g = -13 V at 2 K. Moreover, the slope of σ_{xx}/C_S vs. V_g curve actually increases a little after transfer, meaning an increase in the field-effect mobility. When the temperature is cooled to 2 K, the mobility further increases to 10000 $cm^2/V{\cdot}s$ on the electron side. The increased mobility in the transferred device reveals that none of

the transfer process, the YIG thin film and the top gate dielectric material (MMA or PMMA) are factors adversely affecting the graphene's quality. This is also a further evidence of the extremely flat surface of the YIG thin films. For all the 8 devices studied, the mobility either decreases or increases slightly, no significant change in mobility is found.

3.3.3 Quantum Hall Effect

At low temperatures and under strong magnetic fields, electrons in a two dimensional system will travel in circular cyclotron orbits, which are discrete and quantized and known as the Landau levels. The Landau levels are highly degenerate at very low temperatures. With such conditions, the Hall conductance is quantized to certain discrete values in the unit of e^2/h, which is known as the quantum Hall effect (QHE). The discrete values, known as the filling factor ν, are usually integers for 2D electron systems. Then one have $\sigma_{AHE} = \nu \frac{e^2}{h}$. But for a system with Dirac fermions, for instance graphene, the filling factors are $\nu = \pm 4(n+1/2)$, where n is the Landau level index which is a non-negative integer. At the 0^{th} Landau level ($n = 0$), the filling factor ν is 2, corresponding to a Hall conductance of $2e^2/h$, known as the half-integer QHE, which is the hallmark of graphene.

The Quantum Hall effect (QHE) measurement is performed on graphene devices on both SiO_2/Si substrate and YIG/GGG substrate. Figure 3-12 is the QHE gate dependence of a device on SiO_2/Si substrate at 2 K in a constant 10 T perpendicular magnetic field. The Dirac point is very close to zero in this device. And the 0^{th} Landau level plateaus in R_{xy} on both electron and hole sides with the quantum conductance value of $2e^2/h$ can be clearly seen in the vicinity of the Dirac point. And so do the higher Landau level plateaus. The filling factors are marked at each Hall plateau.

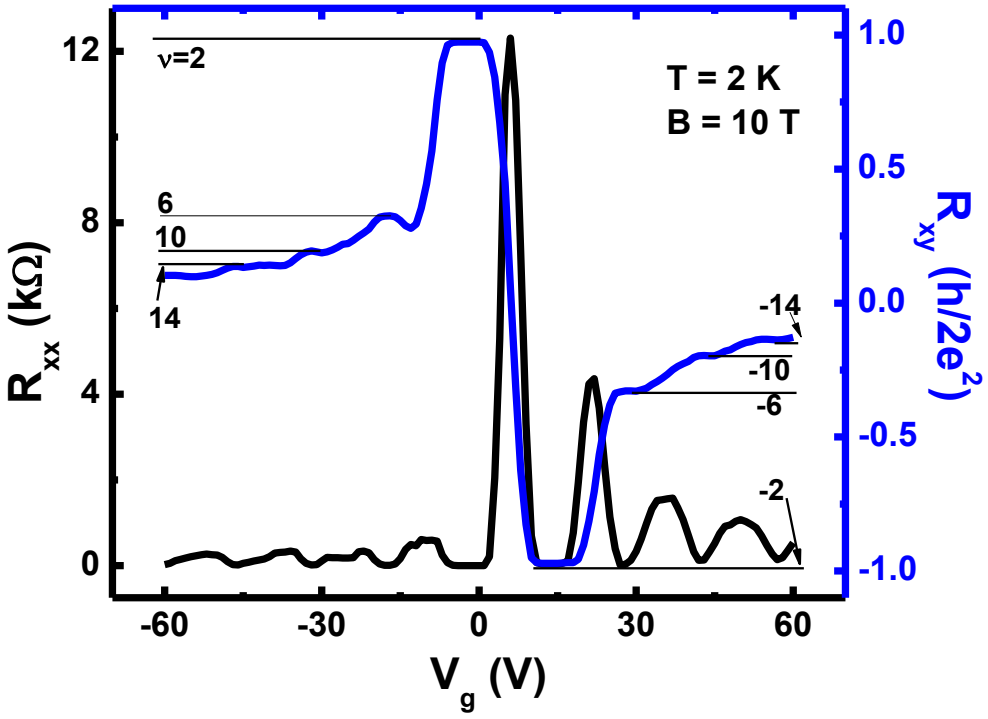

Figure 3-12 QHE gate dependence in graphene on SiO_2/Si
Quantum Hall effect is performed at 2 K in a constant 10 T perpendicular magnetic field. Quantum Hall plateaus in Rxy and oscillations in Rxx can be both seen indicating high quality in graphene device.

Quantum oscillations, in which R_{xx} goes to zero at the R_{xy} plateaus and then maximum when R_{xy} changes values, are observed in the longitudinal resistance when back gate voltage is swept.

Figure 3-13 is the QHE magnetic field dependence of a device on YIG/GGG substrate at 2 K with zero gate voltage. The carrier density at zero gate voltage is very low so that only the 0^{th} Landau level can be observed. In the longitudinal resistance curve, before the resistance reaches 0, two peaks on both side of the magnetic field can be seen, which could be the 4 split sub-levels in the 0^{th} Landau level.

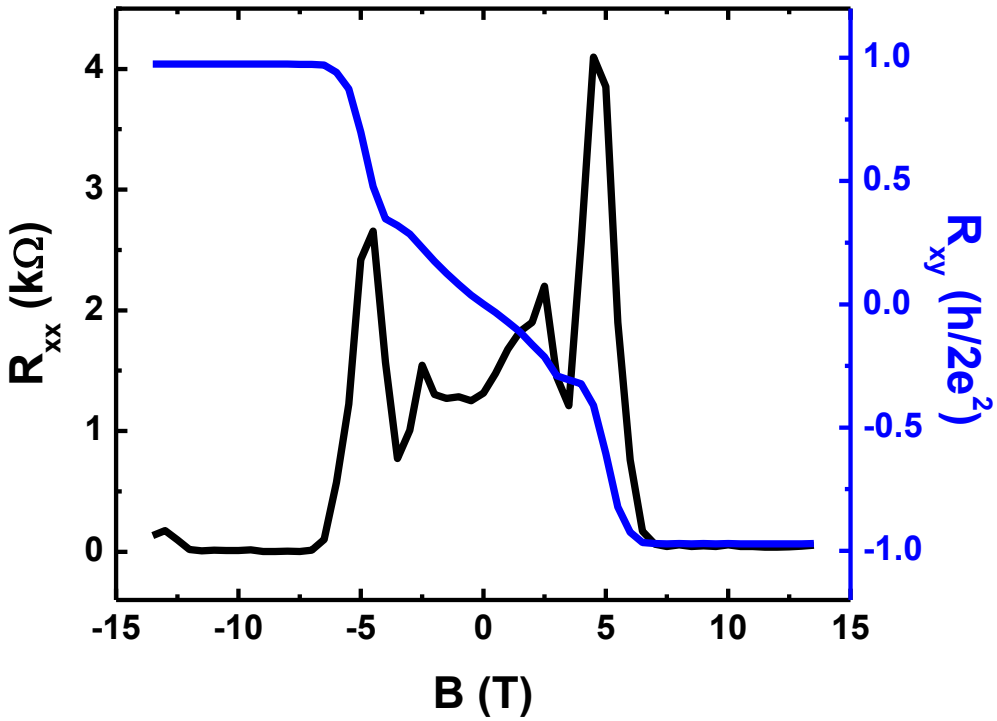

Figure 3-13 QHE magnetic field dependence in graphene YIG/GGG
Quantum Hall effect is performed at 2 K with no top gate voltage applied. Only 0th Landau level can be observed since the carrier density is very low in this device and the Dirac point is very close to 0 top gate voltage.

Figure 3-14 is the QHE top gate dependence of a device transferred to YIG/GGG substrate at 2 K in a constant 8 T perpendicular magnetic field. The curves are quite similar to the one on SiO_2/Si substrate. The Landau level plateaus in Hall resistance and quantum oscillations in the longitudinal resistance can be clearly observed. Filling factors are marked on the corresponding plateaus. Less Landau levels are observed in this figure when gate voltage is changed within the same range. This is mainly determined by the applied perpendicular magnetic field and the effective capacitance per unit area of the dielectric materials.

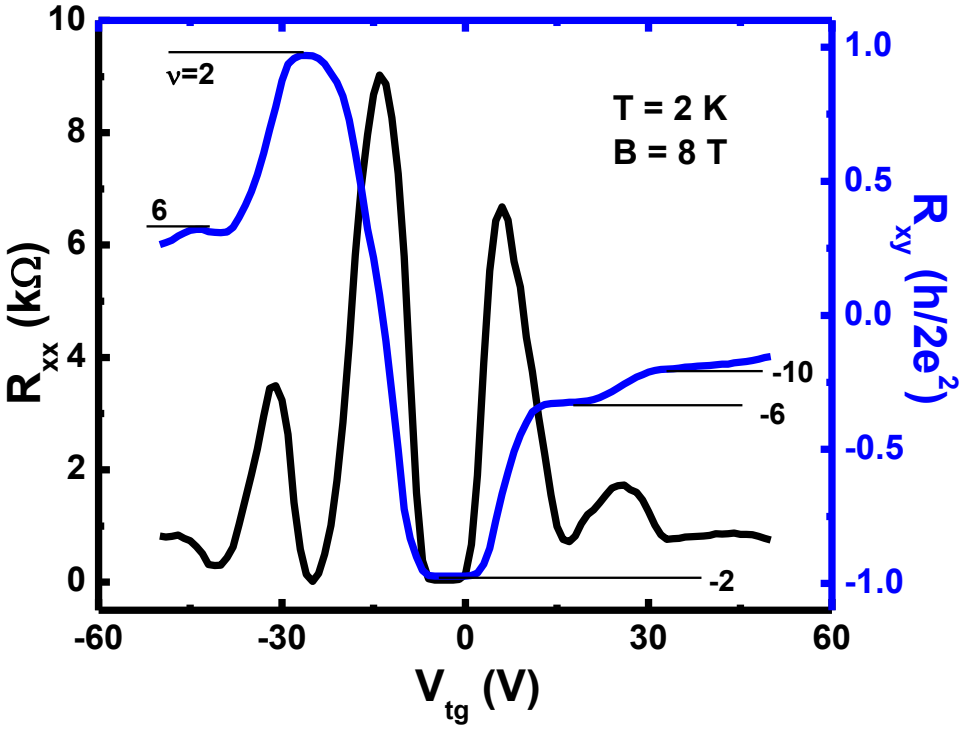

Figure 3-14 QHE gate dependence in graphene YIG/GGG
Quantum Hall effect is performed at 2 K in a constant 8 T perpendicular magnetic field. Quantum Hall plateaus in Rxy and oscillations in Rxx can be both seen indicating high quality in the transferred device and the transferred technique is quite successful without adversely affect the device's mobility

For each Landau level, the carrier density required to fully fill that Landau level is $n_{L.L.} = g\frac{eB}{h}$, where $n_{L.L.}$ is the carrier density required to fully fill each Landau level under that B field, g is the spin and valley degeneracy, considering there are both spin and valley degeneracy in graphene, g is equal to 4. When the gate voltage is changed, the carrier density changes in graphene. When the Landau levels are fully filled, the Fermi level is in the gap between two adjacent Landau levels. So no density of states can be found on the Fermi level, there are only conducting channels on the edge which is in the regime of ballistic transport. With four terminal resistance geometry, the longitudinal voltage goes to 0 at this point. The change in gate voltage between two adjacent dips

or peaks corresponds to the change of carrier density required to just fully fill one Landau level. Then one can obtain $\Delta n_{2D} = n_{L.L.} = g\frac{eB}{h} = \frac{4eB}{h}$. With the relationship between charges and voltages of a parallel capacitor $e \cdot \Delta n_{2D} = C_S \cdot \Delta V_g$, the corresponding effective capacitance per unit area can be calculated, $C_S = \frac{4e^2B}{h}/\Delta V_g$. With the Q data in Figure 3-11 and 3-13, the effective capacitances per unit area of the dielectric materials, SiO_2 and MMA can be calculated, which are $C_{S,SiO2}$ = 1.0 $\times 10^{-4}$ F/m^2 and $C_{S,MMA}$ = 7.4$\times 10^{-5}$ F/m^2.

Another way to calculate the capacitance is based on the gate dependence. From the Hall effect data, the carrier density can be extracted. With the changes in gate voltage and carrier density extracted from Hall effect, another capacitance can be calculated by using $C_S = \Delta n_{2D}/(e \cdot \Delta V_g)$ or taking the derivative of the n_{2D} vs. V_g curve. The capacitances per unit area extracted from the Hall effect have high consistency with the values calculated from the quantum Hall effect.

The third way to calculate capacitance is to use the equation of a parallel capacitor, $C_S = \frac{\varepsilon_0 \varepsilon_r}{d}$, which was used to calculated the effective capacitance in Chapter 2. However, this calculation is not applicable with organic dielectric layers. In the graphene devices, the top gate dielectric, MMA and PMMA are organic materials dissolved in solutions, spin-coated on the device and baked on a hot plate. There are many factors influencing the estimation of its dielectric constant, such as the density, the baking environment, baking temperature fluctuation, thickness, the homogeneity of the resist, etc. Without an accurate dielectric constant, this method is not a good approach in obtaining the effective capacitance in this material. In this dissertation, the value used for capacitance per unit area is based on the experimental data which is from the QHE and Hall effect measurements.

3.4 Anomalous Hall Effect in Graphene on YIG

3.4.1 Hall Effect in Graphene on YIG

After the characterization of the device, Hall effect measurement is performed to study the proximity-induced effect induced in the transferred graphene device. At 300K, a straight line of the Hall effect signal is obtained. However, when the temperature is lowered, the Hall effect signal starts to have curvatures. At the lowest temperature that the system can reach, which is 2 K, the curvature reaches the maximum. Figure 3-15 is a typical Hall effect curve at 2 K. The red line is a guide to the eye. It is a straight line with the same slope as the high field part which is due to the ordinary Hall effect. After carefully removing the linear ordinary Hall background (red line), a nonlinear curve is immediately obtained, as is shown in Figure 3-16.

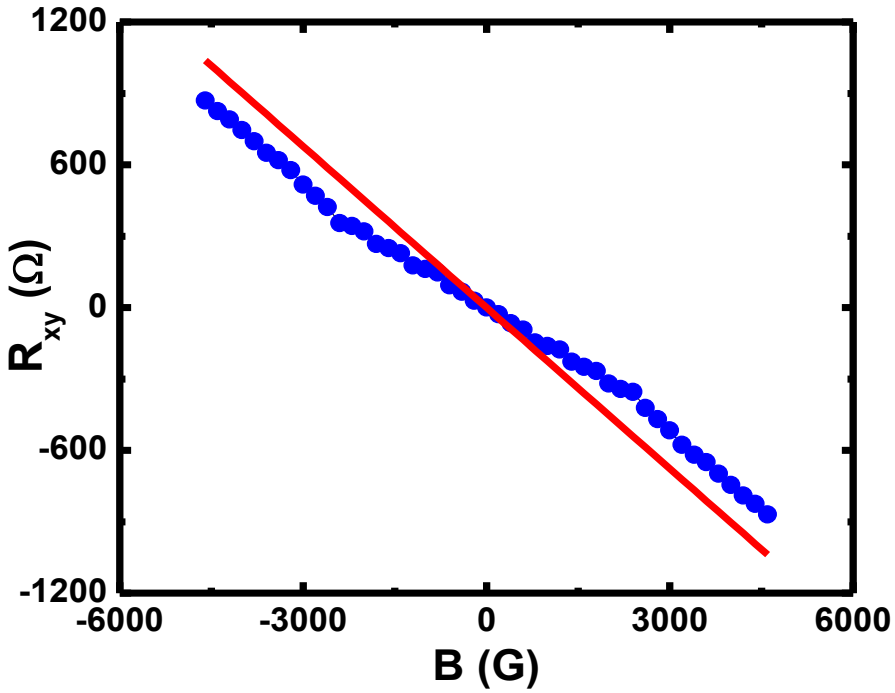

Figure 3-15 Overall Hall signal of a transferred graphene device
The Hall effect is performed at 2 K in a perpendicular magnetic field. Clear nonlinear feature is present indicating the AHE in the transferred device. Red line is a linear fit of the ordinary Hall background.

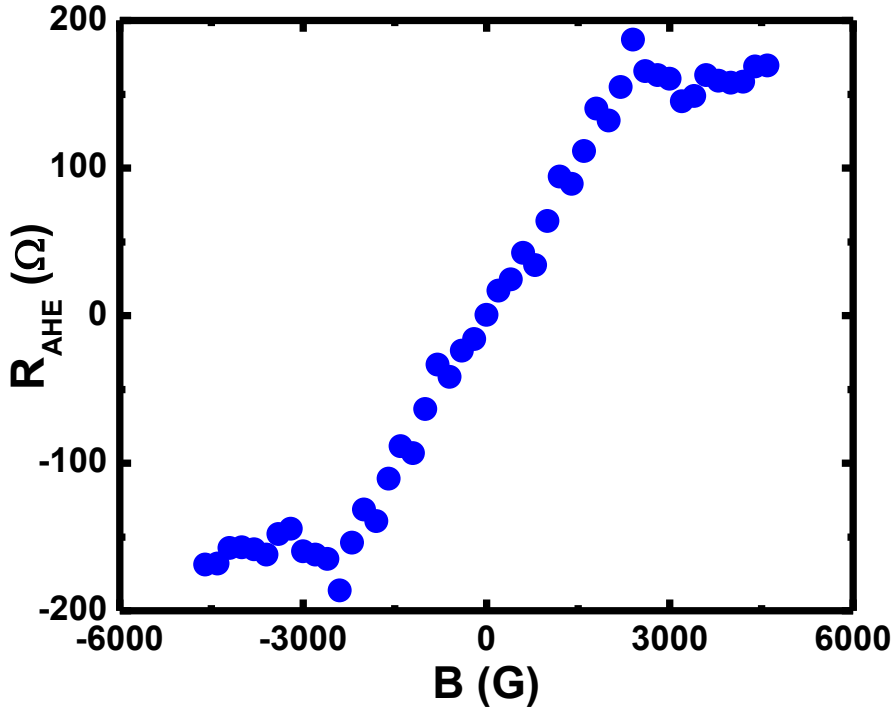

Figure 3-16 AHE in the transferred graphene device
After carefully remove of the ordinary Hall effect background (linear part) in Figure 3-14, A nonlinear curve with a saturation field of 2200 G is obtained.

Another way to remove the linear background is to linear-fit on the high field part (>2500 G), and then subtract a straight line passing through the origin with a slope extracted from the linear fit. However, at low temperatures, the raw data always contains some unexpected additional features, such as dips and peaks, resistance fluctuations, creating uncertainty in extracting the ordinary Hall effect signal. Since the resulting nonlinear curve is small compared to the overall curve, little uncertainty in the ordinary Hall part could result in big difference in the nonlinear curve. What's more, in the high field range, there will be quantum oscillations or other unrelated phenomena. Linear fit on high field part is not a preferred way, especially at low temperatures.

This nonlinear curvature appeared at low temperatures could have two possible sources. One is from the two-band Hall effect mixing, which are two parallel channels of carriers with different mobilities[73]. Another is the AHE induced by the magnetization of the YIG thin film. There are several pieces of evidence supporting the latter case. First of all, for all the transferred devices studied, the saturation field is always around 2000 G, for example in Figure 3-16, the saturation field is 2200 G. If this is the anomalous Hall effect, its origin must be from the magnetic substrate, which is the YIG thin film. And the out-of-plane saturation field of YIG films is also around 2000 G. These two saturation fields are highly consistent, which supports the anomalous Hall effect case. Second, the magnetization of YIG films does not change significantly below room temperature since the Curie temperature of the YIG films is T_C = 550 K. Moreover, the saturation field of the nonlinear curve does not change with temperature, either, further confirming the origin from the YIG substrate. Third, if the nonlinear curvature is from the two-band Hall mixing, the carrier densities and mobilities of the two mixing channels must be different in different devices. The saturation field cannot be coincidently the same for all the devices. This is contrary to the observation. Thus, the nonlinear curvature should not be a result of the two-band Hall effect mixing. Later, I will show this saturation field does not change at different gate voltages, which is another evidence supporting the anomalous Hall effect case. The calculation of AHE conductivity and related issues will be discussed in the Section 3.5.

3.4.2 AHE Temperature Dependence

Starting from the lowest temperature, 2K, the Hall effect measurement is performed at different temperatures up to 300 K. After the linear background is carefully removed, AHE curves at different temperatures are obtained. Figure 3-17 is a typical set of AHE temperature dependence

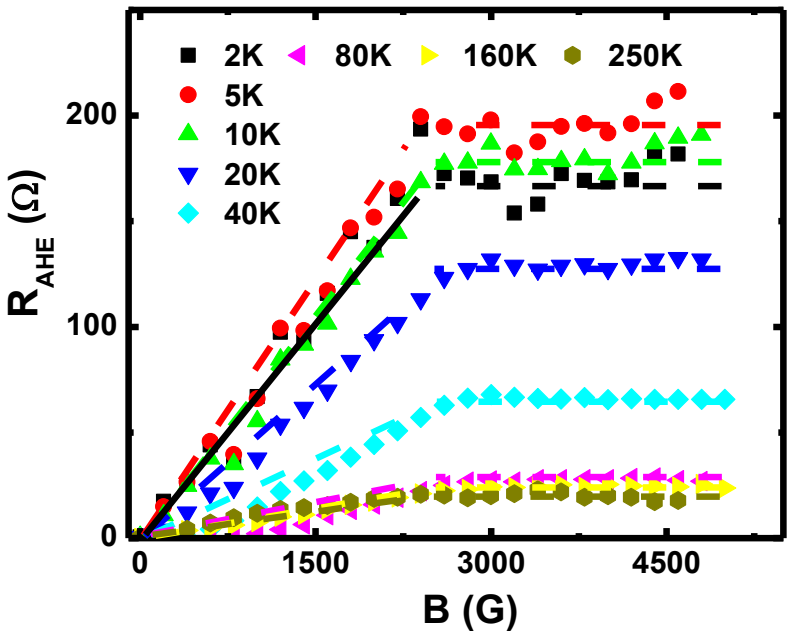

Figure 3-17 AHE at different temperatures

The temperature dependence of AHE in a transferred device is measured within the range of -5000 G to 5000 G in a perpendicular magnetic field. AHE is robust up to 250 K. At 300 K it can hardly be seen. Dashed lines are guides to the eye describing the shape of AHE.

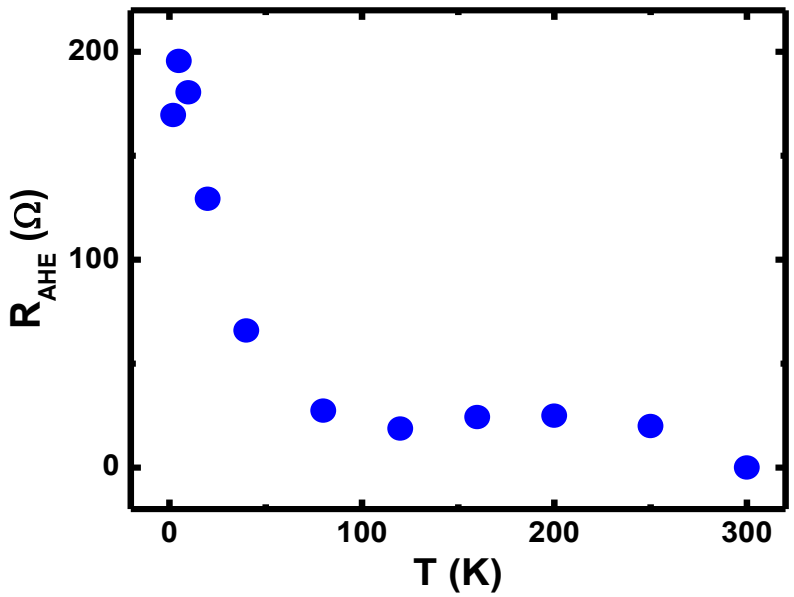

Figure 3-18 AHE resistance temperature dependence.

The AHE resistance at each temperature is extracted from Figure 3-16. R_{AHE} is plotted as a function of T

curves. Then the AHE resistance, which is defined as the resistance in the AHE curve after the saturation field is reached, is extracted from this figure. The AHE resistance R_{AHE} as a function of temperature is plot in Figure 3-18. There is a sharp decrease in R_{AHE} from 2 K to 80 K. Then it stays constant when $T > 80$ K and slowly decreases to zero at 300 K, which defines the Curie temperature, $T_C \sim 300$ K, of the induced magnetization in the transferred graphene device.

This complicated AHE temperature behavior can be explained with two possibilities. It is known that the magnetization in conducting ferromagnets is a function of magnetization and longitudinal resistance. It decreases when either of the parameters decreases, and vice versa. Since the magnetization in YIG is a slow changing function with temperatures below 80K, the steep change in AHE resistance should not originate from the magnetization in YIG film. Then it must result from the change in longitudinal resistance.

Figure 3-19 is a plot of the longitudinal resistance as a function of temperature. Each data point is extracted from the resistance at the Dirac point in the gate dependence curve measured at different temperatures. The black curve is the resistance without external magnetic field, which means the direction of the magnetization in YIG is in-plane. The temperature dependence the longitudinal resistivity is weak without the magnetic field. The blue curve is the resistance with 1 T perpendicular magnetic field, which is already higher than the out-of-plane saturation field of YIG. The magnetic moments should be all aligned to the out-of-plane direction. The temperature dependence of the longitudinal resistivity gets stronger with the 1 T magnetic field. The change in resistance with 1 T perpendicular magnetic field is much larger than that without magnetic field, indicating the influence of the proximity effect in the transferred graphene device. From Figure 3-19, the change in the longitudinal resistance is only 1.5 times from 2 K to 80 K with 1 T perpendicular magnetic field. And it is even smaller without magnetic field. However, from Figure

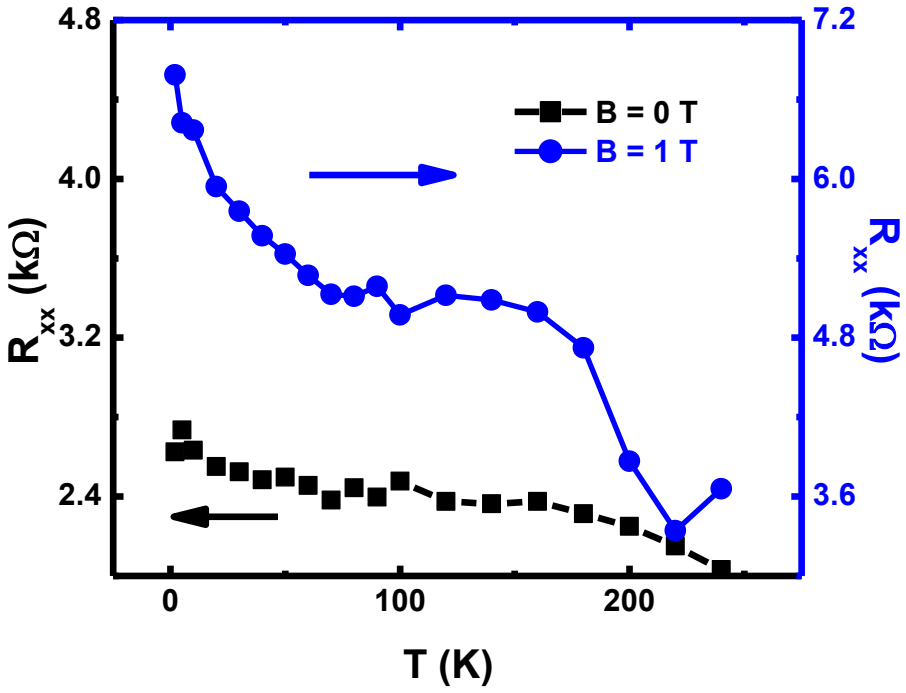

Figure 3-19 Temperature dependence of R_{xx} in a transferred device
The temperature dependence of longitudinal resistance at the Dirac point without magnetic field (black squares) and with 1 T perpendicular magnetic field (blue circles)

3-18, the change in the AHE resistance is about 10 times from 2 K to 80 K. The change in resistance is still too small to be responsible for the dramatic change in the AHE resistance.

Considering that the AHE arises from the proximity effect between graphene and YIG substrate, the AHE should also depend on the coupling strength. The physical contact distance between graphene and YIG can be greatly reduced at low temperatures due to the freeze of atom vibration in the interface region. When temperature increases, the intimate contact between graphene and YIG becomes weaker and weaker, and the effective exchange coupling strength decreases accordingly. It should be pointed out that each device may have different physical contact. And because the exchange coupling greatly depends on the physical contact, there is device-to-device

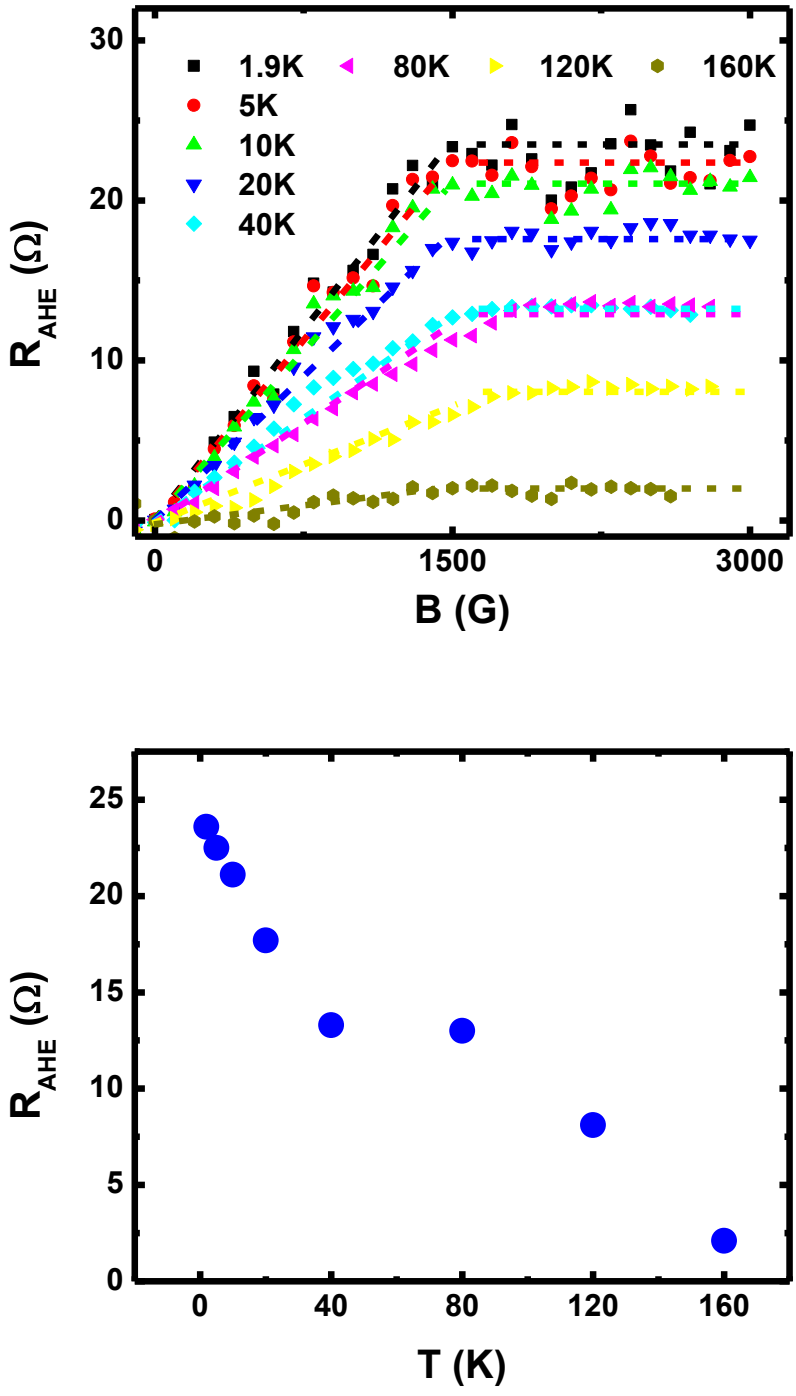

Figure 3-20 AHE temperature dependence in another transferred device
The saturation field of this device is ~ 1700 G. R_{AHE} is only 25 Ω when at 1.9 K. And T_C is only ~160 K.

variation in the Curie temperature T_C and maximum of AHE resistance R_{AHE}. For all the 8 devices studied, the highest T_C is ~ 300 K and maximum R_{AHE} is ~ 200 Ω. Figure 3-20 is the AHE temperature dependence in another device. The maximum R_{AHE} is only ~ 24 Ω. And AHE cannot be observed when temperature is higher than 160 K, which means T_C is only ~ 160 K. This further confirms the statement that the AHE strongly depends on the coupling strength since the coupling strength cannot always has the same level in different devices.

3.4.3 AHE Gate Dependence

With top gate fabricated, the carrier density and type can be tuned in the transferred devices at a fixed temperature, which allows the study of the relationship between R_{AHE} and R_{xx} without affecting the exchange coupling strength and the induced magnetization. For different carrier types, the slopes of the ordinary Hall effect should have different signs. So if the nonlinear curvature comes from a 2-band Hall effect, then the saturation field and even the sign of the nonlinear curve should change when the carrier type changes. But if it is from the induced magnetization, then the AHE sign is not expected to change.

Figure 3-21 is the resistance gate dependence of a transferred device at 20 K. The Dirac point is at V_g = 35V. The carriers are holes at V_{tg} = 60 V while they are electrons at V_{tg} = 0 V and -20V. Although the carrier types are different, there is always nonlinear curvature with the same sign, as is shown in Figure 3-22. Moreover, the saturation fields are the same for the data at these three gate voltages. This is a strong confirmation that the nonlinear curvature is indeed from the AHE which is induced by the YIG film. It is worth to note that among these 3 gate voltages, R_{xx} is the highest one at V_g = 60 V and the corresponding R_{AHE} is also the highest. Those at V_g = 0 V is in the

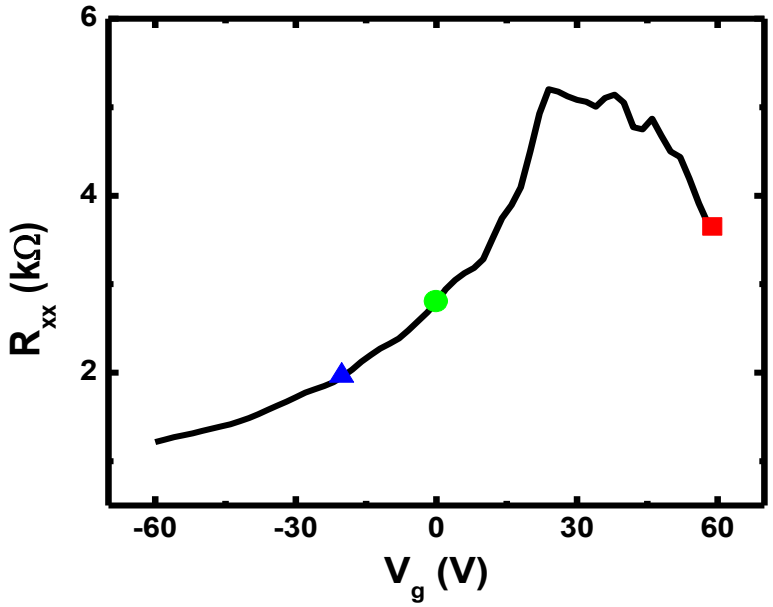

Figure 3-21 Gate dependence of R_{xx} in a transferred device at 20 K

Red square is at V_{tg} = 60 V, green circle is at V_{tg} = 0 V, and blue triangle is at V_{tg} = -20 V. Hall effect measurement is performed at these 3 points and the AHE is extracted, as is shown in Figure 3-21.

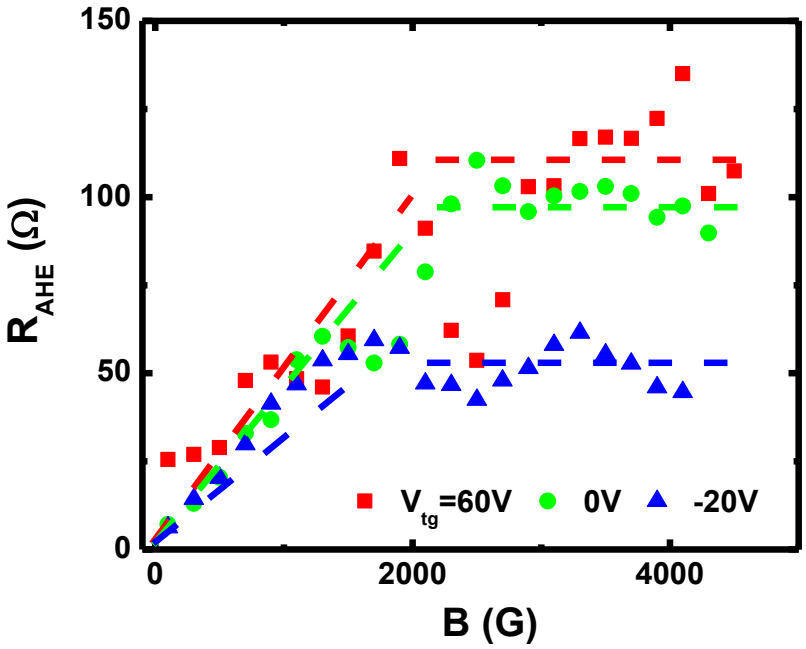

Figure 3-22 AHE at different top gate voltages

Red squares, green circles, and blue triangles are AHE curves at V_{tg} = 60V (electron type), 0V (hole type), and -20 V (hole type). $R_{AHE}(V_{tg}=60V) > R_{AHE}(V_{tg}=0V) > R_{AHE}(V_{tg}=-20V)$, which is the same order as the longitudinal resistances at the corresponding top gate voltages.

middle while V_g = -20 V has the smallest values. It follows the trend that the higher the longitudinal resistance, the higher the AHE resistance.

To further study the relationship between the longitudinal resistance and AHE resistance, another device with fine-tuned top gate voltage is measured at 2 K. The Dirac point in this device is at V_{tg} = -14 V. Start from V_{tg} = -10 V, the Hall effect measurement is taken at different top gate voltages up to V_{tg} = 20 V. The carriers are electrons for all the top gate voltages bigger than -14 V. As the top gate voltage increases, the electron density increases while the longitudinal resistance, R_{xx}, decreases. In the meantime, AHE is monitored. The AHE curves at different top gate voltages are shown in Figure 3-23. a saturation field close to 2200 G is observed in this device. As the top gate voltage is increased, AHE resistance decreases systematically. But the saturation field stays the same. At V_{tg} = 20 V, AHE could be hardly seen. The change of R_{AHE} as a function of temperature is plotted in Figure 3-24. The figure is plotted in a log-log scale in order to extract the exponent of the power-law relationship between R_{AHE} and R_{xx}. The red line is a linear fit on the data, which has a slope of n = 1.9 ± 0.2. This exponent is very close to 2, which means the relationship between R_{AHE} and R_{xx} is $R_{AHE} = AR_{xx}^2$, where A = $\sigma_{AHE.}$ For the traditional conducting ferromagnetic materials, this relationship means that the AHE conductivity does not depend on the scattering rate, which excludes the skew scattering mechanism. Since both the intrinsic and side-jump AHE conductivity does not depend on the scattering rate, our results indicate either an intrinsic or side-jump mechanism. For ferromagnetic metals, whose carrier density is extremely high, by varying the scattering rate, if this relationship holds, then it simply means a constant AHE conductivity, *A*. In general, *A* should depend on the Fermi energy. In metals, the Fermi energy does not change dramatically as the scattering rate is tuned by varying the temperature or other parameters. For a 2D material as graphene, when the gate voltage is tuned, the carrier density and consequently the Fermi energy are tuned. The constant AHE conductivity means that it does not even depend on the

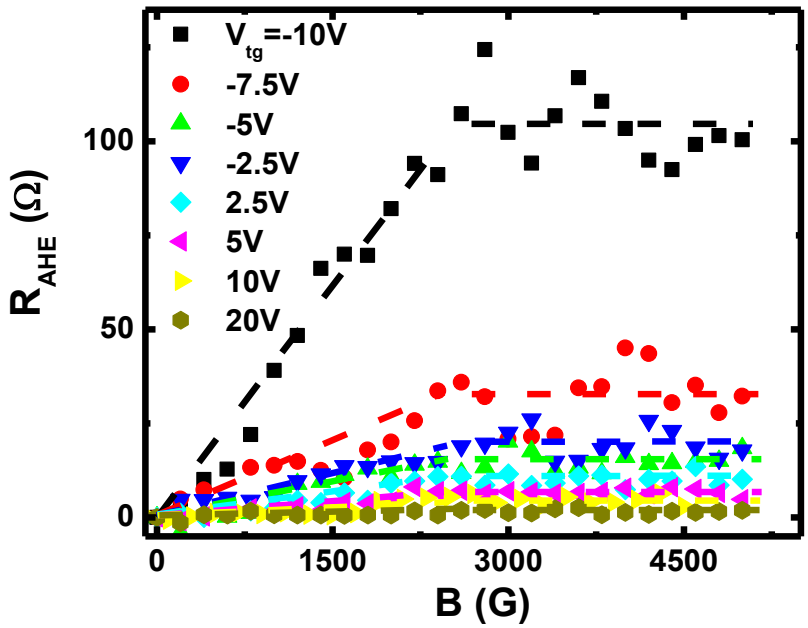

Figure 3-23 AHE at different top gate voltages on the electron side at 2 K

The top gate voltage is gradually increased from V_{tg} = -10 V until V_{tg} = 20 V. The AHE decreases as top gate voltage increases, which can be hardly seen at V_{tg} = 20 V.

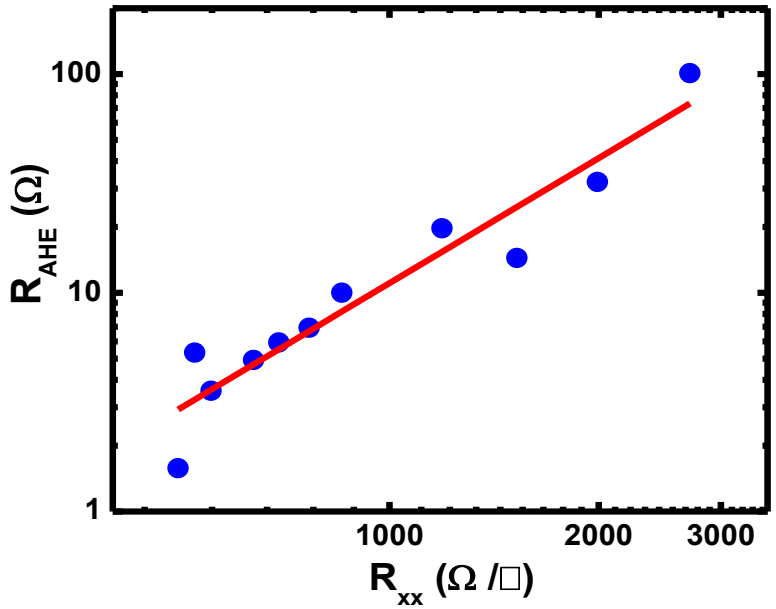

Figure 3-24 R_{AHE} as a function of R_{xx} in log-log plot

R_{AHE} is extracted from Figure 3-22. R_{xx} is measured at the same time when Hall effect is performed. The figure is scaled in a log-log plot.

Fermi energy. Such an observation is difficult to reconcile with the intrinsic mechanism since it should depend on the band structure. More detailed theoretical analysis is needed to elucidate the AHE mechanism in such a system.

No hole side data is taken in this device within the safe top gate range, but the same behavior, which should be the same as the device shown in Figure 3-21 and 3-22, is expected. Another device with top gate is able to show Dirac point at the high positive gate voltage, allowing the study of the relationship between R_{AHE} and R_{xx} on the hole side. The AHE curves at different gate voltages on the hole side are present in Figure 3-25. The Dirac point is at V_{tg} = 55 V in this device. Starting from V_{tg} = 46 V, the top gate voltage is systematically decreased to V_{tg} = 20 V. The longitudinal resistance decreases accordingly and the AHE resistance follows the same trend. R_{AHE} can be extracted from Figure 3-25 and its relationship with respect to R_{xx} is plotted in Figure 3-26 in a log-log scale. In Figure 3-26, the red line is a linear fit on the data and the slope is 1.9 $\pm$0.3, which is

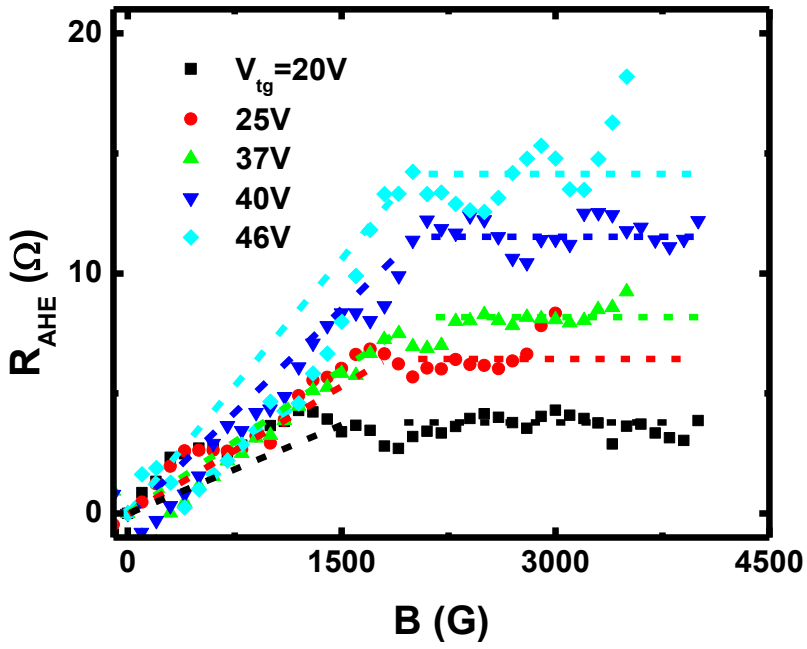

Figure 3-25 AHE at different top gate voltages on the hole side at 2 K
The top gate voltage is gradually increased from V_{tg} = 20 V until V_{tg} = 46 V.

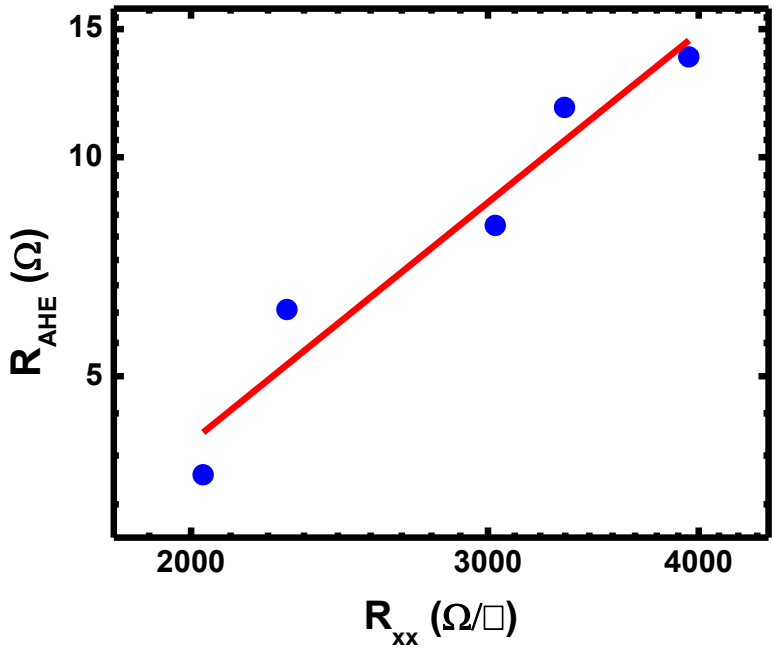

Figure 3-26 R_{AHE} as a function of R_{xx} in log-log plot
AHE resistance is extracted from Figure 3-24. Longitudinal resistance is measured at the same time when performing Hall effect measurement.

almost the same as the value obtained in Figure 3-24 in the previous device on the electron side. This means exponent of the power-law scaling in R_{AHE} with respect to R_{xx} is also very close to 2. Both of this device and the previous device have the same consistency with the first device shown in Figure 3-21 and 3-22. Regardless the carrier type, the AHE always has the same sign and changes with the longitudial resistivity, forming a power-law relationship with respect to the longitudian resistivity with an exponent of 2. More discussion will be present in Section 3.5.

3.5 Discussion

The intrinsic spin-orbit coupling in graphene is very weak due to its low atomic number[80], which is estimated to be ~10 μeV. But large enhancement in the spin-orbit coupling can be realized

when graphene is put on to certain substrates[82,85] or subjected to hydrogenation[74], which is a critical condition to realize the QAHE in the transferred graphene device. The observation of AHE in the transferred graphene devices up to 300 K indicates strong spin-orbit coupling in the device and marks the Curie temperature in the transferred graphene device.

With the highest R_{AHE} and the corresponding ρ_{xx}, one can calculate the AHE conductivity σ_{AHE} with equation $\sigma_{AHE} = \frac{R_{AHE}}{\rho_{xx}^2 + R_{AHE}^2} = 0.09\left(\frac{2e^2}{h}\right)$, which is about one order smaller than the quantum conductance, $2e^2/h$. The QAHE has not been realized yet. To achieve the quantum conductance, the Fermi level should be firstly tuned into the gap opened by the magnetic exchange field and the strong spin-orbit coupling. This gap size is mainly determined by the smaller of these two factors. The highest T_C observed is ~ 300 K, meaning the exchange coupling strength should be no less than 25 meV. The observation of AHE but not QAHE may indicate that the spin-orbit coupling is still not strong enough so that the opened gap is still small. When the Fermi level is in the gap, disorder smear out the small gap so that only AHE can be observed.

In graphene, there is a relationship[72] between σ_{xx} and n_{2D},

$$\sigma_{xx} = 2\frac{e^2}{h}\frac{\pi v_F^2}{u_0^2} n_{2D}.$$

From the gate voltage dependence, one can obtain the slope of the above equation is, $slope = 2\frac{e^2}{h}\frac{\pi v_F^2}{u_0^2} = 1.34 \times 10^{-19} m^2/\Omega$. For the relaxation time τ_k in graphene, it has a dependence on carrier density[72],

$$\tau_k = \frac{v_F}{u_0^2} k = \frac{v_F}{u_0^2}\sqrt{\pi n}.$$

From the slope just calculated, $\frac{v_F}{u_0^2}$ can be obtained, $\frac{v_F}{u_0^2} = \frac{slope}{2\frac{e^2}{h}\pi v_F} = 5.52\times10^{-22} m\cdot s$. Then,

$\tau_k = \frac{v_F}{u_0^2}\sqrt{\pi n} = 9.78\times10^{-22}\sqrt{n}(m\cdot s)$. From Ref 86[86], one have

$$\sigma_{\min} = \frac{20e^2}{h}\frac{n^*}{n_{imp}} \Rightarrow n_{imp} = \frac{20e^2}{h}\frac{n^*}{\sigma_{\min}}.$$

σ_{min} can be determined from the gate voltage dependence, σ_{min} = 3.15 ×10^{-4} S, then n_{imp} = 2.45n*, where n* is the width of σ_{xx} plateau. The V_g range for σ_{xx} plateau is ~ 3 V. Then $n^* = C_S V_g/e$ = 1.38 ×10^{15} m^{-2}, where C_S = 7.36 ×10^{-5} F/m^2, which is calculated from the quantum Hall effect. So n_{imp} = 3.38 ×10^{15} m^{-2}. Then τ_k =5.69 ×10^{-14} s. And the broadening energy from disorder is

$$\frac{\hbar}{\tau_k} = 1.85\times10^{-21} J = 11.6 meV.$$

This disorder broadening energy is only half of the exchange coupling strength. One can infer that the Rashba spin-orbit coupling is less than $\frac{1}{2}\times 11.6\ meV = 5.8\ meV$ so that the disorder smear out the gap and no QAHE is observed.

For traditional conducting ferromagnetic materials, once the relationship between R_{AHE} and $R_{xx,}$ $R_{AHE}\sim R_{xx}^{a}$, is figured out, the mechanism can readily be known. The intrinsic origin of AHE will give a = 2, whereas the skew scattering from impurities gives a = 1. When a = 2, there is another possibility that it could be from the side jump effect which is also an extrinsic mechanism. While the relationship is between R_{AHE} and R_{xx} being extracted, the relaxation time is usually tuned. However, the change in carrier density or Fermi level is impossible due to the extreme high carrier density in the traditional conducting ferromagnetic materials. But graphene is a completely new system compared to the conducting ferromagnetic materials. While the relaxation time is tuned, the carrier density and Fermi level is also changed, the AHE mechanism is much more complex in this

system. However, this opens a new route to study the ferromagnetism in a 2D system such as graphene.

The low-energy effective Hamiltonian for graphene on YIG in the vicinity of Dirac point can be written as

$$\mathcal{H}_{\tau_z} = v\left(\tau_z\sigma_x p_x + \sigma_y p_y\right) + \frac{\lambda_R}{2}\left(\tau_z\sigma_x s_y - \sigma_y s_x\right) + \Delta s_z.$$

where $\tau_z = \pm$ indicating the **K** and **K'** valley respectively, σ and s are the Pauli matrices acting on the sublattice and spin degree of freedom respectively, v is graphene's Fermi velocity, λ_R is Rashba spin-orbit coupling, and Δ is the proximity-induced spin splitting due to the YIG substrate. The Hamiltonian acts on the wavefunction $\psi_\pm^\dagger = (\psi_{A,\uparrow,\pm}^\dagger, \psi_{B,\uparrow,\pm}^\dagger, \psi_{A,\downarrow,\pm}^\dagger, \psi_{B,\downarrow\pm}^\dagger)$, identified by the corresponding valley index, $\tau_z = \pm$. After diagonalizing the Hamiltonian for one valley, **K**, the energy dispersion can be obtained,

$$E_\pm^2 = v^2p^2 + \Delta^2 + \frac{\lambda_R^2}{2} \pm \frac{1}{2}\sqrt{4v^2p^2(4\Delta^2 + \lambda_R^2) + \lambda_R^4},$$

With the Fermi velocity given by $v = (3/2)ta$ = 596.4 meV nm, where t = 2.8 eV is the nearest neighbor hopping strength and a = 0.142 nm is the lattice constant in graphene, the energy dispersion with respect to the wavevector p can be plotted, Figure 3-27. The magnetic exchange strength is Δ = 25 meV, which is estimated from the AHE temperature dependence. The exchange

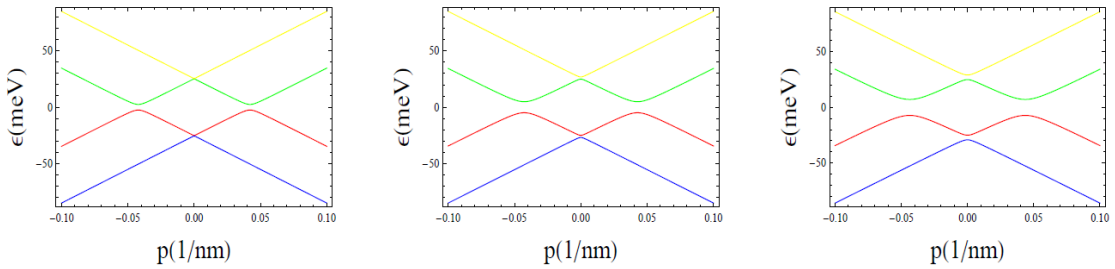

Figure 3-27 Energy dispersion in **K** valley with Rashba coupling
From left to right, the Rashba spin-orbit coupling is 5, 10, 15 meV respectively.

field leads to the spin splitting in the band structure. And the Rashba spin-orbit coupling avoids the band crossings. The **K'** valley has the same structure as the **K** valley.

For convenience, we denote the four bands by the index α = 1, 2, 3, 4 (blue, red, green, yellow, respectively in Figure 3-27), $\epsilon_1 = -E_-, \epsilon_2 = -E_+, \epsilon_3 = E_-, \epsilon_4 = E_+$. With p = 0, the energy gaps between 1 and 2, 3 and 4 can be calculated,

$$|\epsilon_2(p=0) - \epsilon_1(p=0)| = |\epsilon_4(p=0) - \epsilon_3(p=0)| = \sqrt{\Delta^2 + \lambda_R^2} - \Delta.$$

And the energy gap between 2 and 3 is

$$\Delta_g = \left|\epsilon_{3,min} - \epsilon_{2,max}\right| = 2\epsilon_{3,min} = \frac{2\Delta\lambda_R}{\sqrt{4\Delta^2+\lambda_R^2}}, \text{ with } p = \pm\frac{\sqrt{2}\Delta}{v}\sqrt{\frac{2\Delta^2+\lambda_R^2}{4\Delta^2+\lambda_R^2}}.$$

From this expression, one can infer that $\Delta_g < 2min(\Delta, \lambda_R)$, which is that the energy gap is always smaller than twice of the minimum value of the magnetic coupling and the Rashba spin-orbit coupling.

As is discussed in the beginning of this chapter, the intrinsic contribution to the AHE can be determined by integrating the Berry curvature over all the occupied states,

$$\sigma_{AHE}^{int} = \frac{e^2}{\hbar}\sum_\alpha \int_{BZ} \frac{d^2k}{(2\pi)^2} n_F(E_\alpha(\boldsymbol{k}))\Omega_\alpha(\boldsymbol{k}),$$

where the integral is on the Brillion zone, α is the band index, n_F(x) is the Fermi-Dirac distribution, E_α(**k**) is the energy eigenstate, Ω_α(**k**) is the Berry curvature of the α^{th} band., which is

$$\Omega_\alpha(\boldsymbol{k}) = -Im\left[\epsilon_{ij}\left\langle\frac{\partial u_\alpha(\boldsymbol{k})}{\partial k_i}\middle|\frac{\partial u_\alpha(\boldsymbol{k})}{\partial k_j}\right\rangle\right],$$

where ϵ_{ij} is anti-symmetric tensor, u_α(**k**) is the α^{th} band eigenstate. With inversion symmetry, Ω_α(**k**) = Ω_α(-**k**). With time-reversal symmetry, Ω_α(**k**) = - Ω_α(-**k**). Due to the presence of YIG substrate and magnetic exchange coupling, the time-reversal symmetry is broken. So the Berry curvature can be non-zero. For the **K** valley,

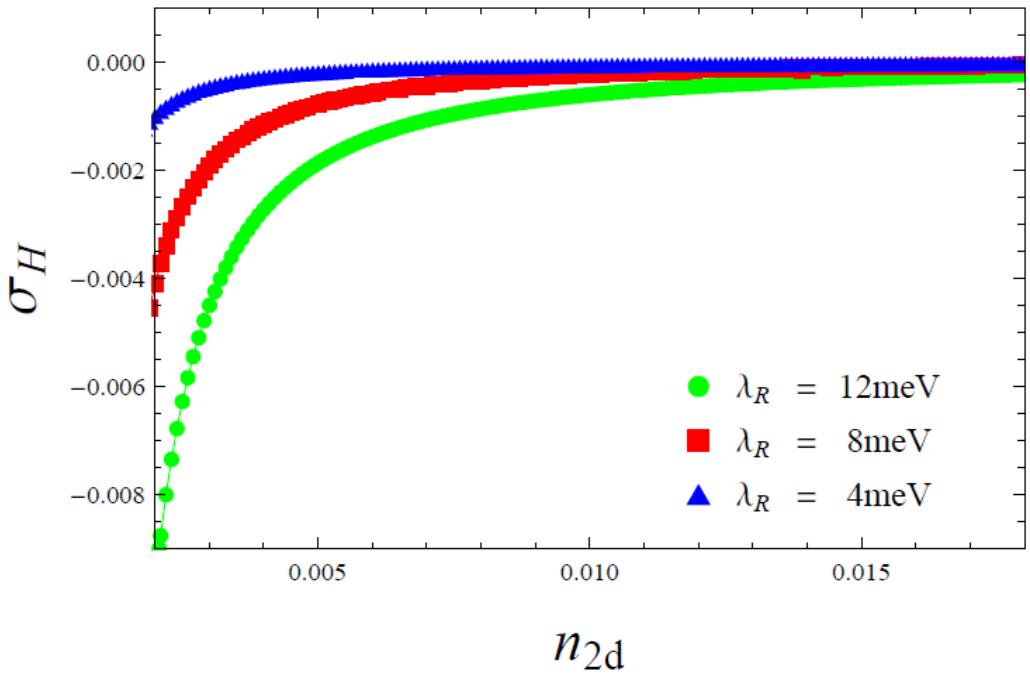

Figure 3-28 Intrinsic AHE conductivity as a function of n_{2D}
The exchange field is assumed to be 25 meV which is estimated from the AHE temperature dependence. The Rashba spin-orbit coupling is set as 4 (blue triangles), 8 (red squares), 12 meV (green circles). The unit for AHE conductivity is e^2/h.

$$\Omega_\alpha(\boldsymbol{k}) = Im\sum_{\beta\neq\alpha}\left[\epsilon_{ij}\frac{\langle u_\alpha|\partial\mathcal{H}(\boldsymbol{k})/\partial k_i|u_\beta\rangle\langle u_\beta|\partial\mathcal{H}(\boldsymbol{k})/\partial k_j|u_\alpha\rangle}{(\epsilon_\beta-\epsilon_\alpha)^2}\right],$$

where α, β = 1, 2, 3, 4. When the Fermi level is in the gap, the σ_{AHE}^{int} is quantized.

With the equation derived for σ_{AHE} above, the intrinsic contribution of σ_{AHE} in the transferred graphene device can be calculated, as is shown in Figure 2-28. The exchange field is estimated from the AHE temperature dependence, Δ = 25 meV. The Rashba spin-orbit coupling λ_R = 4, 8, 12 meV for the blue, red and green curves, respectively. The calculated intrinsic σ_{AHE} is at least one order smaller in magnitude than the measured value (0.09($2e^2/h$)). Therefore, the AHE in the transferred graphene has a more likely extrinsic mechanism, such as side jump. As the Dirac point is approached, the carrier density is greatly reduced, the charged impurity screening in graphene

turns to be weak. Hence, the extrinsic mechanism gets enhanced. This may be the reason why the intrinsic mechanism takes up only a small portion in the AHE. It is worth to point out that the Fermi level manipulation with gating in this ferromagnetic graphene opens a new approach allowing the study of the relationship between the Fermi energy and the AHE conductance, which is impossible in traditional conducting ferromagnetic materials. It may lead to a different empirical power-law relation which may further elucidate the physical origin of the AHE.

The transfer process of the entire device is very successful without affecting graphene's quality and mobility. The AHE is observed in the transferred graphene devices on YIG thin films, revealing the achievement of induced ferromagnetism in graphene. The highest Currie temperature T_C is ~ 300 K, indicating a strong magnetic proximity effect at the interface between graphene and YIG thin film. And the presence of AHE in graphene itself is an evidence of strong Rashba spin-orbit coupling in graphene. More effort can be made to have a device as clean as possible so that the Coulomb scattering and broadening energy from disorder can be greatly reduced. And further work can be carried out to achieve strong spin-orbit coupling and high quality device with less impurities and disorder.

3.6 Transition Metal Dichalcogenides

3.6.1 Device Characterization

In this section, the transition metal dichalcogenides are discussed. Here, the transition metal dichalcogenides are referred to the layered structure materials, MoS_2, $MoSe_2$, WS_2, and WSe_2. Since they all have similar properties, only MoS_2 will be discussed in this chapter.

MoS_2 nanoflakes are mechanically exfoliated on to SiO_2/Si substrates with the same method of the scotch-tape assisted graphene exfoliation. Under optical microscope, on the 290-nm thick SiO_2/Si substrate, the color of single-layer MoS_2 is blue to purple, similar to the color of bilayer or trilayer graphene but darker than that of single-layer graphene. Figure 3-29 is a typical optical microscopy images of the mechanically exfoliated MoS_2 nanoflakes. The nanoflake in the middle of the image has two parts: the left part is single-layer MoS_2 while the right part is bilayer. Around

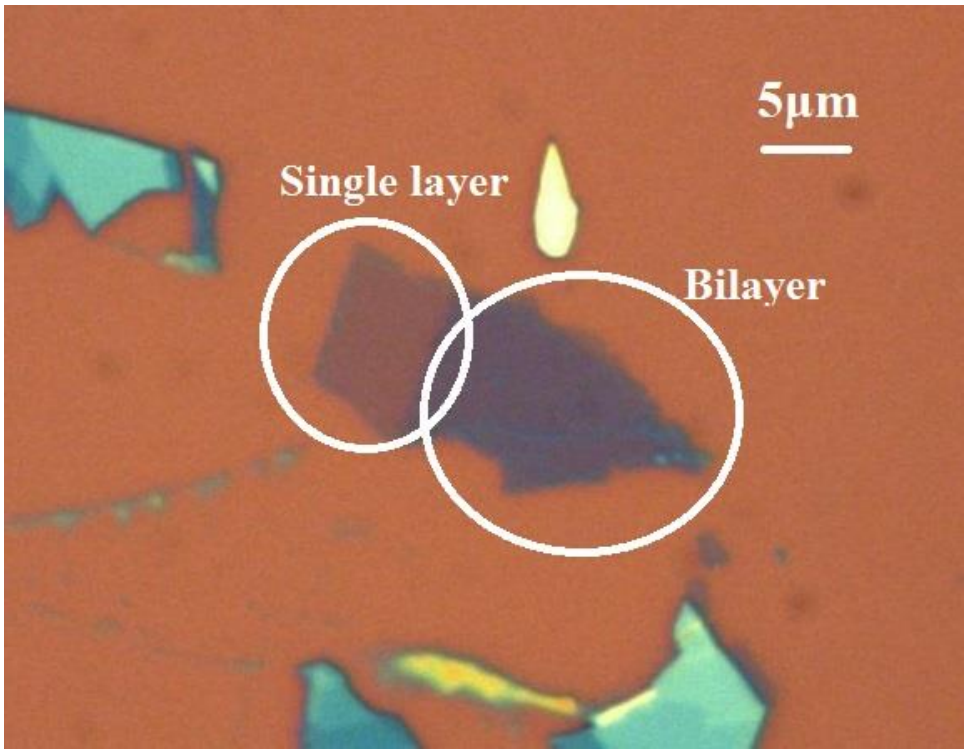

Figure 3-29 MoS_2 optical microscope image

this flake, there are several multilayer MoS_2 nanoflakes. The color contrast is quite clear for atomically thin MoS_2 nanoflakes[87-90]. This can be further confirmed by Raman spectroscopy and atomic force microscopy, which will be discussed later.

The thickness of MoS_2 nanoflakes is firstly characterized by optical Raman spectroscopy[87]. Room temperature Raman spectroscopy is performed with a 532 nm laser on MoS_2 nanoflakes. The typical Raman spectra of MoS_2 with different thickness are shown in Figure 3-30. Between the range of 360 cm^{-1} and 440 cm^{-1}, two characteristic peaks of MoS_2 can be identified, the E_{2g}^1 peak (~ 386 cm^{-1} for single-layer MoS_2) and A_{1g} peak (~ 405 cm^{-1} for single-layer MoS_2). Although there are always two characteristic peaks of MoS_2 with different thickness, the peak positions are slightly different. Table 3-1 is a list of the peaks positions of MoS_2 with different thicknesses. For thicker MoS_2, The position of the E_{2g}^1 tends to have a smaller value while the position of the A_{1g} peak tends to be at a higher Raman shift. For bulk MoS_2, the positions of the the E_{2g}^1 peak and A_{1g} peak are 384 cm^{-1} and 409 cm^{-1}, respectively. Another important feature related to the thickness is the difference between the Raman shifts of the two peak positions[87]. The separation of the two peaks grows as the thickness of MoS_2 flakes increases from 19 cm^{-1} in single-layer MoS_2 to 25 cm^{-1} in bulk MoS_2. The changes of the Raman shifts of the two peaks in MoS_2 with different thicknesses is attributed to the Coulomb interactions and possible stacking-induced changes of the intralayer bonding, as well as the van der Waals forces between layers.

Table 3 Raman shifts of MoS_2 flakes

	Raman Shift		
MoS_2 thickness	**E_{2g}^1 (cm^{-1})**	**A_{1g} (cm^{-1})**	**Difference (cm^{-1})**
Single-layer	386	405	19
Bilayer	385	406	21
Bulk	384	409	25

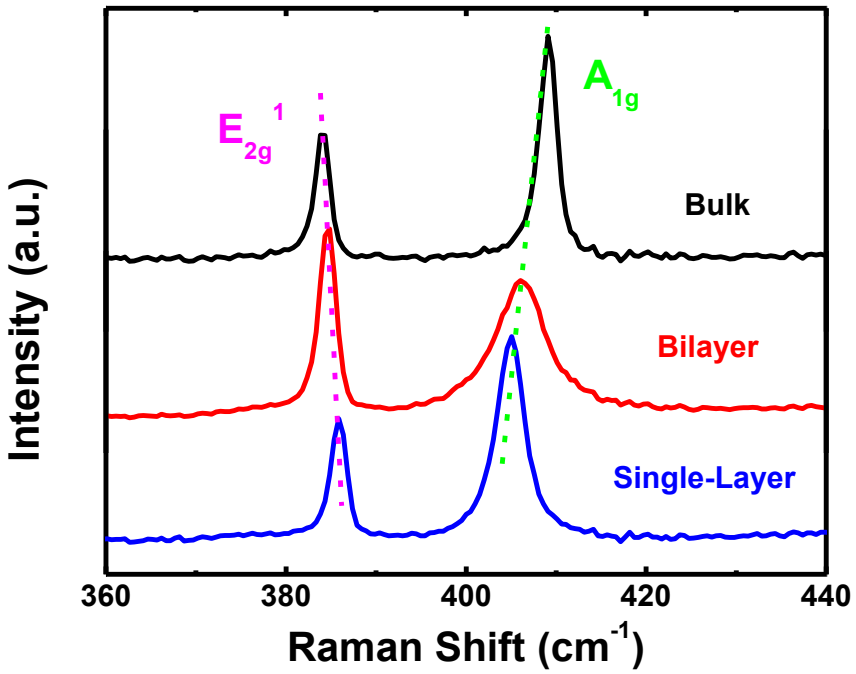

Figure 3-30 MoS_2 Raman spectra

Atomic force microscopy is performed to further confirm the thickness of MoS_2 nanoflakes substantiate the statement made in previous paragraphs. It can also provide the topographic information of the nanoflakes so as to check the quality of MoS_2 nanoflakes. Figure 3-31**a** is the optical image of a typical MoS_2 flake. Its left part is single-layer while the right part is multi-layer. Figure 3-31**b** and **d** are the AFM topographic images of this MoS_2 flake. From the AFM images, the flake is quite clean on both the single-layer part and multilayer part. Nevertheless, there are thick "islands" around the flake which are believed to be scotch tape residual. Figure 3-31**c** and **e** are the height profiles across the lines marked on Figure 3-31**b** and **d**, respectively. In Figure 3-31**c**, the height different between the two adjacent red arrows is only 0.78 nm, which is very close to the expected thickness (0.65 nm) of single-layer MoS_2 and smaller than the bilayer thickness. It

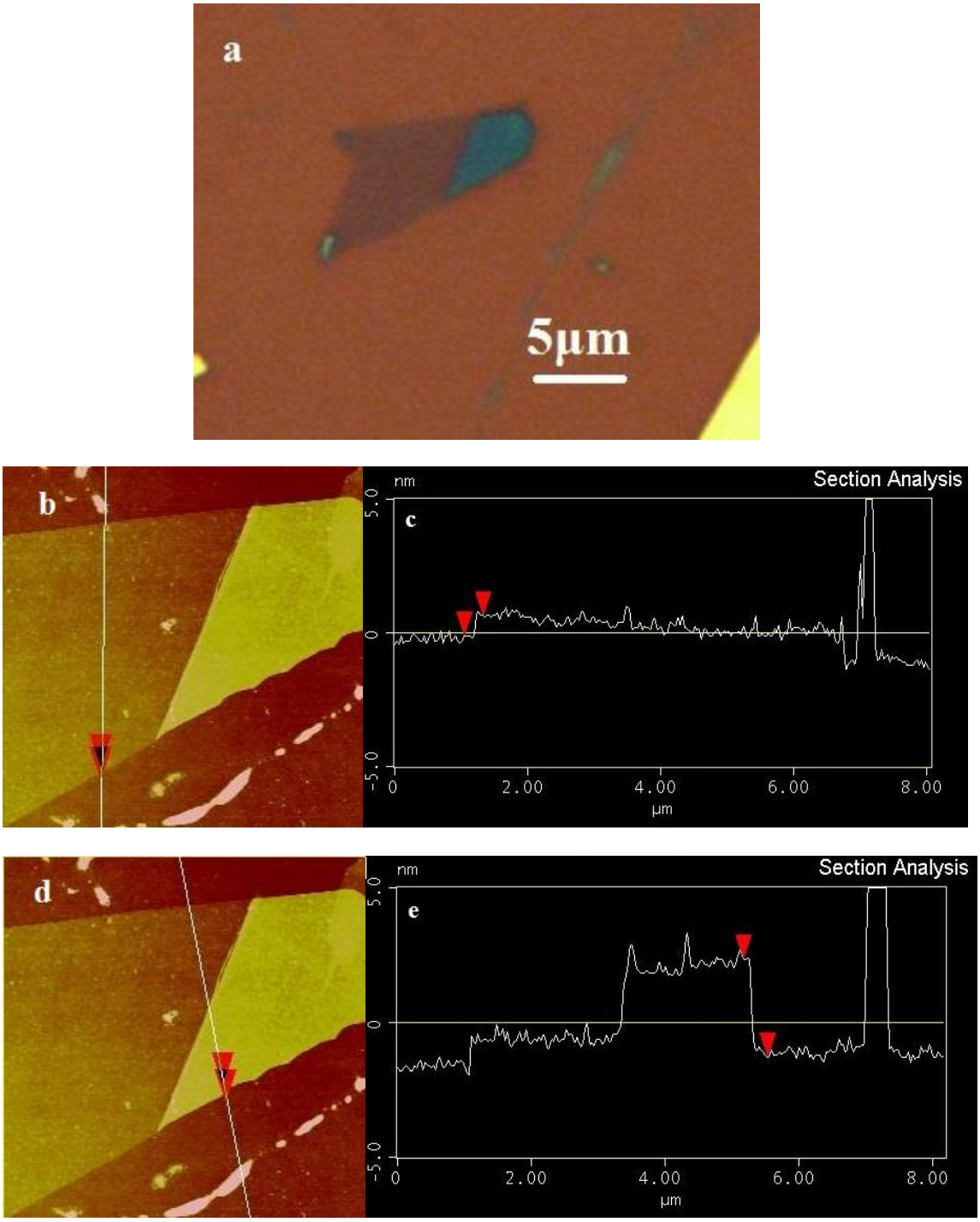

Figure 3-31 AFM on MoS_2

a, Optical microscope image of MoS2 nanoflake; **b.** and **c.** AFM topographic image of the MoS2 flake shown in **a**; **c**. and **e.** thickness profiles of the lines marked in **a**. and **c.**

has to be a single-layer MoS_2. The thickness of the multilayer part is 3.62 nm, which corresponds to five layers of MoS_2.

Sometimes, scotch tape residual can be seen even on top of the MoS_2 flakes under atomic force microscope, which could result in an inaccuracy in the flake's thickness measurement. And this could also aggravate the contact problem between the flake and contact electrodes. Annealing at a relatively high temperature can be performed to reduce and even remove the scotch tape residual and thus improve the contacts.

3.6.2 Device Fabrication

MoS_2 nanodevices are firstly fabricated with MMA and PMMA as the electron beam lithography resist which is describe in section 3.2.1. It is known that there is always Schottky's barrier between a metal electrode and a semiconductor due to the mismatch in work functions. Moreover, there is always resist residual left on the flake no matter how well it is developed although a little overexposure is performed. Hence, Contact problem becomes quite essential in MoS_2 devices. To have a cleaner surface, the lift-off resist (LOR) is employed instead of MMA, which is believed to have less residual after develop.

A layer of LOR-3B is spin-coated at a speed of 3600 rpm for 45 sec with a ramping rate of 10000 rpm/s. The wafer is baked on a hot plate at 180 ℃ for 5 min. Subsequently, a layer of PMMA is spin-coated at speed of 3600 rpm for 45 sec with a ramping rate of 10000 rpm/s. And it is baked on a hot plate at 180 ℃ for 5 min. After electron beam lithography, the PMMA resist is developed in in a solution consisting IPA and MIBK with the ratio of 3:1 for 65 s. Since LOR is not sensitive to electron beams. There is still the LOR layer covering the entire substrate, but with the PMMA layer patterned. Then the LOR is developed in an MF-319 solution afterwards. Usually 2 seconds

are long enough to develop LOR resist. However, in order to get clean surface and good contact, another half to one second developing time is added. But this can only be done under the premise of the good separation of electrode patterns.

3.6.3 Electrical Transport Properties

3.6.3.1 Electrical transport properties on SiO_2/Si

The electrical transport properties of MoS_2 nanodevices are tested with Keithley 2400 as the bias source and Keithley 2000 as the ammeter and voltmeter. Usually, Lock-in amplifiers are used for the electrical transport measurement due to the high signal/noise level. However, MoS_2 nanodevices have very high resistance which is comparable to the internal resistance of a Lock-in amplifiers. The output source voltage will be greatly affected. Moreover, due to the Schottky's barrier and high contact resistance, the imaginary part of detected signal in the Lock-in amplifier is big, which will affect the extraction of the actual signals. So the use of Lock-in amplifiers are no longer applicable in MoS_2 nanodevices.

The current-voltage characteristic curves are tested to check the contact between MoS_2 and metal electrodes. And a back gate is applied through the SiO_2 dielectric layer to tune the Fermi level in the device. At high positive gate voltages, a relatively linear current-voltage characteristic curve is obtained after the MMA resist is replaced with LOR, as is shown in Figure 3-32, which confirms the fact that there is a cleaner surface after LOR is employed. The source-drain current is I_{ds} = 0.84 μA at V_g = 60 V with the application of a source-drain voltage V_{ds} = 1 V, which corresponds to a 2-termianl resistance R_{2T} = 1.2 MΩ. The 4-terminal voltage, V_{4T} are monitored simultaneously. R_{4T} can be calculated by dividing V_{4T} with I_{ds}. Then one can have $R_{4T} = V_{4T}/I_{ds}$ = 0.4 MΩ at V_g = 60 V. When the gate voltage is decreased to V_g = 0 V, I_{ds} = 0.105 μA and V_{4T} = 0.326 V. Then R_{2T} = 9.5

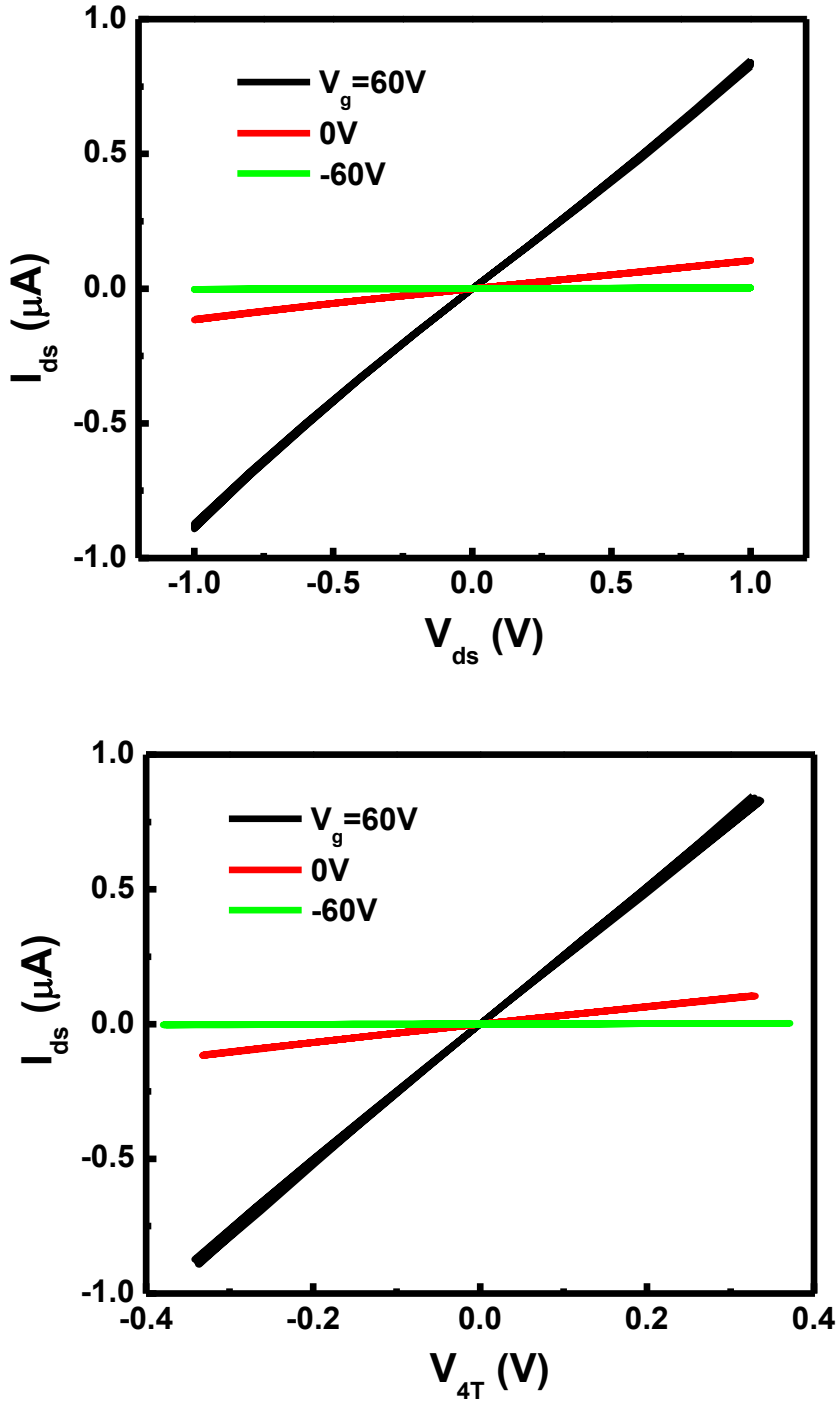

Figure 3-32 Current-Voltage curve of a single-layer MoS_2 device
Upper figure is the current-voltage curve between the source-drain electrondes. In the lower figure, the source-drain voltage, V_{ds}, is replaced by the 4-terminal voltage, V_{4T}.

MΩ and R_{4T} = 3.1 MΩ. When the gate voltage is further decreased to V_g = -60 V, the source-drain current decreases accordingly to I_{ds} = 2.58 nA while V_{4T} remains almost unchanged V_{4T} = 0.366 V. Then one have R_{2T} = 388 MΩ and R_{4T} = 142 MΩ at V_g = -60 V.

For all the gate voltages, if comparing R_{2T} with R_{4T}, R_{2T} is always about three times as resistive as R_{4T}. When considering the aspect ratio difference between R_{2T} and R_{4T}, the corresponding resistivities are almost the same, revealing a small or comparable contact resistance with respect to the device resistance.

In order to have the Fermi level precisely adjusted to the maximum of the valence band, a back gate is applied to the device through the SiO_2/Si substrate. At room temperature, a constant bias voltage V_{ds} = 1 V is applied, and both I_{ds} and V_{4T} are monitored. Figure 3-33**a** is the gate dependence of I_{ds}. The source-drain current at V_g = 60 V is I_{ds} = 1.76 μA, the corresponding R_{2T} = 568 kΩ. As V_g is decreased, the I_{ds} decreases subsequently, indicating the majority carriers are electrons and the Fermi level is in the conduction band. When the gate voltage is decreased to V_g = -60V, I_{ds} then decreases to I_{ds} = 1.13 nA and R_{2T} = 885 MΩ, which can be explained that the Fermi level just gets into the bandgap and no free carriers are present in the device. The change in I_{ds} or R_{2T} covers more than three orders in magnitude. When V_g is further decreased, I_{ds} decreases accordingly. However, due to the influence of noise and the limit of meters, the current measured will be with of less accuracy. Figure 3-33**b** is the gate voltage dependence of R_{4T}, which has the same trend as the R_{2T} but is only 1/3 in magnitude as big as R_{2T}.

Taking the derivative of I_{ds} or R_{4T} with respect to V_{ds}, then the field-effect mobility can be extracted. Since there is almost no difference in resistivity or conductivity for R_{2T} and R_{4T}, only the mobility extracted from R_{2T}, which is the gate dependence of I_{ds}, will be discussed. The field-effect mobility is calculated in the same way as is discussed in Section 2.3. With the application

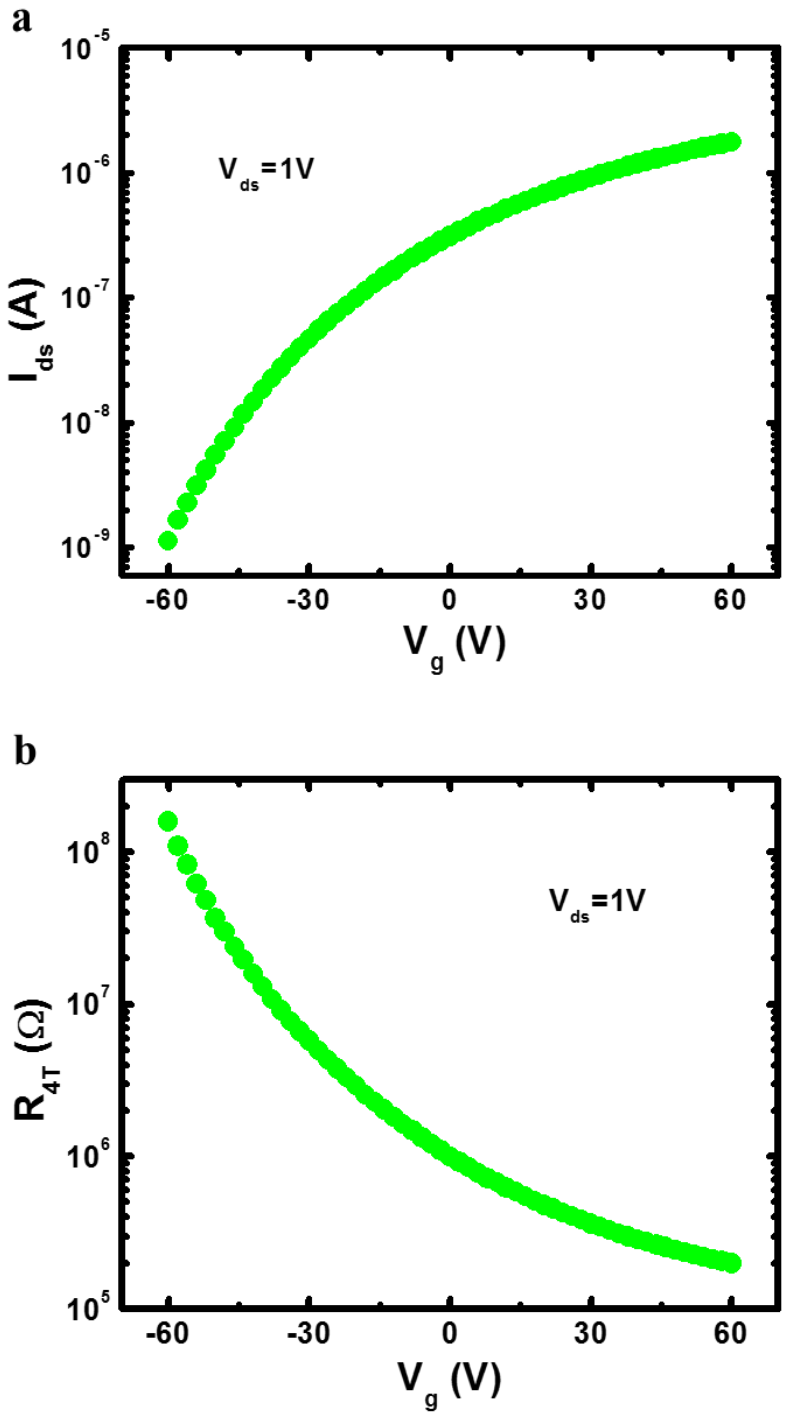

Figure 3-33 Gate dependence of a single-layer MoS_2 device
Upper Figure, **a**, is the gate dependence of the source-drain current I_{ds}. Lower Figure, **b**, is the gate dependence of the 4-terminal resistance R_{4T}.

of 1V

source-drain voltage, the mobility is ~ 7 $cm^2/V{\cdot}s$ at V_g = 60V, which is a typical value of single-layer MoS_2 devices on a substrate[89,91,92]. The mobility decreases as V_g is decreased, which can be explained with the fact that the Fermi level is approaching the band gap as V_g is decreased, resulting in the decrease in mobility.

The Fermi level cannot be tuned close to the valence band yet, although a change over 10^3 has been achieved with the applying of a back gate through SiO_2 dielectric layer. A new material with high dielectric constant needs to be explored in order to widely tune the Fermi level.

3.6.3.2 Electrical Transport Properties on Strontium Titanate (STO)

In order to widely tune the Fermi level in MoS_2 devices, a new material with high dielectric constant needs to be explored. The strontium titanate (STO) has an extreme high dielectric constant at room temperature, which is near 300. At low temperature, its dielectric can be even higher. Moreover, high dielectric constant substrate is expected to greatly suppress the Coulomb scattering in extremely thin device so that the device's performance could be greatly enhanced, for example the improvement in carrier's mobility[93]. The mobility enhancement is observed with single-layer MoS_2 device with a HfO_2 top gate dielectric material[89]. The mobility enhancement in MoS_2 devices is expected with the application of STO substrate.

Graphene can be identified on SiO_2 with a certain thickness atop Si substrate[1,94-96]. The same principle applies to single-layer TMD flakes. Nonetheless, the identification of MoS_2 (or WS_2, WSe_2) on other substrates is of great difficulty. Moreover, since STO substrate is about 200 μm thick and is insulating, the electron beam lithography can hardly be performed during the fabrication process. Then the same device transfer technique, described in Section 3.2.2, is employed to transfer MoS_2 devices to STO substrates. After transfer, the device is annealed in

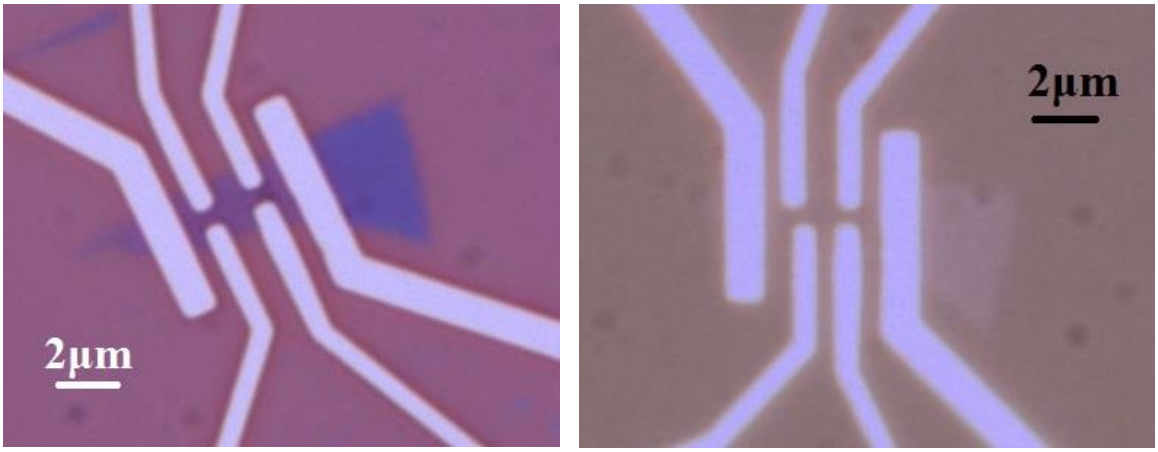

Figure 3-34 Optical images of the same MoS_2 device before and after transfer
Left figure is a single-layer MoS_2 device fabricated on SiO_2/Si substrate. Right figure is the same MoS2 device after transferred to STO substrate.

vacuum for 2 hours at about 400 ℃. Single-layer MoS_2 device becomes nearly invisible after transferred to STO substrate. Nevertheless, the situation is different for multi-layer MoS_2. In Figure 3-34, which are the same device before and after transfer, the location of the single-layer part can hardly be told while it is quite easy to recognize the multi-layer part. The identification of the multi-layer MoS_2 part and the contact electrodes implies the success of the transfer process.

After transfer, the device is characterized electrically at room temperature. Figure 3-35 is a typical current-voltage characteristic curve for the device on STO substrate. Since the STO substrate is very thick, ~200 μm, extremely high gate voltage can be applied to through the STO dielectric without dielectric breakdown. Black curve is the current-voltage curve at V_g = 0 V and red curve is the one at V_g = 200 V. A source-drain voltage of V_{ds} = 10V is applied. At V_g = 200 V, I_{ds} = 1.30 μA. Then R_{2T} = 7.69 MΩ. At V_g = 0 V, I_{ds} is already very low, which is ~ 145 nA with V_{ds} = 10V. The corresponding R_{2T} is 69 MΩ. When the gate voltage is further decreased, I_{ds} stays almost unchanged and at a very small value, indicating the limit of the ammeter. The current-voltage curves at both gate voltages (0 V and 200 V) show nonlinear behaviors indicating a nonohmic contact between the device and electrodes. This nonohmic contact is probably due to the

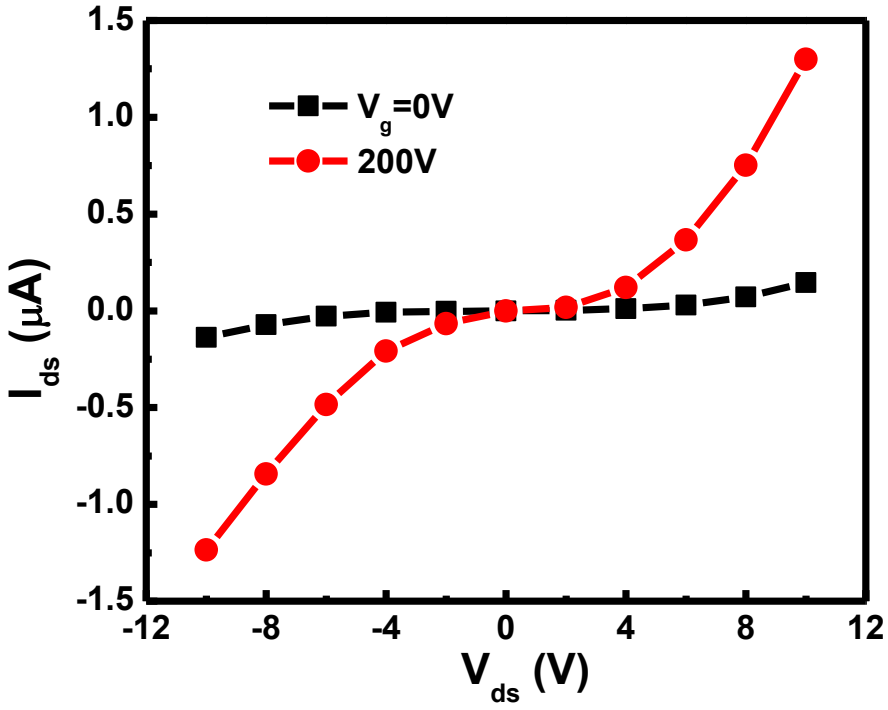

Figure 3-35 Current-Voltage curve of a single-layer MoS_2 device STO

transfer process. In Figure 3-34, if looking closely, one can find out that one of the electrodes is moved from its original position after transfer. Although the movement of electrodes is very rarely found in the other transferred devices, one can somehow summarize that the electrodes are more or less affected during the transfer process. For graphene devices discussed in the previous sections, the contact is not a problem after transfer since graphene can always have good contact with metal electrodes. But the situation is quite different with MoS_2 devices. The mismatch of work functions of the device and metal electrodes creates huge Schottky's barrier which prevents the flow of current between electrodes and device. Although ohmic contact is obtained in devices on SiO_2/Si substrate, small influence in the electrodes could greatly increase the width and/or height of the Schottky's barrier, thus leading to a nonlinear current-voltage curve.

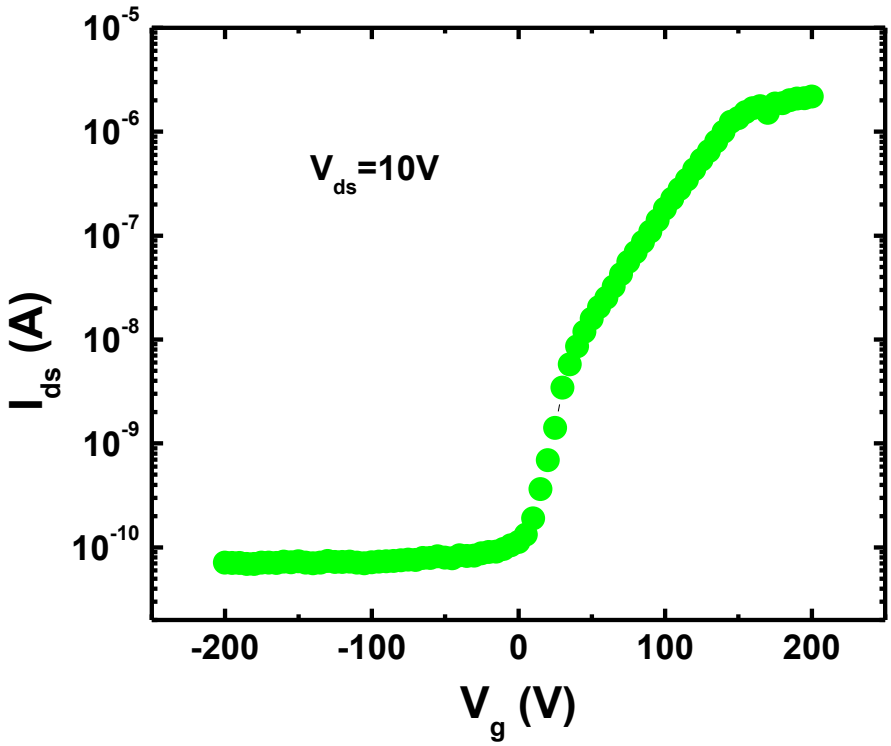

Figure 3-36 Gate dependence of a single-layer MoS2 device STO

The gate dependence of I_{ds} is shown in Figure 3-36. In order to see the dramatic change in magnitude of I_{ds}, the figure is plotted in a semi-log style. The source-drain voltage V_{ds} is fixed at 10V. When V_g is scanned from 200 V to -200 V, there is a change close to 10^5 in I_{ds}. In the gate dependence of I_{ds}, there are two sections in the gate dependence. From V_g = 200 V to 0 V, I_{ds} decreases as V_g is decreased, which should correspond to the decrease of Fermi level in the conduction band and hence the decrease in carrier density. But the Fermi level should be still in the conduction band or very close to the bottom of the conduction band. In the figure, from V_g = 200 V to 0V, there looks like slope changes around V_g = 150 V and 50 V. However, they are artificial slope changes only due to the semi-log plot. If plotted in a normal way, it is linearly decreases as

the gate voltage decreases. The second section is from V_g = 0 V to -200V. In this range, I_{ds} is very small and has almost no change, indicating the Fermi level is already inside the band gap.

With the thickness of STO substrate t = 200 μm, the capacitance per unit area is only $C_{S,STO}$ = 1.33×10^{-5} F/m^2 (assuming the dielectric constant of STO at room temperature is 300). Then the field-effect mobility can be extracted from the range between V_g = 200 V to 0 V, which is only 5 cm^2/V·s. This is a comparable value to the one obtained on SiO_2/Si substrate. But this value is only an estimation without considering the contribution from the contact resistance. As is pointed out previously that the contact becomes worse after transfer. So the actual mobility could be higher. Moreover and most importantly, the dielectric constant used in the capacitance calculation is only a simple number. But for a ferroelectric-like materials as STO, the dielectric constant changes with the change of the electric field, exhibiting a complex behavior with the application of a gate voltage[97]. So the actual field-effect mobility could be different. Great enhancement in mobility is not observed.

However, an enhancement in the gate tunability is observed. There is only 10^3 change in I_{ds} or R_{2T} with the SiO_2/Si substrate. But a change of 10^5 in I_{ds} or R_{2T} is achieved with the STO substrate. Yet, the Fermi level cannot be tuned close to the valence band. To further push the tunability of STO substrate, thinner STO dielectric layer is needed. This can be achieved by depositing nm-thick STO on Nb-doped STO substrate, which needs future efforts.

3.6.3.3 Ionic Liquid Gating

To realize the ambipolar gating, that is to tune the Fermi level to the valence band, either thinner STO substrate or a more powerful dielectric material needs to be developed. Ionic liquid has caught researcher's eyes for its high tunability in the carrier density[98,99], (as high as 10^{14} cm^{-2} change in

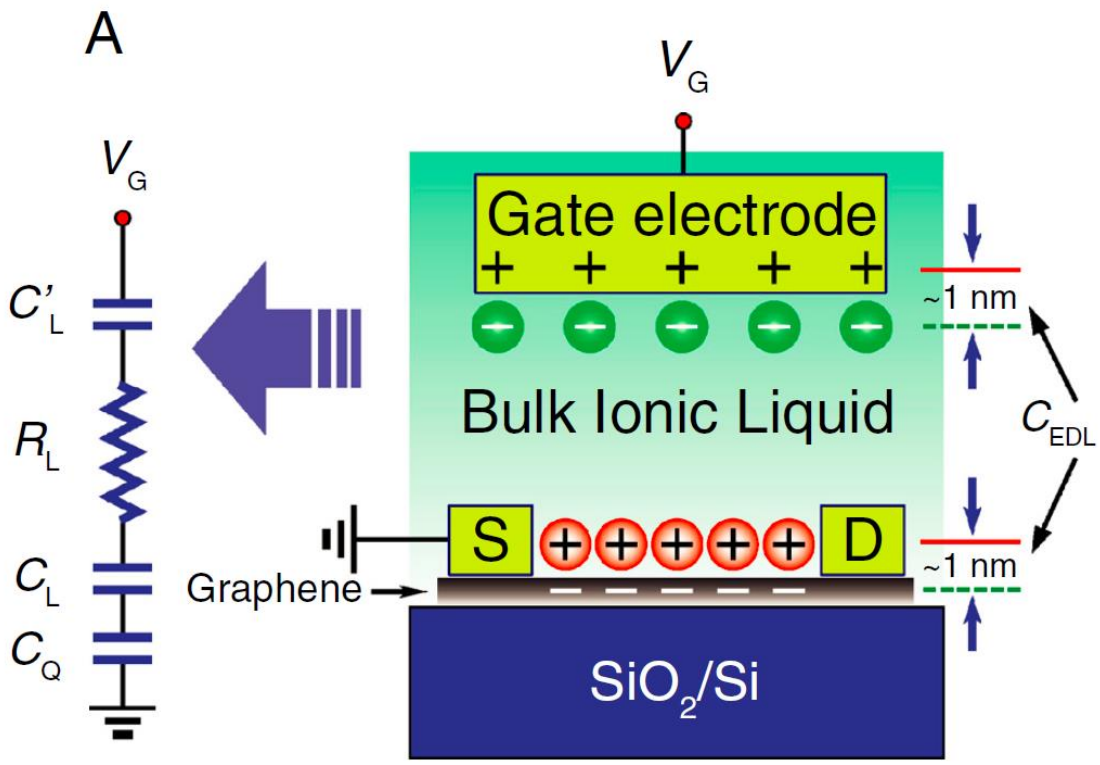

Figure 3-37 Schematic cross-section of the ionic liquid gating
Left figure is the equivalent electric circuit of the ionic liquid gating. Right figure is the schematic cross-section diagram of the ionic liquid gating. [Ye, *et al. Proceedings of the National Academy of Sciences* **108**, 13002-13006]

carrier density is observed). The ambipolar gating is also realized in MoS_2 devices with the use of ionic liquid[100].

After the ionic liquid is dropped on top of the device, with the gate voltages, it forms an electric double layer (EDL) between the ionic liquid and device, as is illustrated in Figure 3-37. In Figure 3-37, the left figure is the equivalent electric circuit of the right figure. C_L' stands for the capacitance between the gate electrode and the ionic liquid. R_L represents the equivalent resistance of the ionic liquid. C_L is the geometrical capacitance between the electric double layer and graphene device. And C_Q is the quantum capacitance of graphene which is due to the finite density of states. The

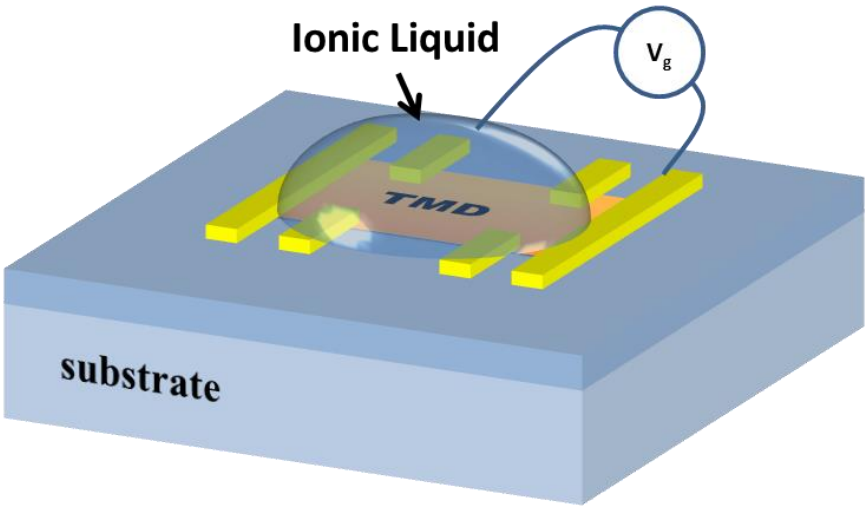

Figure 3-38 schematic diagram of the device with ionic liquid gating

effective thickness between the electric double layer and graphene is only ~ 1 nm. With a few gate voltages, there will be a huge effective gate acting on the graphene device.

MoS_2 device is fabricated on SiO_2/Si substrate first. After the device is wire bonded to a sample holder, a drop of ionic liquid (*N*,*N*-diethyl-*N*-(2-methoxyethyl)-*N*-methylammonium bis-(trifluoromethylsulfonyl)-imide (DEME-TFSI)) covers the top of the MoS_2 area. Due to the low viscosity and high liquid mobility of the ionic liquid, the device should be placed faced-up in case of the flow of the ionic liquid. A probe station is adopted for the measurement. One of the probes in the probe station is inserted into the ionic liquid, which is used as the gate electrode. Additional wires are bonded from the device to the sample holder for electrical transport measurements. All measurements are performed at room temperature. Figure 3-38 is the schematic diagram of the device configuration with ionic liquid gating on top.

The safe gate voltage range that can be applied to this type of ionic liquid is from -3 V to 3 V. However, when at high gate voltages (> 2 V or < -2 V), this type of ionic liquid becomes very reactive. After a loop of gate voltage scan from -3 V to 3 V, no signal can be detected. Sometimes,

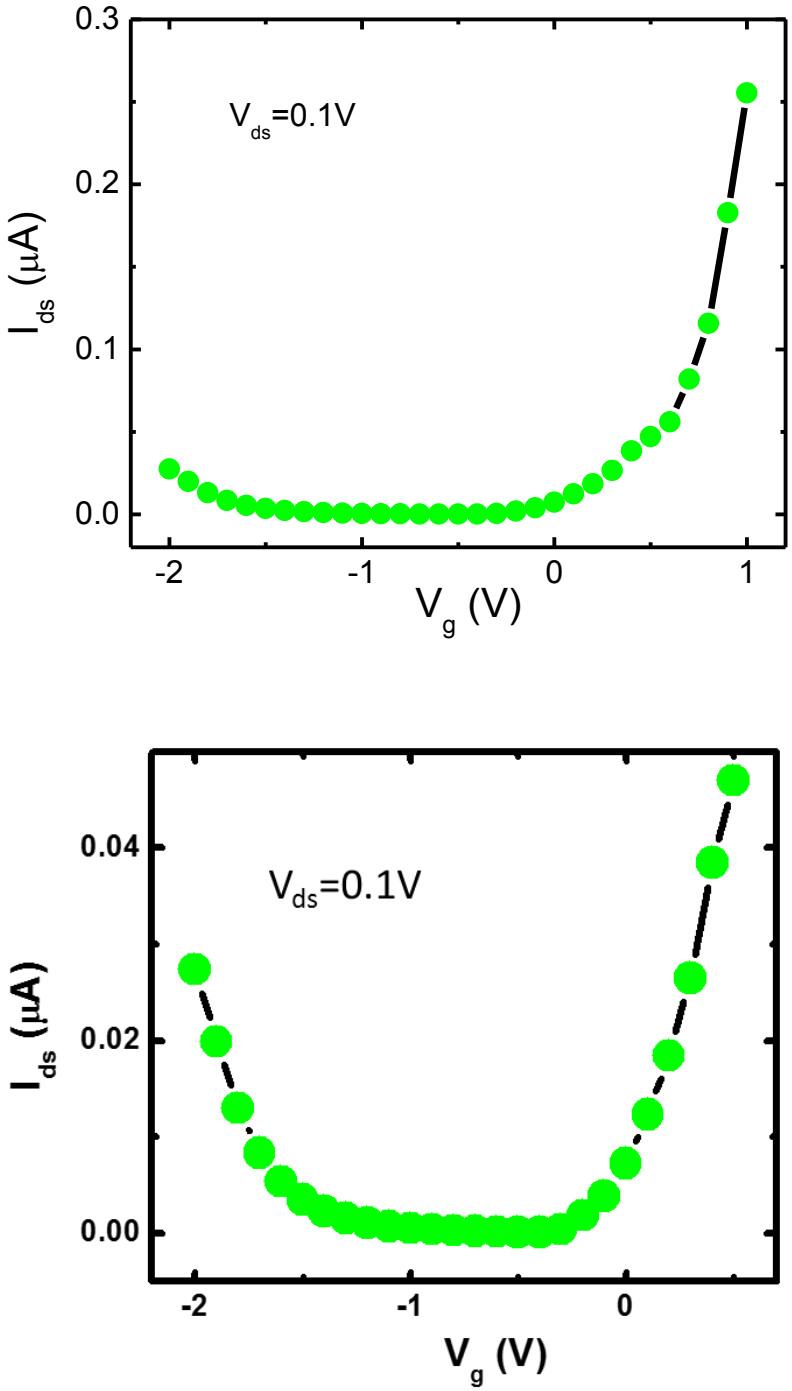

Figure 3-39 Gate dependence of a MoS_2 device with ionic liquid gating
Lower figure is a zoom-in plot of the upper figure from -2 V to 0.5 V in V_g.

even the metal electrodes are found to be reacted with the ionic liquid (there is a color change in the metal electrodes). Either the contact between the device and electrodes or the device itself turns bad during this process. Figure 3-39 is the gate dependence of I_{ds} with ionic liquid gating. The gate voltage is applied only within V_g = -2 V to 1 V to minimally suppress the reaction between the device/electrodes and the ionic liquid. The lower figure is a zoom-in plot of the upper figure in V_g from -2 V to 0.5 V. There is a clear increase in I_{ds} when V_g is close to -2 V, which is an indicative sign of the ambipolar gating and the approaching of Fermi level to the top of valence band. However, the resistances at high positive and negative gate voltages are very large, 392 kΩ at V_g = 1V and 3.65 MΩ at V_g = -2 V. The high resistance have an indication that the Fermi level may not reach the valence band yet but should be very close to the valence band maximum. Future work is needed to further push the gate tunability of the ionic liquid. One possibility is to cool the system down to a temperature right above the freezing point of the ionic liquid (220 K for DEME-TFSI). The reactivity of the ionic liquid with device and electrodes can be effectively reduced, which means higher gate voltage (±3 V) and longer time at a certain gate voltage can be achieved without affecting or damaging the device properties and the contact between the device and electrodes.

3.6.4 Discussion

The MoS_2 nanoflakes are mechanically exfoliated on SiO_2/Si substrate. The single-layer MoS_2 nanoflakes can be identified by the optical microscopy, which is further confirmed by both Raman spectroscopy and atomic force microscopy. Single-layer MoS_2 nanoflakes with proper size are identified and located under the optical microscope. Then nanodevices are fabricated out of the nanoflakes by standard electron beam lithography technique with the use of LOR/PMMA resist. The electrical transport properties are characterized, including the current-voltage characteristics

and the gate dependence. A change over 10^3 in resistance has been accomplished in the devices on SiO_2/Si substrate within a 120V-gate voltage range.

It is found that the as-exfoliated flakes are naturally electron-doped, resulting an n-type behavior without gate application. However, to realize the valley Hall effect, which is discussed in Chapter 1, the Fermi level has to be tuned to the valence band maximum. A material with high dielectric constant is then explored, which is the strontium titanate (STO). The pre-fabricated MoS_2 devices are successfully transferred to the 200-μm-thick strontium titanate substrate. The change in resistance with gate voltage has been further improved to 10^5 after the transfer. However, the realization of p-type transition has not been achieved yet. Thinner STO dielectric layer may be a solution to further push the gate tunability.

On the other hand, the ionic liquid is studied in order to tune the Fermi level further in the bandgap, reaching the valence band maximum. A sign of ambipolar gating is observed at room temperature, implying that the Fermi level is very close to the valence band. Low temperature measurement should be planned in the future in order to achieve a higher gate voltage with ionic liquid gating, and therefore wider range of the Fermi level tuning. More work needs to be performed realize the valley Hall effect in transition metal dichalcogenides.

Chapter 4 Conclusion

In this dissertation, three different special materials are studied, topological insulators (Bi_2Se_3 and Bi_2Te_2Se), graphene and transition metal dichalcogenides. Their bulk forms are all layered structures with Van der Waals force bonding between layers.

In the first part, two different topological insulator candidates, Bi_2Se_3 and Bi_2Te_2Se, are explored. Starting from the synthesis and XRD characterization of single crystals, Bi_2Se_3 and Bi_2Te_2Se bulk flakes are then characterized both optically (FTIR) and electrically. Thickness of the bulk flakes is determined with FTIR spectroscopy. Bulk insulating behaviors are achieved and confirmed by the resistance temperature dependence measurement. The bulk insulating flakes are always with low carrier density as is confirmed by the Hall effect measurement. Especially, extremely high 3D resistivity (> 2 Ω cm) is achievement in Bi_2Te_2Se bulk flakes indicating the suppression of bulk carrier channels. Moreover, in the most resistive Bi_2Te_2Se bulk flakes, the Hall coefficient also has a temperature dependence, in which the majority carriers change from holes to electrons when the flake is cooled from room temperature to 10 K. The bulk bandgap of Bi_2Se_3 is determined from the relationship between the relative Fermi level position and 3D carrier density, which are extracted from FTIR and Hall effect measurements, respectively. Shubnikov-de Haas effect are both observed in Bi_2Se_3 and Bi_2Te_2Se flakes, an indicative sign of high mobility carrier channels, suggesting the detection of topological surface states.

Bi_2Se_3 nanodevices are then fabricated in a lithography-free technique which is developed to overcome the disadvantages of normal lithography approach. Moreover, the devices are intentionally exfoliated from overdoped p-type bulk flakes. With the help of electron beam irradiation, the excess hole carriers in the p-type devices are then compensated. The insulating behavior is observed in the device after electron beam irradiation. The relative position of the Fermi

level is extracted from the resistivity temperature dependence in the device after each electron beam irradiation. Gate dependence measurement reveals the Dirac point in the most insulating state. It also gives the highest observed field-effect mobility in Bi_2Se_3 nanodevice among the mobilities reported so far. The minimum conductivity as low as 28 e^2/h is obtained. Some extended impurity states are believed to exist in the device, which lead to the increase in the minimum conductivity.

To conclude the study of the topological insulators, the excess bulk carriers issue is solved in both bulk samples and nanodevices. The temperature dependence of the resistivity which is the most important feature of the insulating states is studied. Hall effect measurement further confirms the decrease of the bulk carriers. Shubnikov-de Haas effect measurement gives a substantial evidence for the high mobility topological surface states. And we firstly realize high field-effect mobility in Bi_2Se_3 nanodevices. More systematic study on Bi_2Te_2Se (both bulk materials and nanodevices) can be planned to achieve p-type in this material and then use the same technique as is used on the Ca-doped Bi_2Se_3 devices. Theoretically, Bi_2Te_2Se is expected to be cleaner than Ca-doped Bi_2Se_3 since it is only a pure compound without any doping. High mobility surface state with even lower minimum conductivity should be achieved in Bi_2Te_2Se devices.

The second part is the study of graphene devices on an insulating magnetic thin film, YIG. Atomically flat YIG thin film is deposited in a pulsed laser deposition system. Both atomic force microscopy and room temperature magnetic hysteresis loop are performed to confirm the surface flatness and magnetism of YIG thin films. Since YIG/GGG substrate is thick and insulating, graphene devices are nanofabricated on SiO_2/Si substrate first and then transferred to the YIG thin films with a device transfer technique. Devices are characterized with Raman spectroscopy before and after the transfer process. Similar spectra are obtained, shows the success of the device transfer technique. No observable D peak is present in the Raman spectra, which indicates that the transfer process does not negatively affect graphene's quality. Gate dependence measured before and after

the transfer process further confirms this statement. The field-effect mobility extracted from the gate dependence is nearly unchanged.

At low temperatures, the AHE is observed in the transferred graphene devices, which is the first observation the AHE in graphene on a magnetic insulator. The saturation field has high consistency with that of the YIG films. The AHE dependence study gives the magnetic coupling strength which is ~ 25 meV and the Curie temperature T_C ~ 300 K. The gate dependence of the AHE is then studied. The power relationship between the AHE resistance and longitudinal resistivity is obtained with the exponent equals to 2.

The use of a magnetic insulator as graphene substrate provide a new approach to study the magnetism in graphene without affecting graphene's mobility. And the unique properties of YIG films make it stand out of the other materials, such as ferrimagnetic (magnetism), atomically flat (intimate contact with graphene), insulating (no shunting current to graphene device), chemically and magnetically stable, etc. Different from the traditional conducting ferromagnetic materials, graphene is a complete new system for the study of ferromagnetism. The detailed mechanism of the AHE in the transferred graphene device needs further studies both experimentally and theoretically.

The primary study of the transition metal dichalcogenides is described in Section 3.6. The same exfoliation method is used for MoS_2 nanoflakes. A Schottky's barrier is found between the device and the electrode after device nanofabrication. Different approaches are taken to realize the ohmic contact between the device and the electrodes, including device annealing, different metals for contact electrodes, the employment of LOR resist, contact area doping by reactive ion etching, etc. The ohmic contact is then achieved with the use of LOR resist and is confirmed by the current-voltage characteristic curves.

With the application of a SiO_2 back gate, a change of 10^3 in the resistance is achieved. And it is further improved to 10^5 with the use of a STO back gate. Moreover, with the help of ionic liquid, a sign of ambipolar gating is observed, indicating the realization of adjusting the Fermi level close to the top of the valence band. Due to the high reactivity of the ionic liquid at room temperature with high gate voltages, the measurement is limited. Studies under low temperature (but above the freezing point of the ionic liquid) should be conducted in the future. And more work needs to be carried out to realize the ohmic contact, to widely tune the Fermi level, and to realize the valley Hall effect and other related phenomena.

Bibliography

1 Novoselov, K. S. *et al.* Electric Field Effect in Atomically Thin Carbon Films. *Science* **306**, 666-669 (2004).

2 Bernevig, B. A., Hughes, T. L. & Zhang, S. C. Quantum spin Hall effect and topological phase transition in HgTe quantum wells. *Science* **314**, 1757-1761 (2006).

3 Mak, K., Lee, C., Hone, J., Shan, J. & Heinz, T. Atomically Thin MoS_2: A New Direct-Gap Semiconductor. *Physical Review Letters* **105**, 136805 (2010).

4 Xiao, D., Liu, G.-B., Feng, W., Xu, X. & Yao, W. Coupled Spin and Valley Physics in Monolayers of MoS_2 and Other Group-VI Dichalcogenides. *Physical Review Letters* **108**, 196802 (2012).

5 Fu, L., Kane, C. & Mele, E. Topological Insulators in Three Dimensions. *Physical Review Letters* **98**, 106803 (2007).

6 Fu, L. & Kane, C. Topological insulators with inversion symmetry. *Physical Review B* **76**, 045302 (2007).

7 Moore, J. & Balents, L. Topological invariants of time-reversal-invariant band structures. *Physical Review B* **75**, 121306 (2007).

8 Roy, R. Topological phases and the quantum spin Hall effect in three dimensions. *Physical Review B* **79**, 195322 (2009).

9 Kane, C. L. & Mele, E. J. Quantum Spin Hall Effect in Graphene. *Physical Review Letters* **95**, 226801 (2005).

10 Kane, C. L. & Mele, E. J. Z_2 Topological Order and the Quantum Spin Hall Effect. *Physical Review Letters* **95**, 146802 (2005).

11 Konig, M. *et al.* Quantum spin hall insulator state in HgTe quantum wells. *Science* **318**, 766-770 (2007).

12 Hsieh, D. *et al.* A topological Dirac insulator in a quantum spin Hall phase. *Nature* **452**, 970-974 (2008).

13 Hsieh, D. *et al.* Observation of Unconventional Quantum Spin Textures in Topological Insulators. *Science* **323**, 919-922 (2009).

14 Roushan, P. *et al.* Topological surface states protected from backscattering by chiral spin texture. *Nature* **460**, 1106-1109 (2009).

15 Zhang, H. *et al.* Topological insulators in Bi_2Se_3, Bi_2Te_3 and Sb_2Te_3 with a single Dirac cone on the surface. *Nat Phys* **5**, 438-442 (2009).

16 Hsieh, D. *et al.* A tunable topological insulator in the spin helical Dirac transport regime. *Nature* **460**, 1101-1105 (2009).

17 Xia, Y. *et al.* Observation of a large-gap topological-insulator class with a single Dirac cone on the surface. *Nat Phys* **5**, 398-402 (2009).

18 Chen, Y. L. *et al.* Experimental Realization of a Three-Dimensional Topological Insulator, Bi_2Te_3. *Science* **325**, 178-181 (2009).

19 Hsieh, D. *et al.* Observation of Time-Reversal-Protected Single-Dirac-Cone Topological-Insulator States in Bi_2Te_3 and Sb_2Te_3. *Physical Review Letters* **103**, 146401 (2009).

20 Zhang, T. *et al.* Experimental Demonstration of Topological Surface States Protected by Time-Reversal Symmetry. *Physical Review Letters* **103**, 266803 (2009).

21 Ren, Z., Taskin, A., Sasaki, S., Segawa, K. & Ando, Y. Large bulk resistivity and surface quantum oscillations in the topological insulator Bi_2Te_2Se. *Physical Review B* **82**, 241306 (2010).

22 Wang, L.-L. & Johnson, D. Ternary tetradymite compounds as topological insulators. *Physical Review B* **83**, 241309 (2011).

23 Chang, C. Z. *et al.* Thin films of magnetically doped topological insulator with carrier-independent long-range ferromagnetic order. *Advanced materials* **25**, 1065-1070 (2013).

24 Lang, M. *et al.* Competing Weak Localization and Weak Antilocalization in Ultrathin Topological Insulators. *Nano letters* **13**, 48-53 (2012).

25 Kong, D. *et al.* Ambipolar field effect in the ternary topological insulator $(Bi_xSb_{1-x})_2Te_3$ by composition tuning. *Nat Nano* **6**, 705-709 (2011).

26 Chang, C.-Z. *et al.* Experimental Observation of the Quantum Anomalous Hall Effect in a Magnetic Topological Insulator. *Science* **340**, 167-170 (2013).

27 Arakane, T. *et al.* Tunable Dirac cone in the topological insulator $Bi_{2-x}Sb_xTe_{3-y}Se_y$. *Nature communications* **3**, 636 (2012).

28 Ren, Z., Taskin, A. A., Sasaki, S., Segawa, K. & Ando, Y. Optimizing $Bi_{2-x}Sb_xTe_{3-y}Se_y$ solid solutions to approach the intrinsic topological insulator regime. *Physical Review B* **84**, 165311 (2011).

29 Liu, M. *et al.* Crossover between Weak Antilocalization and Weak Localization in a Magnetically Doped Topological Insulator. *Physical Review Letters* **108**, 036805 (2012).

30 Yang, Q. I. *et al.* Emerging weak localization effects on a topological insulator–insulating ferromagnet (Bi_2Se_3-EuS) interface. *Physical Review B* **88**, 081407 (2013).

31 Wei, P. *et al.* Exchange-Coupling-Induced Symmetry Breaking in Topological Insulators. *Physical Review Letters* **110**, 186807 (2013).

32 Jiang, H., Wang, L., Sun, Q.-f. & Xie, X. C. Numerical study of the topological Anderson insulator in HgTe/CdTe quantum wells. *Physical Review B* **80**, 165316 (2009).

33 Groth, C. W., Wimmer, M., Akhmerov, A. R., Tworzydło, J. & Beenakker, C. W. J. Theory of the Topological Anderson Insulator. *Physical Review Letters* **103**, 196805 (2009).

34 Li, J., Chu, R.-L., Jain, J. K. & Shen, S.-Q. Topological Anderson Insulator. *Physical Review Letters* **102**, 136806 (2009).

35 Dziawa, P. *et al.* Topological crystalline insulator states in $Pb_{1-x}Sn_xSe$. *Nat Mater* **11**, 1023-1027 (2012).

36 Dzero, M., Sun, K., Galitski, V. & Coleman, P. Topological Kondo Insulators. *Physical Review Letters* **104**, 106408 (2010).

37 Wang, Z. F., Liu, Z. & Liu, F. Organic topological insulators in organometallic lattices. *Nature communications* **4**, 1471 (2013).

38 Charlier, J.-C., Blase, X. & Roche, S. Electronic and transport properties of nanotubes. *Reviews of Modern Physics* **79**, 677-732 (2007).

39 Novoselov, K. S. *et al.* Two-dimensional gas of massless Dirac fermions in graphene. *Nature* **438**, 197-200 (2005).

40 Zhang, Y., Tan, Y.-W., Stormer, H. L. & Kim, P. Experimental observation of the quantum Hall effect and Berry's phase in graphene. *Nature* **438**, 201-204 (2005).

41 Son, Y.-W., Cohen, M. L. & Louie, S. G. Half-metallic graphene nanoribbons. *Nature* **444**, 347-349 (2006).

42 Chen, J.-H., Li, L., Cullen, W. G., Williams, E. D. & Fuhrer, M. S. Tunable Kondo effect in graphene with defects. *Nat Phys* **7**, 535-538 (2011).

43 Uchoa, B., Kotov, V. N., Peres, N. M. R. & Castro Neto, A. H. Localized Magnetic States in Graphene. *Physical Review Letters* **101**, 026805 (2008).

44 Dietl, T. A ten-year perspective on dilute magnetic semiconductors and oxides. *Nat Mater* **9**, 965-974 (2010).

45 Qiao, Z. *et al.* Quantum anomalous Hall effect in graphene from Rashba and exchange effects. *Physical Review B* **82**, 161414 (2010).

46 Mak, K. F., He, K., Shan, J. & Heinz, T. F. Control of valley polarization in monolayer MoS_2 by optical helicity. *Nat Nano* **7**, 494-498 (2012).

47 Checkelsky, J. *et al.* Quantum Interference in Macroscopic Crystals of Nonmetallic Bi_2Se_3. *Physical Review Letters* **103** (2009).

48 Hor, Y. *et al.* p-type Bi_2Se_3 for topological insulator and low-temperature thermoelectric applications. *Physical Review B* **79**, 195208 (2009).

49 Wang, Z. *et al.* Tuning carrier type and density in Bi_2Se_3 by Ca-doping. *Applied Physics Letters* **97**, 042112 (2010).

50 Wang, Z.-y., Wei, P. & Shi, J. Tuning the Fermi level in Bi_2Se_3 bulk materials and transport devices. *Frontiers of Physics* **7**, 160-164 (2011).

51 Neupane, M. *et al.* Topological surface states and Dirac point tuning in ternary topological insulators. *Physical Review B* **85**, 235406 (2012).

52 LaForge, A. D. *et al.* Optical characterization of Bi_2Se_3 in a magnetic field: Infrared evidence for magnetoelectric coupling in a topological insulator material. *Physical Review B* **81**, 125120 (2010).

53 Vaško, A., Tichý, L., Horák, J. & Weissenstein, J. Amphoteric nature of copper impurities in Bi_2Se_3 crystals. *Appl. Phys.* **5**, 217-221 (1974).

54 Wei, P., Wang, Z., Liu, X., Aji, V. & Shi, J. Field-effect mobility enhanced by tuning the Fermi level into the band gap of Bi_2Se_3. *Physical Review B* **85**, 201402 (2012).

55 Köhler, H. & Fabbicius, A. Galvanomagnetic Properties of Bi_2Se_3 with Free Carrier Densities below 5×10^{17} cm^{-3}. *physica status solidi (b)* **71**, 487-496 (1975).

56 Köhler, H. & Hartmann, J. Burstein Shift of the Absorption Edge of n-Bi_2Se_3. *physica status solidi (b)* **63**, 171-176 (1974).

57 Köhler, H. Conduction Band Parameters of Bi_2Se_3 from Shubnikov-de Haas Investigations. *physica status solidi (b)* **58**, 91-100 (1973).

58 Qu, D.-X., Hor, Y. S., Xiong, J., Cava, R. J. & Ong, N. P. Quantum Oscillations and Hall Anomaly of Surface States in the Topological Insulator Bi_2Te_3. *Science* **329**, 821-824 (2010).

59 Taskin, A. A., Sasaki, S., Segawa, K. & Ando, Y. Manifestation of Topological Protection in Transport Properties of Epitaxial Bi_2Se_3 Thin Films. *Physical Review Letters* **109**, 066803 (2012).

60 Ren, Z., Taskin, A. A., Sasaki, S., Segawa, K. & Ando, Y. Observations of two-dimensional quantum oscillations and ambipolar transport in the topological insulator Bi_2Se_3 achieved by Cd doping. *Physical Review B* **84**, 075316 (2011).

61 Xiu, F. *et al.* Manipulating surface states in topological insulator nanoribbons. *Nat Nano* **6**, 216-221 (2011).

62 Sacépé, B. *et al.* Gate-tuned normal and superconducting transport at the surface of a topological insulator. *Nature communications* **2**, 575 (2011).

63 Analytis, J. G. *et al.* Bulk Fermi surface coexistence with Dirac surface state in Bi_2Se_3: A comparison of photoemission and Shubnikov–de Haas measurements. *Physical Review B* **81**, 205407 (2010).

64 Analytis, J. G. *et al.* Two-dimensional surface state in the quantum limit of a topological insulator. *Nat Phys* **6**, 960-964 (2010).

65 Butch, N. P. *et al.* Strong surface scattering in ultrahigh-mobility Bi_2Se_3 topological insulator crystals. *Physical Review B* **81**, 241301 (2010).

66 Ren, Z., Taskin, A. A., Sasaki, S., Segawa, K. & Ando, Y. Fermi level tuning and a large activation gap achieved in the topological insulator Bi_2Te_2Se by Sn doping. *Physical Review B* **85**, 155301 (2012).

67 Xiong, J. *et al.* Quantum oscillations in a topological insulator Bi_2Te_2Se with large bulk resistivity (6 Ω cm). *Physica E: Low-dimensional Systems and Nanostructures* **44**, 917-920 (2012).

68 Xiong, J. *et al.* High-field Shubnikov–de Haas oscillations in the topological insulator Bi_2Te_2Se. *Physical Review B* **86** (2012).

69 Eto, K., Ren, Z., Taskin, A. A., Segawa, K. & Ando, Y. Angular-dependent oscillations of the magnetoresistance in Bi_2Se_3 due to the three-dimensional bulk Fermi surface. *Physical Review B* **81**, 195309 (2010).

70 Kong, D. *et al.* Rapid Surface Oxidation as a Source of Surface Degradation Factor for Bi_2Se_3. *ACS Nano* **5**, 4698-4703 (2011).

71 Chen, Y. L. *et al.* Massive Dirac Fermion on the Surface of a Magnetically Doped Topological Insulator. *Science* **329**, 659-662 (2010).

72 Castro Neto, A. H., Guinea, F., Peres, N. M. R., Novoselov, K. S. & Geim, A. K. The electronic properties of graphene. *Reviews of Modern Physics* **81**, 109-162 (2009).

73 Ong, N. P. Two-band model for $NbSe_3$ (Ohmic regime). *Physical Review B* **18**, 5272-5279 (1978).

74 Balakrishnan, J., Kok Wai Koon, G., Jaiswal, M., Castro Neto, A. H. & Ozyilmaz, B. Colossal enhancement of spin-orbit coupling in weakly hydrogenated graphene. *Nat Phys* **9**, 284-287 (2013).

75 Huang, S. Y. *et al.* Transport Magnetic Proximity Effects in Platinum. *Physical Review Letters* **109**, 107204 (2012).

76 Lu, Y. M. *et al.* Pt Magnetic Polarization on $Y_3Fe_5O_{12}$ and Magnetotransport Characteristics. *Physical Review Letters* **110**, 147207 (2013).

77 Lin, T., Tang, C. & Shi, J. Induced magneto-transport properties at palladium/yttrium iron garnet interface. *Applied Physics Letters* **103**, 132407 (2013).

78 Sun, Q.-f., Jiang, Z.-t., Yu, Y. & Xie, X. C. Spin superconductor in ferromagnetic graphene. *Physical Review B* **84**, 214501 (2011).

79 Qiao, Z. *et al.* Quantum Anomalous Hall Effect in Graphene Proximity Coupled to an Antiferromagnetic Insulator. *Physical Review Letters* **112**, 116404 (2014).

80 Konschuh, S., Gmitra, M. & Fabian, J. Tight-binding theory of the spin-orbit coupling in graphene. *Physical Review B* **82**, 245412 (2010).

81 Varykhalov, A. *et al.* Electronic and Magnetic Properties of Quasifreestanding Graphene on Ni. *Physical Review Letters* **101**, 157601 (2008).

82 Dedkov, Y. S., Fonin, M., Rüdiger, U. & Laubschat, C. Rashba Effect in the Graphene/Ni(111) System. *Physical Review Letters* **100**, 107602 (2008).

83 Sachs, R., Lin, Z., Odenthal, P., Kawakami, R. & Shi, J. Direct comparison of graphene devices before and after transfer to different substrates. *Applied Physics Letters* **104**, 033103 (2014).

84 Ferrari, A. C. *et al.* Raman Spectrum of Graphene and Graphene Layers. *Physical Review Letters* **97**, 187401 (2006).

85 Xiao, D., Yao, W. & Niu, Q. Valley-Contrasting Physics in Graphene: Magnetic Moment and Topological Transport. *Physical Review Letters* **99**, 236809 (2007).

86 Adam, S., Hwang, E. H., Galitski, V. M. & Das Sarma, S. A self-consistent theory for graphene transport. *Proceedings of the National Academy of Sciences* **104**, 18392-18397 (2007).

87 Lee, C. *et al.* Anomalous Lattice Vibrations of Single- and Few-Layer MoS_2. *ACS Nano* **4**, 2695-2700 (2010).

88 Splendiani, A. *et al.* Emerging photoluminescence in monolayer MoS_2. *Nano letters* **10**, 1271-1275 (2010).

89 Radisavljevic, B., Radenovic, A., Brivio, J., Giacometti, V. & Kis, A. Single-layer MoS_2 transistors. *Nat Nano* **6**, 147-150 (2011).

90 Castellanos-Gomez, A. *et al.* Electric-Field Screening in Atomically Thin Layers of MoS_2 : the Role of Interlayer Coupling. *Advanced materials* **25**, 899-903 (2012).

91 Kim, S. *et al.* High-mobility and low-power thin-film transistors based on multilayer MoS_2 crystals. *Nature communications* **3**, 1011 (2012).

92 Ghatak, S., Pal, A. N. & Ghosh, A. Nature of Electronic States in Atomically Thin MoS_2 Field-Effect Transistors. *ACS Nano* **5**, 7707-7712 (2011).

93 Jena, D. & Konar, A. Enhancement of Carrier Mobility in Semiconductor Nanostructures by Dielectric Engineering. *Physical Review Letters* **98**, 136805 (2007).

94 Casiraghi, C. *et al.* Rayleigh Imaging of Graphene and Graphene Layers. *Nano letters* **7**, 2711-2717 (2007).

95 Blake, P. *et al.* Making graphene visible. *Applied Physics Letters* **91**, 063124 (2007).

96 Abergel, D. S. L., Russell, A. & Fal'ko, V. I. Visibility of graphene flakes on a dielectric substrate. *Applied Physics Letters* **91**, 063125 (2007).

97 Sachs, R., Lin, Z. & Shi, J. Ferroelectric-like $SrTiO_3$ surface dipoles probed by graphene. *Sci. Rep.* **4**, 3657 (2014).

98 Ueno, K. *et al.* Electric-field-induced superconductivity in an insulator. *Nat Mater* **7**, 855-858 (2008).

99 Ye, J. *et al.* Accessing the transport properties of graphene and its multilayers at high carrier density. *Proceedings of the National Academy of Sciences* **108**, 13002-13006 (2011).

100 Zhang, Y., Ye, J., Matsuhashi, Y. & Iwasa, Y. Ambipolar MoS_2 Thin Flake Transistors. *Nano letters* **12**, 1136-1140 (2012).